This work was written as part of one of the author's official duties as an Employee of the United States Government and is therefore a work of the United States Government. In accordance with 17 U.S.C. 105, no copyright protection is available for such works under U.S. Law.

CC0 1.0 Universal (CC0 1.0)
Public Domain Dedication

https://creativecommons.org/publicdomain/zero/1.0/

Access to this work was provided by the University of Maryland, Baltimore County (UMBC) ScholarWorks@UMBC digital repository on the Maryland Shared Open Access (MD-SOAR) platform.

Please provide feedback

Please support the ScholarWorks@UMBC repository by emailing scholarworks-group@umbc.edu and telling us what having access to this work means to you and why it's important to you. Thank you.

Looking at cosmic near-infrared background radiation anisotropies

A. Kashlinsky[*]

*Code 665, Observational Cosmology Lab, Goddard Space Flight Center,
Greenbelt, Maryland 20771, USA
and SSAI, Lanham, Maryland 20706, USA*

R. G. Arendt

*Code 665, Observational Cosmology Lab, Goddard Space Flight Center,
Greenbelt, Maryland 20771, USA
and CRESST/University of Maryland, Baltimore County, Baltimore, Maryland 21250, USA*

F. Atrio-Barandela

Department of Fundamental Physics, University of Salamanca, 37008 Salamanca, Spain

N. Cappelluti

*Yale Center for Astronomy and Astrophysics,
P.O. Box 208120, New Haven, Connecticut 06520, USA
and Department of Physics, University of Miami, Coral Gables, Florida 33124, USA*

A. Ferrara

Scuola Normale Superiore, Piazza dei Cavalieri 7, I-56126 Pisa, Italy

G. Hasinger

*Institute for Astronomy, 2680 Woodlawn Drive, University of Hawaii,
Honolulu, Hawaii 96822, USA*

(published 19 June 2018)

The cosmic infrared background (CIB) contains emissions accumulated over the entire history of the Universe, including from objects inaccessible to individual telescopic studies. The near-infrared ($\sim$1–10 μm) part of the CIB, and its fluctuations, reflects emissions from nucleosynthetic sources and gravitationally accreting black holes. If known galaxies are removed to sufficient depths the source-subtracted CIB fluctuations at near-infrared can reveal sources present in the first stars era and possibly new stellar populations at more recent times. This review discusses the recent progress in this newly emerging field which identified, with new data and methodology, significant source-subtracted CIB fluctuations substantially in excess of what can be produced by remaining known galaxies. The CIB fluctuations further appear coherent with unresolved cosmic x-ray background indicating a very high fraction of black holes among the new sources producing the CIB fluctuations. These observations have led to intensive theoretical efforts to explain the measurements and their properties. While current experimental configurations have limitations in decisively probing these theories, their potentially remarkable implications will be tested in the upcoming CIB measurements with the European Space Agency's Euclid dark energy mission. The goals and methodologies of LIBRAE (Looking at Infrared Background Radiation with Euclid), a National Aeronautics and Space Administration (NASA) selected project for CIB science with Euclid, which has the potential for transforming the field into a new area of precision cosmology, are described.

CONTENTS

[*]Alexander.Kashlinsky@nasa.gov

I. INTRODUCTION

Development of modern physical cosmology began in earnest in the early 20th century, when Hubble's insight into the radial velocities of galaxies yielded the first observational evidence for expanding Universe models proposed as an immediate consequence of Einstein's gravitational field equations. The now accepted theory of the Universe's origin is known as the big bang model, named so in jest in 1950 by one of the proponents of the alternative "steady-state" cosmology, Sir Fred Hoyle. The discovery of the cosmic microwave background (CMB) radiation in 1964 (Penzias and Wilson, 1965), anticipated by Alpher (1948) and Alpher and Herman (1948), added a firm observational pillar in support of the big bang theory (Dicke *et al.*, 1965). The Cosmic Background Explorer (COBE) Far-Infrared Absolute Spectrophotometer (FIRAS) measurements (Mather *et al.*, 1990) revealed a highly accurate blackbody energy spectrum for the CMB confirming its origin in the hot dense early phase of the big bang. The CMB angular structure, uncovered first with the COBE Differential Microwave Radiometer measurements (Smoot *et al.*, 1992), provided an unprecedented insight into the density field of the Universe a mere $\sim 400\,000$ yr after the big bang.

This century has so far marked the emergence of precision cosmology, when the fundamental cosmological parameters and the contributions of the Universe's basic constituents to its matter and energy budget have been accurately determined. A standard cosmological model describing the evolution of structure has been established in agreement with the observations of CMB angular fluctuations on subdegree scales as probed by balloons (de Bernardis *et al.*, 2000; Lange *et al.*, 2001) and post-COBE finer resolution Wilkinson Microwave Anisotropy Probe (WMAP) (Bennett *et al.*, 2013) and Planck (Planck Collaboration *et al.*, 2016b) satellites. In addition, our understanding of high-energy physics is now sufficiently advanced for connecting cosmological phenomena to the quantum physics of the primordial Universe.

The widely accepted cosmological concordance model requires large amounts of dark matter (DM), as well as dark

energy (DE) of unknown nature and origin, and in broad terms explains the Universe's structure as follows. The large-scale isotropy of the Universe, as well as the small-scale inhomogeneities that evolved into galaxies and galaxy clusters, is thought to be the result of a period of early accelerated expansion, termed inflation (Kazanas, 1980; Guth, 1981; Linde, 1982). While the precise mechanism driving inflation and the underlying preinflationary structure of spacetime are still unknown, the matter density field predicted by inflation is now established observationally on scales $\gtrsim 10$ Mpc, which encompass masses $\gtrsim 10^{14} \, M_\odot$. Smaller scales subtend structures presently in nonlinear regimes where the original density field is not probed directly.

Much of the progress has been made through observational and theoretical studies of the CMB. It was only recently, however, that a lesser known relative of the CMB, the cosmic infrared background (CIB), started getting attention. CIB contains emissions over the entire history of the Universe, including from sources inaccessible to direct telescopic studies. The latter category includes the epoch when first stars were born as well as possible new populations at later times. The near-IR (1–10 μm) CIB, the subject of this review, probes emissions from early stars and black holes (BHs) (Partridge and Peebles, 1967; Bond, Carr, and Hogan, 1986; McDowell, 1986; Santos, Bromm, and Kamionkowski, 2002; Salvaterra and Ferrara, 2003; Cooray *et al.*, 2004; Kashlinsky *et al.*, 2004). To isolate the part of the CIB from new, potentially interesting cosmological sources, resolved galaxies must be excised from the maps to sufficiently faint levels. The remaining, source-subtracted CIB can then be compared to that expected after "reasonable" extrapolations, based on other data, from remaining known galaxies. An excess, if significant, would potentially reveal important cosmological information on the nature of the new sources, their epochs, abundances, and the density field in which they reside.

Measurements over the past decade from analyses of Spitzer by Kashlinsky *et al.* (2005, 2007b), Kashlinsky *et al.* (2012) and Cooray *et al.* (2012), and AKARI (Matsumoto *et al.*, 2011) satellite data identified near-IR CIB fluctuations remaining in deep integrations on subdegree and degree scales. It appears that these fluctuations cannot originate from remaining known galaxy populations (Kashlinsky *et al.*, 2005; Helgason, Ricotti, and Kashlinsky, 2012). It was further found that the CIB fluctuations are coherent with unresolved soft cosmic x-ray background (CXB) at levels much higher than expected from remaining known populations suggesting significantly greater BH proportions among the CIB sources than in known populations (Cappelluti *et al.*, 2013, 2017; Helgason *et al.*, 2014; Mitchell-Wynne *et al.*, 2016). The extensive list of empirical properties for these CIB fluctuations, discussed next, provides a further important set of clues to the origin of these sources. While some of the CIB properties, such as its amplitude, can be modeled with new populations at intermediate redshifts, other empirical evidence points toward the fluctuations originating at early epochs, possibly the "first stars era." New programs, specifically on the upcoming dark energy Euclid mission, will probe with unprecedented accuracy and scope the CIB from high redshifts, and its properties, enabling unique insight into the era of the first luminous sources, identifying their nature and the properties of the underlying density field at those epochs.

This review summarizes the current state of the near-IR CIB fluctuation measurements, their potentially remarkable theoretical implications, and discusses the future prospects of this rapidly developing field. Wherever the context permits, we will plot results in terms of the original quantities displayed in the corresponding measurement papers.

A list of symbols and abbreviations used throughout this review is given at the end.

II. BACKGROUND COSMOLOGY AND DEFINITIONS

Brightnesses of resolved sources are given in the *AB* magnitude system (Oke and Gunn, 1983), where the flux density S_ν of a source is related to the *AB* magnitude by $S_\nu = S_0 10^{-0.4 m_{AB}}$ with $S_0 = 3631 \, \text{Jy} = 3631 \times 10^{-26} \, \text{W} \, \text{m}^{-2} \, \text{Hz}^{-1}$. The surface brightnesses I_ν of extended sources are often given in units of $\text{MJy} \, \text{sr}^{-1}$ ($\text{MJy} = 10^6 \, \text{Jy} = 10^{-20} \, \text{W} \, \text{m}^{-2} \, \text{Hz}^{-1}$). It is common practice to express surface brightness per $\log \nu$ instead of ν by defining a flux as $F = I_\nu (d\nu/d\log \nu) = \nu I_\nu = (c/\lambda) I_\nu = \lambda I_\lambda$. Thus, in commonly used units, $F[\text{nW} \, \text{m}^{-2} \, \text{sr}^{-1}] = (3000/\lambda \, [\mu\text{m}]) I_\nu [\text{MJy} \, \text{sr}^{-1}]$. It is instructive to convert CIB surface brightness levels into their comoving photon number density:

$$n_{\text{CIB}}(\nu) = \frac{4\pi}{c} I_\nu / h_{\text{Planck}} = 0.63 \left(\frac{I_\nu}{\text{MJy/sr}} \right) \text{cm}^{-3}.$$

For comparison the CMB photons are orders of magnitude more abundant with $n_{\text{CMB}} = 413 \, \text{cm}^{-3}$.

CMB observations established the flat geometry of the Universe. We will thus adopt the Friedmann-Robertson-Walker flat metric for the Universe with the interval given by $ds^2 = c^2 dt^2 - (1+z)^{-2} (dx^2 + x^2 d\omega)$, where z, x, t, and ω are the redshift, comoving coordinate distance, cosmic time, and solid angle. Photons move along null geodesics $ds^2 = 0$. The Friedmann equations with the matter, dark energy (Λ), radiation or relativistic component and curvature density parameters $\Omega_m, \Omega_\Lambda, \Omega_\gamma,$ and Ω_K lead to $c(1+z) dt/dz = R_H/E(z)$, where $E(z) \equiv [\Omega_\gamma (1+z)^4 + \Omega_m (1+z)^3 + \Omega_K (1+z)^2 + \Omega_\Lambda f(z)]^{1/2}$ with $f(z)$ describing the evolution of DE and $R_H \equiv cH_0^{-1}$. The Hubble constant is $H(z) = H_0 E(z)$ and the distance measures become the coordinate distance $x(z) = c \int (1+z) dt = R_H \int_0^z dz/E(z)$, the comoving angular diameter distance $d_A(z) = x(z)$, and the luminosity distance $d_L(z) = (1+z) x(z)$. Proper distances are $(1+z)^{-1} \times$ (comoving distances and scales) and proper time intervals are $(1+z) \times$ (cosmic time).

We adopt the cosmological parameters $\Omega_K = 0, \Omega_\Lambda = 0.72,$ $\Omega_m = 0.28,$ $\Omega_{\text{baryon}} = 0.045,$ $h = 0.71,$ and $\sigma_8 = 0.9,$ where the present-day Hubble constant is $H_0 = 100h \, \text{km/s/Mpc}$. σ_8 is the present-day linear matter density contrast over a sphere of comoving radius $r_8 = 8h^{-1}$ Mpc (Davis and Peebles, 1983). The total mass contained on average within the comoving radius r is $M(r) = 4.9 \times 10^{11} (r/1h^{-1} \, \text{Mpc})^3$ and the baryonic mass is $M_{\text{baryon}}(r) = 7.8 \times 10^{10} (r/1h^{-1} \, \text{Mpc})^3$. We also adopt $\Omega_\gamma = 0$ and, for the bulk of the review, $f(z) = 1$, equivalent to the DE reflecting the vacuum energy density resulting in a cosmological constant Λ or equation of state with pressure $\mathcal{P} = -\rho c^2$.

The origin of structures in the Universe is tied to matter density fluctuations $\delta_m(\vec{x})$ produced during inflationary expansion. During the matter-dominated era, these fluctuations feel stronger gravitational field and expand at a slower rate than the average Universe: fluctuations grow until they become nonlinear, separate from the comoving frame and collapse. The fluctuations represent a stochastic random field, which can then be decomposed into independent Fourier modes. The variance of each mode is defined as the power spectrum. The correlation function $C(|\vec{x}_1 - \vec{x}_2|) \equiv \langle \delta_m(\vec{x}_1) \delta_m(\vec{x}_2) \rangle$ is then the Fourier transform (FT) of the power spectrum. The isotropy of the Universe requires that the correlation function depends only on the absolute value of the separation distance and the power spectrum only on the absolute wave number. The power spectrum defines all properties of Gaussian random fields, such as inflation-produced density fluctuations.

The standard cosmological model gives the power spectrum of the primordial adiabatic component of matter density fluctuations produced during the inflationary rollover, which is in agreement with CMB observations. This component of the matter density fluctuations starts with an approximately Harrison-Zeldovich (HZ) slope of the 3D power spectrum $P_{\text{3D,initial}}(k) \propto k$ (Guth and Pi, 1982), which is preserved on scales above the horizon at matter-radiation equality, but gets modified by differential growth of smaller wavelength harmonics (Bond and Efstathiou, 1984). The resultant three-dimensional power spectrum $P_{\text{3D}}(k)$ normalized to σ_8 at $z = 0$ is shown in Fig. 1. The inflationary density field is highly Gaussian and so is fully specified by its power spectrum. An important scale, to serve as a standard ruler, imprinted in the spatial spectrum is that of the baryonic acoustic oscillations (BAOs) at the acoustic horizon at decoupling $r_{\text{BAO}} \simeq 150$ Mpc
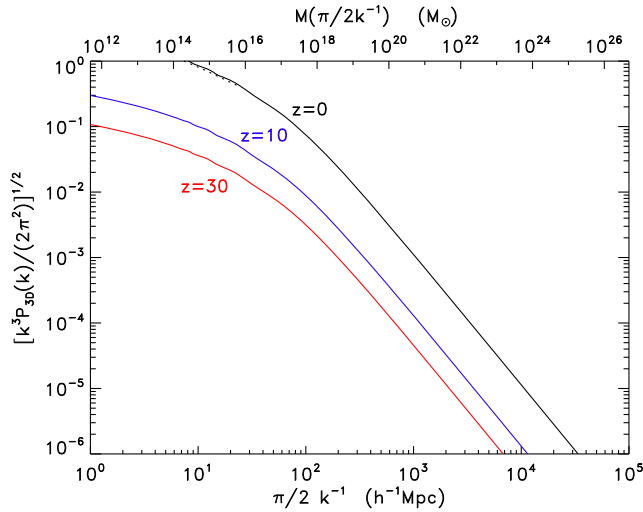

FIG. 1. The rms spectrum of primordial adiabatic density field in the lambda cold dark matter (ΛCDM) concordance model at $z = 0$, 10, and 30. At still higher z, the Universe is in the Einstein–de Sitter regime and the density field amplitude can be scaled as $\propto (1 + z)^{-1}$. At smaller scales the power spectrum approaches the regime $P_{\text{3D}} \propto k^{-3}$. In the spherical collapse model, fluctuations containing mass M with $\sqrt{k^3 P_{\text{3D}}/(2\pi^2)} \gtrsim \delta_{\text{col}} = 1.68$ collapse by z. The dotted line shows $\sigma_M(r)$ vs r at $z = 0$.

(Eisenstein and Hu, 1998, 1999). The mean squared amplitude of density fluctuations over a given radius r is given by $\sigma_M^2(r) = (1/2\pi^2) \int k^2 P_{\text{3D}}(k) W_{\text{TH}}(kr) dk$ with $W_{\text{TH}}(x) = [3j_1(x)/x]^2$, j_n being the spherical Bessel function of order n; it is shown in Fig. 1 with the dotted line at $z = 0$. Such measurements on a scale $r = \pi/2k^{-1}$ correspond to an effective sampling interval of $\Delta = 2r$, and thus a (minimum) spatial wavelength of $2\Delta = 2\pi k^{-1}$. Later, measurements of angular fluctuations are characterized in terms of the equivalent angular wavelength $\theta = 2\pi q^{-1}$.

If the DM is made up of primordial black holes (PBHs), as motivated recently (Bird *et al.*, 2016; Kashlinsky, 2016; Clesse and García-Bellido, 2017) by the Laser Interferometer GW Observatory (LIGO) gravitational wave (GW) discovery (Abbott *et al.*, 2016a, 2016e), the Poissonian fluctuations due to PBHs would provide an extra isocurvature density fluctuation component discussed first by Meszaros (1974, 1975) before the inflationary paradigm was introduced. The addition to power in density fluctuations at the time of the PBH formation from that component would be a constant $P_{\text{PBH,initial}} = n_{\text{PBH}}^{-1}$ in comoving units. This component would add to small-scale power of the density field, increasing the efficiency of early collapse of first halos (Kashlinsky, 2016).

Starting at matter-radiation equality, matter fluctuations grow $\delta\rho/\rho \propto (1 + z)^{-1}$ until the epoch when cosmological constant dominates $(1 + z) \lesssim 3$ and the growth slows down. As fluctuations turn nonlinear they separate from the comoving frame of expansion and collapse to form virialized halos which can host luminous sources forming out of the collapsing baryonic gas, provided it can efficiently cool to below the halo virial temperature.

Once the luminous sources form at high redshift $z \gtrsim 10$, their UV emission near 0.1 μm would contribute to the present CIB near $\gtrsim 1$ μm, and their cosmological power spectrum of clustering would be reflected in the CIB angular anisotropies. Hard x-ray emission from high-z BHs would contribute to the soft x-ray CXB, and related UV emission would make this coherent with the CIB.

The primordial density field in the standard ΛCDM cosmological model, as shown in Fig. 1, is such that after the Universe recombines at $z_{\text{rec}} \sim 1000$, there is an extended period, nicknamed the "dark ages," when no luminous sources existed and everything was made up of neutral hydrogen (H I) until the dark halos collapsing at $z \lesssim 40$–50 produced the first luminous sources. The near-IR CIB provides a new powerful tool to study the emergence of the Universe from the dark ages and the nature of the early luminous sources; recent CIB fluctuation results may have already produced tantalizing insight into these questions.

The nature of the first luminous sources and proportions of BHs among them are currently unknown together with the luminosity density they produced as the Universe started emerging from the dark ages. If dominated by massive stars and/or accreting BHs, the first luminous sources would radiate at the Eddington limit $L_{\text{Edd}} \propto M$ so that the net bolometric luminosity density produced by them is insensitive to the details of their mass function $n(M)$, since $\int n(M) L dM \propto \rho$ (in sources) (Rees, 1978). This leads to the net bolometric flux roughly equal to the maximal luminosity of any gravitating object $L_{\text{max}} = c^5/G$ distributed over the Hubble radius

$(R_H = cH_0^{-1})$ sphere, or $F \sim L_{\max}/(4\pi R_H^2)$ times model-dependent parameters, such as the fraction of baryons in these sources, the redshift of emission, and their radiation efficiency (Kashlinsky *et al.*, 2004). For sources at $z \gtrsim 10$, these emissions would go primarily into the near-IR CIB and with a net flux which is significant for realistic parameter values. While this part of the mean CIB is challenging to isolate from other components, it would have substantial fluctuations with a distinct spatial distribution reflecting the underlying matter power spectrum at those epochs.

There are intuitive reasons why there would be potentially significant, measurable CIB fluctuations from the first stars era (Cooray *et al.*, 2004; Kashlinsky *et al.*, 2004): (1) first stars are predicted to have been massive with luminosity per unit mass larger than present-day stellar populations by a factor of $\sim 10^4$; a similar factor applies to accreting Eddington-limited BHs; (2) their relative CIB fluctuations would be larger as they span a relatively short time span in the evolution of the Universe; and (3) these sources formed at the peaks of the underlying density field, amplifying their clustering properties.

III. MEAN LEVELS OF BACKGROUND LIGHT

We define the extragalactic background light (EBL) at wavelengths from UV to 10 μm to be the sum of all emissions from extragalactic sources. The CIB is the EBL at IR wavelengths, and in this review we focus on the near-IR CIB at 1 to 10 μm. The cosmic optical background (COB) (0.1–1 μm) has similar origins as the CIB, but is restricted to sources at $z \lesssim 7$ (Bernstein, 2007; Kawara *et al.*, 2017; Mattila, Lehtinen *et al.*, 2017; Mattila, Väisänen *et al.*, 2017). The CXB is the net diffuse emissions from 0.5 to 100 keV, with the soft x-ray CXB referring to the range of [0.5–2] keV.

In this section we discuss the status of the mean levels of the backgrounds. Previous reviews by Hauser and Dwek (2001)

and Kashlinsky (2005a) covered the status of the measurements prior to 2004 and the interested reader is referred to these papers for overviews. Here we mainly discuss the progress and the new results obtained since that time, referring to the earlier results only briefly when required for clarity and completion.

A. Galaxy counts and resolved EBL and CIB

The total flux from counted galaxies in deep surveys gives a direct lower bound on the CIB, identifying the contribution to it from the known resolved populations. A possible CIB excess over that component would contain contributions from new extragalactic populations. Since populations' energy emissions are cut off below the Lyman-cutoff wavelength $\sim 0.1(1 + z)$ μm, the wavelength dependence of the CIB would indicate the epochs when it arises. This situation from optical to near-IR bands was discussed by Kashlinsky (2005a) using the counts data available at the time. The updated discussion is presented later.

Following earlier determinations of deep counts in the near-IR [see, e.g., Gardner, Cowie, and Wainscoat (1993), Glazebrook *et al.* (1994), Madau and Pozzetti (2000), Totani, Yoshii, Iwamuro *et al.* (2001), Totani, Yoshii, Maihara *et al.* (2001), and Fazio *et al.* (2004a), and many others], further deeper counts covering a wider range of wavelengths have been obtained with new ground and space-borne instruments (Thompson *et al.*, 2005; Keenan *et al.*, 2010; Windhorst *et al.*, 2011; Ashby *et al.*, 2013, 2015; Driver *et al.*, 2016). Figure 2 shows the buildup of the EBL and CIB from the deepest optical (represented by *r* band) and near-IR counts available as of this review. The CIB contributions from known galaxy populations peak at *AB* mag ~ 20–21 with little additional contribution out to $AB \gtrsim 28$ [see, e.g., the detailed discussions by Kashlinsky (2005a) and Driver *et al.* (2016)]. Figure 2 also shows the reconstructed CIB from known
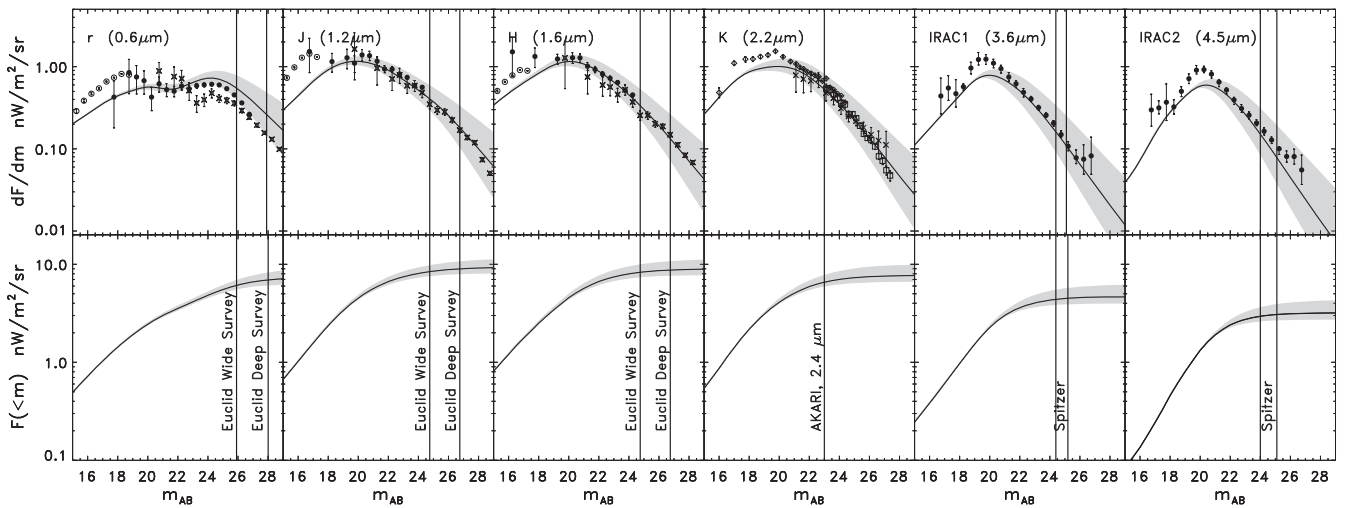
FIG. 2. Differential and cumulative flux from data vs HRK12 reconstruction [shaded bands span the range from the high-faint end (HFE) to the low-faint end (LFE) with the solid lines showing the default reconstructions]. Diffuse fluxes at the *r*, *J*, and *H* bands are obtained using counts from Fig. 12 of Windhorst *et al.* (2011) in the same notation, *K* counts from Keenan *et al.* (2010) (open squares) and Maihara *et al.* (2001) (crosses), and at 3.6 and 4.5 μm the Infrared Array Camera (IRAC) counts from Ashby *et al.* (2013, 2015) are used at $m_{AB} > 16$, where they are less polluted by Galactic star counts. In the *K* band, Fontana *et al.* (2014) presented more updated counts, which are consistent with what is shown, but extend to shallower magnitudes ($m_{AB} < 26$) and are not displayed here for clarity.

TABLE I. HRK12 reconstruction of diffuse flux (nW/m²/sr).

	r	J	H	$K/2.4\mu m$	$3.6\ \mu m$	$4.5\ \mu m$
Net F	$7.5^{+2.5}_{-1.2}$	$9.4^{+2.4}_{-1.3}$	$9.0^{+2.5}_{-1.2}$	$7.7^{+2.4}_{-1.1}$	$4.7^{+1.6}_{-0.7}$	$3.2^{+1.2}_{-0.5}$
m_0	26	24.5	24.5	23	25	25
$F(>m_0)$	$1.4^{+1.6}_{-0.6}$	$1.0^{+1.0}_{-0.4}$	$0.8^{+0.9}_{-0.3}$	$1.1^{+1.1}_{-0.4}$	$0.2^{+0.4}_{-0.1}$	$0.14^{+0.31}_{-0.08}$

populations with the methodology of Helgason, Ricotti, and Kashlinsky (2012) (HRK12) discussed later in Sec. VI.B. This heuristic reconstruction follows the counts data very accurately, especially at the faint end relevant here; the small deviations at the bright end may be due to pollution from star counts and other systematics. Table I gives the CIB estimates in the HRK12 reconstruction for all galaxies and for those remaining below current or future limiting magnitudes. These agree well with the net CIB flux integrated directly from galaxy counts [Table 5 of Kashlinsky (2005a)]; see also Fig. 4 of Driver *et al.* (2016) for updated diffuse fluxes from counts (Beckwith *et al.*, 2006; Bouwens *et al.*, 2010; Windhorst *et al.*, 2011).

Driver *et al.* (2016) derived from compiling counts survey data the net EBL of 24 ± 4 nW/m²/sr between UV and $10\ \mu m$ and 26 ± 5 nW/m²/sr in far IR, 10–1000 μm. Integrating in the near-IR range of $[1–5]\ \mu m$ would give 9^{+3}_{-1} nW/m²/sr for the CIB contribution of known sources according to the HRK12 reconstruction.

The upshot of this discussion is that (1) galaxy counts from known populations produce finite CIB out to at least $m_{AB} \gtrsim 28$, (2) these counts are well approximated with the heuristic CIB and EBL reconstruction developed by Helgason, Ricotti, and Kashlinsky (2012) HRK12, and (3) any excess CIB, if found, must then arise in new populations, which are too faint or too distant to be detected, or both.

B. Direct measurements of CIB

The subtraction of Solar System and Galactic foregrounds (Leinert *et al.*, 1998) from space-based measurements of the absolute sky brightness yields direct measurements of the mean CIB. Observations are usually obtained over multiple wavelengths, and mean CIB estimates are derived by averaging data over large areas. This approach was adopted by both the COBE Diffuse Infrared Background Experiment (DIRBE) and the Infrared Telescope in Space (IRTS) Near-Infrared Spectrometer instruments and its results were reviewed extensively before (Hauser and Dwek, 2001; Kashlinsky, 2005a). Here we briefly review only the new results on the mean near-IR CIB that appeared since the Kashlinsky (2005a) review.

There have been several efforts to apply new modeling and analysis techniques to existing data sets to make improved estimates of the mean CIB. Updated results from the DIRBE measurements have been provided by Levenson and Wright (2008) and Sano *et al.* (2015, 2016). The IRTS data were reexamined by Matsumoto *et al.* (2015). These reanalyses generally lead to smaller systematic uncertainties than earlier estimates, but similar to earlier work, they point to the presence of $\sim$1–5 μm IR emission in excess of that expected from the integrated light of known galaxies (and zodiacal and Galactic foregrounds). New independent observations of the

sky brightness by the AKARI spacecraft also reinforce this picture (Tsumura *et al.*, 2013). New observations from the Cosmic Infrared Background Experiment (CIBER) suborbital mission extend the CIB measurements to shorter wavelengths, but indicate that the spectrum is flattening or falling from 1.25 to 0.8 μm (Matsuura *et al.*, 2017). Deep Hubble Space Telescope (HST) Near-Infrared Camera and Multiobject Spectrometer (NICMOS) observations have been analyzed by Thompson *et al.* (2007a, 2007b), who reported no near-IR CIB excess above the levels contributed by known galaxies to within a few nW/m²/sr. However, the empirical method they apply is sensitive to structure in the CIB, but does not distinguish the mean CIB from the empirically subtracted zodiacal light.

Figure 3 displays the recent mean CIB measurements. Lower limits derived from the integration of the fluxes of resolved galaxies are well below the mean CIB at 0.8–4 μm. While the currently claimed direct mean CIB levels are in tension with constraints from γ-ray absorption (see Sec. III.C), the CIB levels implied by the current fluctuation measurements, a few nW/m²/sr, can be comfortably accommodated.

The primary difficulty with all direct measurement of the CIB and the interpretation of these measurements is the large uncertainty associated with the subtraction of bright foregrounds, particularly the zodiacal light. Dwek, Krennrich, and Arendt (2005) proposed that the similarity of the energy
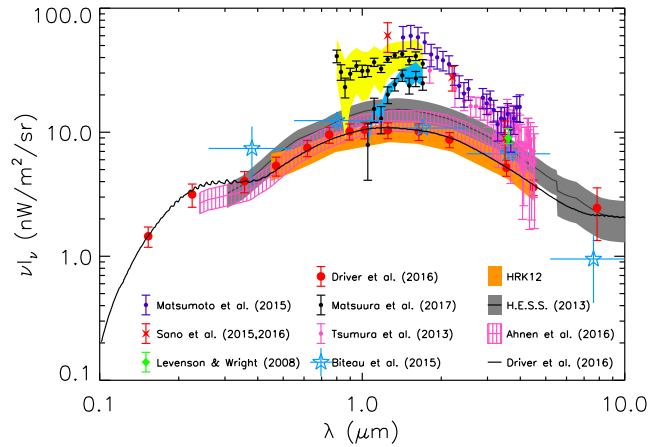
FIG. 3. The spectral energy distribution (SED) of the mean CIB as derived from recent direct measurements and reanalyses: Levenson and Wright (2008) (green diamond), Sano *et al.* (2015, 2016) (red crosses), Matsumoto *et al.* (2015) (violet dots), Tsumura *et al.* (2013) (pink dots), Matsuura *et al.* (2017) [black dots with yellow and blue systematic uncertainty bands are derived with subtraction of the Kelsall *et al.* (1998) and Wright (1998) zodiacal light models, respectively]. The Thompson *et al.* (2007a, 2007b) limit on the net CIB at 1.1 and 1.6 μm is within 3–4 nW/m²/sr of the level given by known galaxy counts. The orange band shows the HRK12 CIB, reconstructed from galaxy counts, bounded by its high-faint-end (HFE) to low-faint-end (LFE) uncertainties. Also shown are the modeled (black line) and measured (large red circles) CIB extrapolated from integrated galaxy counts by Driver *et al.* (2016). Levels of CIB and EBL inferred from γ-ray absorption are shown from Abramowski *et al.* (2013) (gray band), Ahnen *et al.* (2016) (striped pink band), and Biteau and Williams (2015) (blue stars). Adapted from Driver *et al.*, 2016.

spectra suggested that incompletely modeled zodiacal light could be responsible for the apparent CIB excess. However, with extension to shorter wavelengths, the similarity is less clear (Tsumura *et al.*, 2010).

It was noted (Cooray *et al.*, 2009) that a mission outside the interplanetary dust cloud can make greatly improved mean CIB and COB determination due to the reduction of the zodiacal light. Greenhouse *et al.* (2012) and Matuura *et al.* (2014) presented concept studies for such a mission. Studies using Pioneer (Toller, 1983) and New Horizons (Zemcov *et al.*, 2017) data set upper COB limits.

The uncertainties associated with foregrounds can be reduced with the analysis of the CIB fluctuation rather than its mean intensity. Fluctuation measurements were pioneered in the CIB context of DIRBE data by Kashlinsky, Mather, and Odenwald (1996), Kashlinsky *et al.* (1996), and Kashlinsky and Odenwald (2000). At optical wavelengths, such methodology was explored earlier by Shectman (1973, 1974).

C. Limits from γ-ray absorption

CIB emissions may provide a source of abundant photons at high z. The present-day value of I_ν corresponds to a comoving number density of photons per logarithmic energy interval $d \ln E$ of

$$\frac{4\pi}{c}\frac{I_\nu}{h_{\text{Planck}}} = 0.01(I_\nu/0.016 \text{ MJy sr}^{-1}) \text{ cm}^{-3}$$

and if these photons come from high z their number density would increase as $\propto (1+z)^3$ at early times. These photons with the present-day energies E would also have higher energies in the past and they would thus provide absorbers for sources of sufficiently energetic photons via $\gamma\gamma_{\text{CIB}} \rightarrow e^+e^-$ when $E'_\gamma \mathcal{E}'_{\text{CIB}} \geq (m_e c^2)^2$ (Nikishov, 1962; Gould and Schréder, 1967). The $\gamma\gamma$ absorption, being electromagnetic in nature, has a cross-section magnitude similar to that for the Thomson scattering σ_T: it is given by

$$\sigma = \frac{3}{16}\sigma_T(1-\beta^2)\left[2\beta(\beta^2-2) + (3-\beta^4)\ln\left(\frac{1+\beta}{1-\beta}\right)\right],$$

where

$$\beta = \left[1 - \frac{2m_e^2 c^4}{E' \mathcal{E}'(1-\cos\theta)}\right]^{1/2},$$

and E and $\mathcal{E}$ are the present-day energies of the CIB and γ-ray photons respectively; the primes denote rest-frame energies, e.g., $E' = E(1+z)$. The cross section has a sharp cutoff as $\beta \rightarrow 1$, peaks at $\simeq(1/4)\sigma_T$ at $\beta \simeq 0.7$, and is $\sigma \propto \beta$ for $\beta \lesssim 0.6$. The mean free path of γ-ray photons in the presence of CIB would be $(n_{\gamma_{\text{CIB}}}\sigma)^{-1} \sim 0.8(\sigma_T/\sigma)(1 \text{ MJy sr}^{-1}/I_\nu)(1+z)^{-3}$ Mpc. Figure 4, top, shows the CIB expressed as I_ν and as the comoving photon number density times $\sigma_T c H_0^{-1}$, along with regions defined by the $\gamma\gamma$ absorption threshold.

This interaction generates absorption at sufficiently high γ-ray energies for a given IR or optical wavelength (marked in Fig. 4, top). Measuring this absorption provides independent
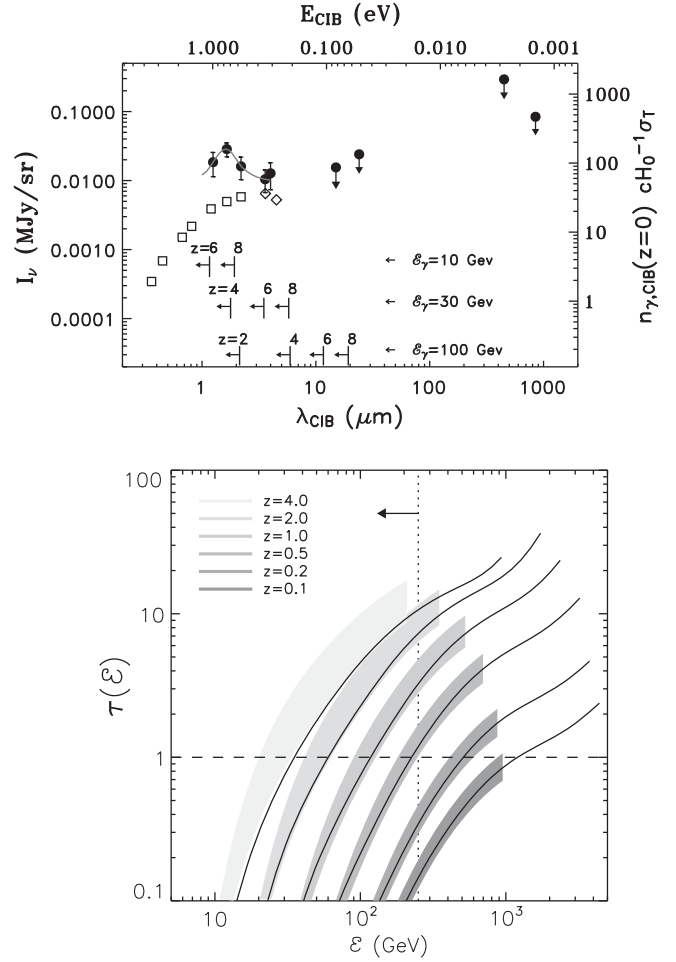
FIG. 4. Top: Filled circles show the CIB excess claimed by the IRTS analysis at near-IR (Matsumoto *et al.*, 2005) as derived by Kashlinsky (2005a) and the open squares show the integrated counts. Vertical bars with left-pointing arrows show the range where photon-photon absorption is possible for the redshifts and energies indicated. Adapted from Kashlinsky, 2005b. Bottom: Solid lines show the $\gamma\gamma$ optical depth out to the marked z vs the observer γ-ray energy using the default reconstruction of Helgason, Ricotti, and Kashlinsky (2012) and the shaded regions show the boundaries of the HRK12 reconstruction. The dashed horizontal line marks $\tau = 1$. The figure shows that the Universe is already optically thick to TeV photons at $z \gtrsim 0.1$. Adapted from Helgason and Kashlinsky, 2012.

constraint on the CIB and its evolution with z. However, the net diffuse flux probed in this way is not source subtracted and is not wavelength specific. If significant CIB comes from high-z sources, it would have provided a far more abundant source of photons at high z which interact with photons of present-day energy $\mathcal{E} \gtrsim 2M_e^2 c^4/E' \gtrsim 30(1+z)$ GeV so that even a moderate CIB from first stars era could be identified in spectra of γ-ray sources at $z \gtrsim 3$–5 (Kashlinsky, 2005b). Helgason and Kashlinsky (2012) reconstructed τ from known sources with the multiwavelength reconstruction of Helgason, Ricotti, and Kashlinsky (2012). This gives the minimal absorption and shows that TeV photons are fully absorbed from nearby ($z \lesssim 1$) sources (Fig. 4), and so to probe first stars era with this method more directly one needs GeV photons.

Dwek, Arendt, and Krennrich (2005) and Aharonian *et al.* (2006) examined the strong CIB in the context of γ-ray absorption toward blazars and production from Population III systems. They conclude that Population III systems are unlikely to contribute much to the CIB excess claimed in the IRTS and DIRBE studies, although such statements quantitatively depend on the assumed spectral energy distribution (SED) of EBL (Kashlinsky and Band, 2007). Ackermann *et al.* (2012) detected attenuation from EBL in the combined sample of Fermi blazars out to $z \simeq 1.6$. Figure 3 shows CIB and EBL levels from Abramowski *et al.* (2013), Biteau and Williams (2015), and Ahnen *et al.* (2016). Constraints from the observed γ-ray absorption (Abramowski *et al.*, 2013) give upper limits of 17 and 14 nW m^{-2} sr^{-1} at 1.1 and 1.6 μm. This is to be compared with the resolved CIB from faint galaxy counts estimated in Table I at these bands. Thus $\lesssim 8$ and 5 nW m^{-2} sr^{-1} currently appear feasible in CIB excess at these wavelengths.

Constraints may, however, be less restrictive because of an alternative suggested explanation of secondary TeV photons produced by the interaction of cosmic rays and EBL (Essey *et al.*, 2010; Essey and Kusenko, 2010). In that interpretation, the intrinsic spectra of blazars at TeV energies have absorption due to high CIB levels, but appear unabsorbed because cosmic rays (protons) from the blazar jets interact with lower energy EBL along the line of sight to produce pions and secondary γ rays, when $E_p E_{EBL} \geq (m_\pi c^2)^2$. Those secondary γ rays coincide with the blazar within the angular resolution of the Cherenkov telescopes because the intergalactic magnetic fields are weak ($\lesssim 10^{-14}$ G) and unable to deflect the cosmic ray protons from the line of sight.

D. Resolved cosmic x-ray background

The CXB was discovered by Giacconi *et al.* (1962) in a rocket flight originally designed to detect x-ray emission from the Moon; the CXB was the first cosmic background discovered. The shape of the CXB spectrum in the 3–50 keV range was first determined by the High Energy Astronomy Observatory-1 (HEAO-1) (Marshall *et al.*, 1980) and shows a pronounced maximum emitted energy in the 20–30 keV range. Figure 5 (Cappelluti *et al.*, 2017) summarizes the best measurements to date. The measurement of the absolute level of the x-ray background is complicated, because of systematic uncertainties in the instrument responses as well as the instrumental background and solid angle characteristics. Additionally, there are systematic differences in the contribution of relatively bright x-ray sources, which are present in wide-field collimated instruments and typically avoided in narrow-field imaging surveys. Thus, throughout the history of CXB measurements there have been systematic differences in the measured absolute CXB intensity, which are partially reflected in Fig. 5. There is a 10%–20% difference between the minimum and maximum flux measured in the energy range 1–20 keV, corresponding to a systematic CXB flux uncertainty of ~1–2 keV/cm^2/s/sr around 1 keV.

X-ray surveys are practically the most efficient means of finding active galactic nuclei (AGN) over a wide range of luminosity and redshift. Deep surveys with focusing x-ray telescopes on ROSAT, Chandra, and the X-ray Multimirror
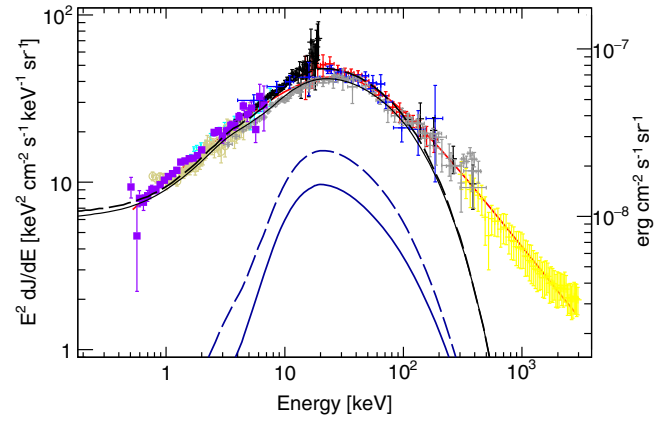

FIG. 5. Compilation of independent measurements of the CXB spectrum from several different instruments in the 0.5–500 keV range. The magenta data points have been recently derived from the Chandra legacy data in the Cosmological Evolution Survey (COSMOS) field. Adapted from Cappelluti *et al.*, 2017; see references therein for the individual data sets. The lines show population synthesis model curves using the Gilli, Comastri, and Hasinger (2007) model as applied by Comastri *et al.* (2015). The thin solid and thick solid lines show the total active galactic nuclei (AGN) spectrum and the contribution of Compton-thick AGN in the model, respectively. The dashed curves show the same information, but assume a 4 times larger abundance of the heavily absorbed Compton-thick AGN. The flux of $1 \, \text{keV}^2 \, \text{cm}^{-2} \, \text{keV}^{-1} \, \text{sr}^{-1} = 1.6 \times 10^{-9} \, \text{erg} \, \text{cm}^{-2} \, \text{sr}^{-1}$ as shown in the right vertical axis.

Mission (XMM)-Newton have resolved the majority of the extragalactic CXB into faint discrete x-ray sources. Enormous multiwavelength photometric and spectroscopic follow-up efforts have identified optical and/or near-IR counterparts to most of these sources and have shown that the main contributors to the CXB are indeed AGN at redshifts up to $z \sim 5$ (Brandt and Hasinger, 2005; Brandt and Alexander, 2015). One of the key observational tools is the determination of the x-ray luminosity function of these AGN, and its cosmological evolution, which gives strong constraints on the accretion history of the Universe. The best-fit model for the distribution of AGN as a function of luminosity and redshift is the so-called "luminosity-dependent density evolution," which shows a strong dependence of the AGN space density evolution on x-ray luminosity, with a clear increase of the peak space density redshift with increasing x-ray luminosity. This "AGN cosmic downsizing" evolution is seen in both the soft x-ray (0.5–2 keV) and the hard x-ray (2–10 keV) bands (Ueda *et al.*, 2014; Miyaji *et al.*, 2015; Fotopoulou *et al.*, 2016), as well as in other wavebands (Hasinger, 2008).

The spectral shape of the CXB was a puzzle for some time, because it does not resemble typical AGN spectra. The resolution came from cosmological population synthesis models, where the evolving AGN luminosity function is folded with sophisticated AGN spectral model templates including the Compton reflection hump and a wide distribution of neutral gas absorption column densities from unabsorbed heavily Compton-thick absorption (Comastri *et al.*, 1995; Gilli, Risaliti, and Salvati, 1999; Ueda *et al.*, 2003, 2014; Ballantyne *et al.*, 2006; Gilli, Comastri, and Hasinger,
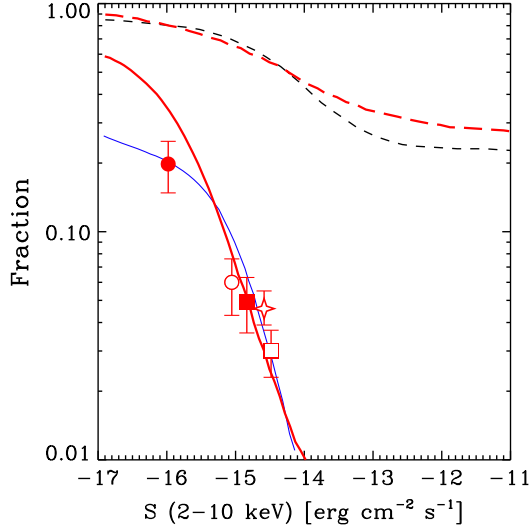
FIG. 6. Observed fractions of Compton-thick AGN by Brightman and Ueda (2012) and references therein are shown by symbols with error bars. Adapted from Ueda *et al.*, 2014. Predictions from population synthesis models of Gilli, Comastri, and Hasinger (2007), adapted from Comastri *et al.* (2015) and Ueda *et al.* (2014) for Compton-thick AGN fractions ($\log N_H = 24$–26, thick red, solid blue) and all obscured AGN ($\log N_H = 22$–26, dashed red, dashed black) in the total AGN are given as a function of the observed 2–10 keV flux.

2007; Treister, Urry, and Virani, 2009). In these models most of the AGN emission in the Universe is significantly absorbed by intervening gas and dust clouds, which is also the reason for the characteristic 20–30 keV peak of the x-ray background spectrum.

Compton-thick AGN, where most primary x-ray emission is absorbed by a large column density of intervening material and only a very small reflected soft component escapes, are hard to detect and therefore elusive in existing deep x-ray surveys. Figure 6 summarizes our current knowledge of the relative fraction of observed Compton-thick AGN as a function of the x-ray flux, compared to the population synthesis models. There are still significant uncertainties in the actual contribution of Compton thick to the luminosity function and cosmic evolution of AGN, and thus their contribution to the accretion history of the Universe.

Through the studies of the x-ray background and large samples of black holes in nearby galaxies, it has become clear that supermassive black holes at the centers of galaxies must play an important role in the cosmic evolution of galaxies. AGN and galaxies in general undergo very similar evolution patterns, where the peaks of AGN activity and star formation occur in the same redshift range ($z = 1.5$–2) and show a similar dramatic decline (downsizing) toward lower z. Strong correlations have been found between the BH mass and global properties of its host galaxy spheroid, such as the bulge luminosity (Kormendy and Richstone, 1995; Magorrian *et al.*, 1998) and the stellar velocity dispersion, i.e., the $M_{BH} - \sigma$ relation (Ferrarese and Merritt, 2000; Gebhardt *et al.*, 2000). Using these correlations, the mass density of local dormant supermassive black holes in galaxy centers has been estimated and is found largely consistent with the mass density accreted

by AGN throughout the history of the Universe (Marconi *et al.*, 2004; Merloni, 2004), yielding further evidence for a tight link between the growth of galaxy bulges and of their nuclear black holes through standard, high-efficiency accretion processes.

However, a recent comprehensive analysis of black hole mass measurements and scaling relations concluded that the canonical black-hole-to-bulge mass ratio, instead of being constant for all galaxies with values around ∼0.1%–0.23% (Merritt and Ferrarese, 2001; Marconi and Hunt, 2003), actually shows a mass dependence and varies from 0.1%–0.2% at $M_{bulge} \sim 10^9 M_\odot$ to ∼0.5% at $M_{bulge} = 10^{11} M_\odot$ (Graham and Scott, 2013; Kormendy and Ho, 2013). However, Shankar *et al.* (2016) argued that these analyses are overestimating black hole masses and hence AGN counts. The revised normalization would lead to a dramatically (a factor of 2 to 5) *larger* estimate of the local BH mass density, which is dominated by massive bulges. Conversely to the previous findings, this result means that there must be other significant channels for BH growth, apart from those assumed in the standard population synthesis model for the CXB. Like others before, Comastri *et al.* (2015) pointed out that the systematic uncertainty in the normalization of the CXB spectrum allows significant contributions of so far undetected populations of heavily shrouded Compton-thick AGN without violating other observational constraints, e.g., in the midinfrared. The dashed curve in Fig. 5 shows a variant of the population synthesis model, where the contribution of heavily obscured, i.e., reflection-dominated Compton-thick AGN has been increased by a factor of 4 with respect to the standard model. This already goes some way toward augmenting the local BH mass density, but is not sufficient. Comastri *et al.* (2015) therefore had to assume another, so far undetected component of BH mass growth, e.g., BHs which are completely shrouded by obscuring material and only radiate at mid-IR wavelengths. However, one major uncertainty in these estimates is the unknown cosmological evolution of the obscuration fraction (Treister and Urry, 2006; Hasinger, 2008). There is also mounting evidence that the fraction of galaxy mergers is significantly higher among Compton-thick AGN compared to the normal CXB population (Kocevski *et al.*, 2015; Kocevski, 2017). In particular, at high redshifts, where galaxy mergers are expected to be more common, obscured accretion can play a much larger role than locally.

IV. THEORY BEHIND CIB FLUCTUATION STUDIES

A. CIB fluctuations primer

1. Theoretical basis

CIB is a decisive tool when sources of interest are fainter than the sensitivity limits of the instrument or are too numerous to be individually resolved (i.e., are confused) at the instrument's angular resolution. The goal is to probe CIB levels from faint populations below the (ideally low) threshold defined by instrument noise and resolution, i.e., $F_{CIB}(m > m_{lim})$. For a sufficiently faint removal threshold, and suitable λ, the hope is that one would move sufficiently far along the redshift cone to probe the earliest sources.

The rate of the net CIB flux production probed in the observer band at wavelength λ is

$$\frac{dF_\lambda}{dz} = \frac{c}{4\pi} \mathcal{L}_{\lambda'}(z) \frac{1}{1+z} \frac{dt}{dz}, \qquad (1)$$

where $\mathcal{L}(z)$ is the comoving luminosity density at the rest wavelength λ'. Emissions from astrophysical sources in the rest-frame UV are cut off at the Lyman break due to absorption by the intergalactic medium (IGM), which happens at rest $\lambda_{Ly} = 0.0912$ μm if the IGM is fully ionized or at the Lyα of $\lambda_{Ly} = 0.1216$ μm if it contains mainly H I.

In the Cartesian limit (small angles), CIB fluctuations can be Fourier transformed,

$$\Delta(\vec{q}) = \frac{1}{4\pi^2} \int \delta F(\vec{x}) \exp(-i\vec{x} \cdot \vec{q}) d^2x,$$

and characterized by the two-dimensional projected power spectrum $P(q) = \langle |\Delta(\vec{q})|^2 \rangle$ as a function of the angular frequency q (or angular scale $2\pi/q$). A typical rms flux fluctuation is $\sqrt{q^2 P(q)/2\pi}$ on the angular scale of wavelength $2\pi/q$. Theoretically there are two types of contributions relevant for interpretation of the measured cosmological projected (2D) power spectrum of source-subtracted CIB fluctuations: (1) shot noise from remaining sources occasionally entering the beam, and (2) the clustering component that reflects clustering of the remaining CIB sources.

The shot-noise power is given by (Kashlinsky, 2005a)

$$P_{SN} = \int_{m_{lim}}^{\infty} S^2(m) \frac{dN}{dm} dm \qquad (2)$$

where m_{lim} is the limiting magnitude of sources remaining in the source-subtracted CIB map, $S(m)$ is the flux of a source of AB magnitude m, and dN/dm is the number counts of the sources per dm. This component is intrinsically white, but convolved with the instrument beam.

When interpreting observations, it is useful to consider the shot noise as follows: source-subtracted CIB fluctuations are measured at a given shot-noise level, which per Eq. (2) defines the equivalent effective magnitude (or flux) of source removal. The net mean CIB flux from sources remaining in the data is then $F_{CIB}(m > m_{lim}) = \int_{m_{lim}}^{\infty} S(m)(dN/dm)dm$. Hence the remaining shot noise is connected to the remaining CIB as $P_{SN} \sim S(\bar{m})F_{CIB}$ with $\bar{m}$ being the effective magnitude of the remaining populations (Kashlinsky *et al.*, 2007c). When discussing observational results the shot-noise power will be expressed in units of $[P_{SN}] = \text{nJy nW/m}^2/\text{sr}$ which is equivalent to $3/\lambda(\mu\text{m}) \times 10^{-12}$ $\text{nW}^2/\text{m}^4/\text{sr}$. Measurements of the diffuse flux CIB fluctuations will be expressed in units of $[\sqrt{q^2 P/(2\pi)}] = \text{nW/m}^2/\text{sr}$.

The clustering component is generally made up of two terms (Cooray and Sheth, 2002): the 1-halo term and the 2-halo term. The 1-halo term is essentially a white noise term convolved with an "average" halo profile of the remaining sources and so reflects an average halo profile below angular scales subtending a typical halo. It is unimportant for high-z sources, but may be important for more local extended ones. The projected 2-halo term is related to the underlying 3D

power P_{3D} of the sources by the relativistic Limber (1953) equation

$$\frac{q^2 P_\lambda(q)}{2\pi} = \int_0^{z_{Ly}(\lambda)} \left(\frac{dF_{\lambda'}}{dz}\right)^2 \Delta^2(qd_A^{-1}; z) dz, \qquad (3)$$

where

$$\Delta^2(k, z) \equiv \frac{k^2 P_{3D}(k, z)}{2\pi cH^{-1}(z)}$$

is the mean square fluctuation in the source counts over a cylinder of diameter k^{-1} and length $cH^{-1}(z)$ and $dF_{\lambda'}/dz$ is the CIB flux production at rest $\lambda' \equiv \lambda/(1+z)$ over the epochs spanned by the integration (Cooray *et al.*, 2004; Kashlinsky *et al.*, 2004; Fernandez *et al.*, 2010; Kashlinsky, Arendt *et al.*, 2015; Helgason *et al.*, 2016). Because cosmological sources have a Lyman break due to IGM absorption by H I at rest wavelength λ_{Ly}, the integration stops at $z_{Ly}(\lambda) = \lambda/\lambda_{Ly} - 1$ because at larger redshifts sources emit only longward of the Lyman-break wavelength; the integration extends only to the redshift specified by the far edge of the filter for band λ. This will be used in the Lyman tomography in Sec. IV.D.7.

The density field is today linear on scales $> r_8$ and the scale of nonlinearity is smaller at higher z. It is reasonable to assume that on linear scales the density of luminous sources traces that of the underlying matter to within a scale-independent bias factor. For reference, the angular scale of $1'$ subtends 1.1, 1.4, 1.5, and 1.6 h^{-1} Mpc at $z = 5, 10, 15,$ and 20. As Fig. 1 shows, the density field on these scales is in linear regime at $z \gtrsim 8$–10. We assume a ΛCDM template for P_{3D} in Eq. (3) for the high-z contributions to CIB fluctuations on arcminute scales and beyond. If the range of z spanned by the populations that are probed is narrow, as can arise if lower-z sources are removed and very high-z sources do not enter beyond z_{Ly}, one can relate CIB fluctuations to the net CIB flux as $\delta F(2\pi/q) \sim F_{CIB}\Delta(qd_A\bar{z})$, where $\bar{z}$ is a suitably averaged redshift of the sources.

Let us assume that a fraction f_{Halo} of all matter in the Universe collapses in halos capable of producing luminous sources at a given redshift, converting on average a fraction f_* of the halo baryons into luminous sources. The bolometric diffuse flux produced by these populations, after they have converted their mass into energy with radiation efficiency ϵ, is

$$F_{tot} \simeq f_{Halo} f_* \left(\frac{c}{4\pi} \epsilon \rho_{baryon} c^2\right) z_{eff}^{-1}$$

$$\simeq 9.1 \times 10^5 \epsilon f_{Halo} f_* z_{eff}^{-1} \frac{\Omega_{baryon} h^2}{0.0227} \frac{\text{nW}}{\text{m}^2 \text{sr}}, \qquad (4)$$

where $z_{eff} \equiv 1/\langle (1+z)^{-1} \rangle$ is a suitably averaged effective redshift factor which accounts for the radiation energy density decreasing with expansion as $\propto (1+z)^{-4}$ vs the matter density $\propto (1+z)^{-3}$.

2. Observationally determined quantities and their uncertainties

Once CIB maps are produced for a square field of width Θ, the diffuse flux is Fourier transformed with pixels in the

Fourier plane having a width of $\Delta q = 2\pi/\Theta$. Because flux is a real quantity, only half of the Fourier plane is independent. The power spectrum is defined as $P(q) = \langle|\Delta(\vec{q})|^2\rangle$, where $\Delta(\vec{q})$ is the 2D FT of the source-subtracted CIB. For ease of comparison with background intensities, we plot results as the mean squared fluctuation at angular scale $2\pi/q$, defined as $q^2 P(q)/(2\pi)$. For spherical harmonic expansion $\delta F(\theta, \phi) = \sum a_{\ell, m} Y_{\ell, m}(\theta, \phi)$, the power is

$$C_\ell = \langle|a_{\ell,m}|^2\rangle_m = \frac{1}{2\ell+1} \sum_{m=-\ell}^{\ell} |a_{\ell,m}|^2.$$

At small angular scales, the multipole in spherical harmonic expansion is related to the angular wave number via $\ell \simeq q$ (in rad^{-1}).

The cross power describing the correlations between fluctuations at different wavelengths (1,2) is $P_{1\times2}(\vec{q}) = \langle\Delta_1(\vec{q})\Delta_2^*(\vec{q})\rangle = \langle[\mathcal{R}_1(\vec{q})\mathcal{R}_2(\vec{q}) + \mathcal{I}_1(\vec{q})\mathcal{I}_2(\vec{q})]\rangle$ with $\mathcal{R}$ and $\mathcal{I}$ standing for the real and imaginary parts of the Fourier transform $\Delta(\vec{q})$. The cross-power spectrum is a real quantity which can be positive or negative.

The correlation function $C(\theta) = \langle\delta F(\vec{x})\delta F(\vec{x} + \vec{\theta})\rangle$ and the 2D power are interrelated via an integral transform, which in the limit of small angles $\theta \ll 1$ rad is

$$C(\theta) = \frac{1}{2\pi} \int_0^\infty P(q) J_0(q\theta) q \, dq$$

and

$$P(q) = 2\pi \int_0^\infty C(\theta) J_0(q\theta) \theta \, d\theta$$

with J_0 being the cylindrical Bessel function of zeroth order. Any white noise power, such that $P = $ const, results in $C(\theta) \propto \delta_D(\theta)$ and directly translates only into the zero-lag value of the correlation function (i.e., variance). The shot-noise component is white noise convolved with the beam and will be reflected in the correlation function values only up to roughly the beam scale. Nonzero values of the correlation function on scales much greater than the beam reflect a nonwhite power from clustering; e.g., a power law $C \propto \theta^{(n-2)}$ corresponds to $P(q) \propto q^{-n}$.

The coherence between the two bands is defined as

$$\mathcal{C}_{12} \equiv \frac{P_{12}^2}{P_1 P_2}.$$

It should lie between 0 and 1 (no to full coherence).

We now turn to errors and uncertainties for the measured quantities: autopowers, cross powers, and coherence. We assume that the underlying $\Delta(\vec{q})$ is Gaussian distributed, but note that this may be affected by biasing (Kaiser, 1984; Bardeen *et al.*, 1986; Jensen and Szalay, 1986; Kashlinsky, 1991, 1998).

The errors on the power measured from a finite size field are subject to the sampling ("cosmic") variance (Abbott and Wise, 1984). Namely, if the power $\hat{P}$ at the central wave number q is determined from a total of N_q independent pixels in the

Fourier plane, the error on this measurement is $\sigma_P = \hat{P}/\sqrt{N_q}$. Because the autopower is a quadratic quantity and is χ^2 distributed, this approximation does not correspond to the standard 68% confidence limit at the very largest scale, where $N_q \sim 1$–2, but at smaller scales it is a reasonable approximation. An additional issue is that masking of resolved sources in the maps generates coupling between various Fourier harmonics thereby biasing or distorting the measurement of the power from FT because of the convolution with mask. Thus one should proceed with caution and verify the power results from fast Fourier transform (FFT) with the much more CPU intensive computation of the correlations function (Kashlinsky *et al.*, 2005; Matsumoto *et al.*, 2011), which is immune to masking effects. In practice, when $\lesssim 30\%$–35% of the maps are masked there is good consistency between the two approaches (Kashlinsky *et al.*, 2005), but the two can at times diverge for much more aggressive masking with the correlation function being a more reliable estimate (Kashlinsky, 2007).

The cross power for uncorrelated quantities can be both positive and negative and would be distributed in a Gaussian manner if the underlying quantities are Gaussian distributed. The cosmic variance error on its measurement from the same field at two different bands is $\sigma_{P_{12}} \simeq \sqrt{P_1 P_2/N_q}$ (Cappelluti *et al.*, 2013).

For errors on the coherence, or the square of the correlation coefficient $\mathcal{R}$, the situation is more complicated since statistical errors must be evaluated from the confidence contours of the quantity of interest ($\mathcal{C} \equiv \mathcal{R}^2$ here), which must be derived from its underlying probability distribution function. Because of the highly nonlinear structure of $\mathcal{R}$ with respect to the underlying quantities in both the numerator and the denominator, its probability distribution function is not trivially derivable. However, once the errors on the power at each q are determined, one can then propagate them via the Fisher transformation (Fisher, 1915) to give the confidence contours of the resultant correlation coefficient. Because errors are always equivalent to confidence contours, one needs to evaluate the 68% confidence limits of $\mathcal{R}$ from the errors on the power. The Fisher transformation technique represents the standard way to evaluate the probability distribution of $\mathcal{R}$ and relate the uncertainties to those of the powers. The Fisher transformation works as follows: One evaluates the central value $\mathcal{R}_0 \equiv \sqrt{\mathcal{C}_0}$ of the correlation coefficient from the power data. The Fisher transformation is to compute the quantity

$$\mathcal{Z} = \frac{1}{2} \ln\left[\frac{(1+\mathcal{R})}{(1-\mathcal{R})}\right],$$

which is normally distributed in most practical cases (Fisher, 1915). This transformation, and its inverse $\mathcal{C} = [\tanh(\mathcal{Z})]^2$, is then used to construct the corresponding confidence interval for $\mathcal{C}$: one evaluates the 68% contours of $\mathcal{Z}$ from the variances of the autopowers and cross powers, assumed to be equivalent to the 68% confidence levels. The variance in $\mathcal{Z}$ is related to the errors on powers as

$$\sigma_{\mathcal{Z}}^2 = \frac{\mathcal{C}_0}{(1-\mathcal{C}_0)^2}\left[\frac{\sigma_{P_{12}}^2}{P_{12}^2} + \frac{1}{4}\frac{\sigma_{P_1}^2}{P_1^2} + \frac{1}{4}\frac{\sigma_{P_2}^2}{P_2^2}\right].$$

The 68% contours for $\mathcal{C}$ are derived from $\mathcal{Z} \pm 1\sigma_{\mathcal{Z}}$, 95% from $\mathcal{Z} \pm 2\sigma_{\mathcal{Z}}$, etc. The confidence contours for $\mathcal{C}$ are thus constrained to the interval of [0, 1] (and [−1, 1] for $\mathcal{R}$).

B. Contribution from remaining known galaxy populations

Helgason, Ricotti, and Kashlinsky (2012) developed a robust heuristic way of reconstructing CIB fluctuations from galaxy populations spanning wavelengths from UV to mid-IR out to $z \sim 6$. The assembled database for the reconstruction now covers over 340 luminosity function (LF) surveys from UV to mid-IR (HRK12, Helgason and Kashlinsky, 2012; Helgason *et al.*, 2014), and the methodology allows filling in the redshift cone with known galaxies across the required wavelengths.

The HRK12 methodology works as follows: the LF in the optical and near-IR can be well described by the Schechter (1976) function parametrized by $M^\star$, $\phi^\star$, and α. Table I in HRK12 shows the measured Schechter parameters from multiple surveys as a function of both rest-frame wavelength and redshift. Whereas $M^\star$ and $\phi^\star$ are well measured out to large distances, the faint-end slope α is poorly constrained and often is simply kept fixed in fits. Deep near-IR number counts provide the best constraints on the faint-end LF slope as they are dominated by the faint end of the LF at $z \sim 1$–3, where measuring α directly becomes challenging. In other words, the faint galaxy counts at 1–5 μm sample the faint end of the LF at different rest-frame wavelengths at intermediate z where the volume density of sources per solid angle is at a maximum. More importantly, compared to the LF, the uncertainties in the counts are robust, i.e., they are not affected by systematic uncertainties associated with redshift determinations or degeneracy in the best-fit Schechter parameters. The only assumptions in the reconstruction are (1) the LF is well described by the Schechter function, and (2) that the evolution and spectral behavior of α is smooth and does not exhibit sudden changes in a narrow interval. The uncertainties of the reconstruction, around the default model, are bracketed by the HFE and LFE limits from varying α within the limits allowed by the data.

The accuracy of the reconstruction is verified by the remarkably good fits to the subsequently measured, and much deeper than at the time, Infrared Array Camera (IRAC) counts (Ashby *et al.*, 2013, 2015) and Fig. 2.

C. Reionization limitations on first stars era

At recombination ($z_{\rm rec} \sim 1100$) photons and baryons decouple and the Dark Ages begin lasting until the unknown redshift (s) when the first luminous sources formed, reionizing the Universe. Two opposite regimes govern the later evolution: even a small amount of H I in the IGM would absorb any light emitted in rest UV bands by resonant absorption in the Lyman lines of 0.1216, 0.1026, and 0.09725 μm (Ly-α, β, γ, respectively) with the largest cross section being due to Ly-α (Gunn and Peterson, 1965). Conversely, the ionized IGM affects the CMB in several ways, mainly (1) the CMB angular power spectrum would be suppressed by Thomson scattering on subdegree scales, (2) the Thomson scattering of CMB photons would also lead to linear polarization of the CMB (Rees, 1968), and (3) peculiar motions generate new

temperature aniosotropies (see Sec. IV.D.5). The probability of scattering is $\propto 1 - \exp(-\tau_e)$ with τ_e being the Thomson optical depth and, since the CMB angular structure is measured to have a clear peak structure at $\ell \gtrsim 100$, it follows that $\tau_e \ll 1$. The induced CMB polarization is fixed by the quadrupole anisotropy of the scattering IGM, so polarization on scales exceeding the horizon at $z_{\rm rec}$ (or $\sim 1°$) provides evidence of Thomson scattering or $\tau_e > 0$.

Thus reionization encodes information about the nature of the first stars, first galaxies, and the emergence of a large-scale structure (Mesinger, 2016). An overview of the underlying physics and measurements was provided in Zaroubi (2013).

1. Gunn-Peterson absorption and neutral hydrogen at low z

As pointed out by Gunn and Peterson (1965) (GP), the high value of the Ly-α cross section $\sigma_\alpha = 4.88 \times 10^{-18}$ cm^2 (ignoring line-broadening effects) leads to a very high optical depth:

$$\tau_\alpha^{\rm GP}(z) = 1.2 \times 10^4 \int_0^z \frac{x_{\rm HI}(z')(1+z')^2}{\sqrt{\Omega_{\rm m}(1+z')^3 + \Omega_\Lambda}} dz', \quad (5)$$

where we adopted a He mass fraction of $Y = 0.24$. This results in full absorption even for a very small fraction of the cosmologically distributed neutral hydrogen $x_{\rm HI}$.

The observed absence of the H I trough in quasar spectra at wavelengths shorter than the rest Ly-α line shows that by $z \simeq 6$ the intergalactic hydrogen has been reionized [see the review by Becker, Bolton, and Lidz (2015), and references therein]. Very broadly, Eq. (5) and the observed lack of absorption of quasar spectra require $x_{\rm HI} \lesssim 10^{-4}(1+z)^{-3/2}$ out to $z \lesssim 6$. Prior to that sources of UV radiation had to exist to ionize the surrounding gas. Similar limits on $x_{\rm HI}$ have been reached with probing the Ly damping of gamma ray bursts (Totani *et al.*, 2006).

Numerous observations suggest that reionization of hydrogen was complete by $z_{\rm ion,H} = 6^{+0.3}_{-0.5}$ as summarized by Fan, Carilli, and Keating (2006). Follow-up high resolution spectroscopy of the Sloan Digital Sky Survey (SDSS)-discovered quasistellar objects (QSOs) at $z \sim 6$ established that the Universe contained large amounts of neutral IGM at $z > z_{\rm ion,H}$ as shown in Fig. 7 (Fan *et al.*, 2006). The lower panel shows the reconstructed effective GP optical depth which is $\tau_{\rm GP} \simeq (1+z)^{4.3}$ out to $z \simeq 5.5$ rising exponentially at higher z. Bernardi *et al.* (2003) found that the effective optical depth decreases suddenly after $z \sim 2.4$ by about 10% and climbs back to the smooth scaling again by $z \sim 2.9$.

These observations do not constrain when the hydrogen reionization began or how it proceeded. Bolton and Haehnelt (2007) argued for an extended reionization period. Bolton and Haehnelt (2013) showed with simulations that observations may not require a large change in $x_{\rm HI}$ between $z \simeq 6$ and 7, but "may instead be indicative of the rapid decrease in the typical mean free path for ionizing photons expected during the final stages of reionization" from "the increasing incidence of absorption systems which are optically thick to Lyman continuum photons." More recent observations start to probe the $z \simeq 6$–7 range. Ota *et al.* (2017) found that comparison of models of Lyman-α emitters with the measured Lyman-α luminosity function suggested that the neutral fraction of H increased with redshift at $z > 6$. These observations are
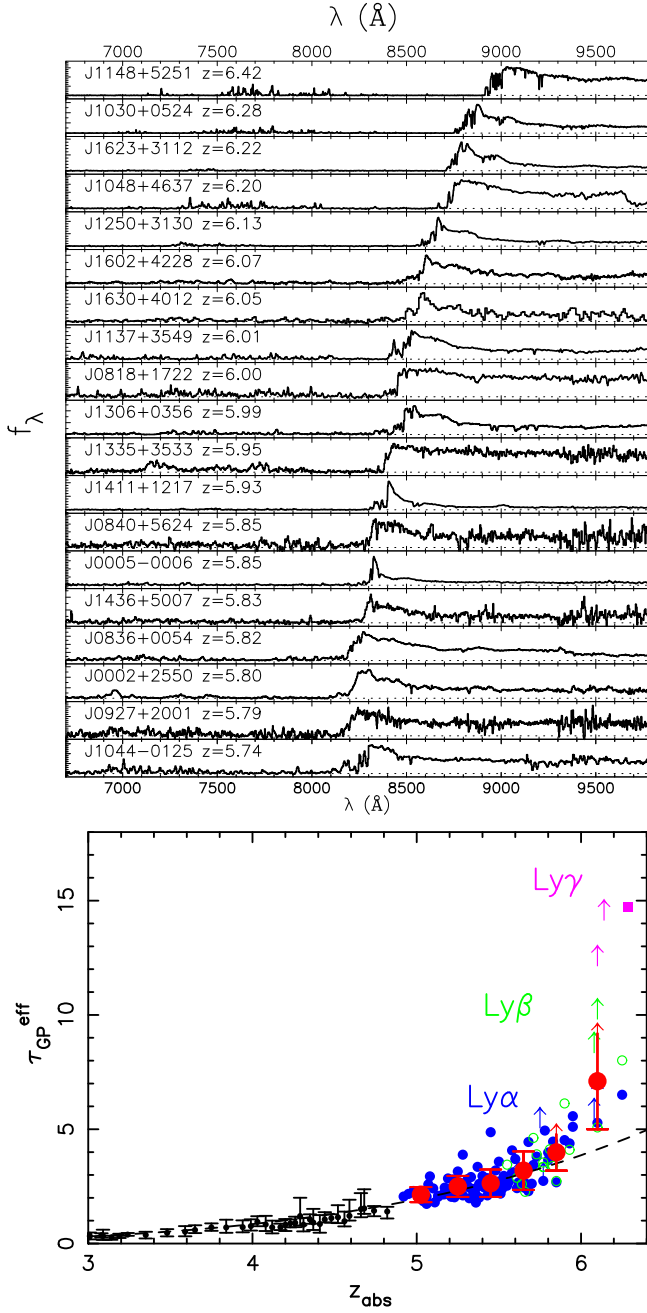
FIG. 7. Top: Spectra of 19 SDSS quasars showing GP absorption. See also Bañados *et al.* (2016) for a more recent extensive compilation. Bottom: Evolution of optical depth combined with the Ly-α, β, and γ absorption measurements. Adapted from Fan *et al.*, 2006.

compatible with both fast (steep) and extended reionization histories as described next.

2. Thomson optical depth and high-z ionization

Detailed transition modeling from a neutral to an ionized state of the IGM hydrogen is the subject of intense current theoretical and observational investigations with the main observational constraints coming from CMB temperature anisotropies. CMB photons are scattered off free electrons, damping the primary anisotropies and generating a large-scale

polarization signal (Mukhanov, 2005) and secondary anisotropies (Vishniac, 1987; Atrio-Barandela and Doroshkevich, 1994). These effects are determined by the Thomson scattering (cross section $\sigma_{\rm T} = 6.65 \times 10^{-25}$ cm^2) optical depth given by

$$\tau_e(0, z_{\rm reion}) = 2 \times 10^{-3} \int_0^{z_{\rm reion}} \frac{x_e(z)(1+z)^2}{\sqrt{\Omega_{\rm m}(1+z)^3 + \Omega_\Lambda}} dz$$

$$\equiv 0.038 + \Delta\tau_e(z > 6), \tag{6}$$

where x_e is the fraction of free electrons at each redshift z. In Eq. (6), the integration gives the total optical depth. A small fraction of cold gas exists in the form of galaxies and Ly-α systems that could be as large as 10% (Salvador-Solé *et al.*, 2017). Removing the contribution $\tau_e(0, 6) \simeq 0.038$ at $z \leq 6$, as evidenced by the GP absorption probes, leaves

$$\Delta\tau_e(z > 6) \simeq 0.003 \Omega_{\rm m}^{-1/2} \int_{z=6}^{z_{\rm reion}} x_e(z)\sqrt{z}\,dz \tag{7}$$

as the high-z contribution to the net Thomson optical depth, which is constrainable by CMB and is of relevance here. It gives a weighted measure of the fraction of free electrons $\langle x_e(z > 6) \rangle$ since the start of reionization at the unknown redshift $z_{\rm reion}$ until the epoch when the GP absorption is known to vanish $z \simeq 6$. These epochs contain the first stars era.

After reionization a fraction $1 - \exp[-\tau(0, z_{\rm reion})] \simeq 0.038 + \Delta\tau$ of CMB photons is scattered off, so their contribution to the primary CMB fluctuations gets smeared out up to the reionization horizon scale $\ell_{\rm reion} \simeq \pi z_{\rm reion}^{1/2} \Omega_{\rm m}^{0.09}$. Because of the damping of the primary CMB radiation power spectrum C_ℓ, CMB temperature-temperature (TT) anisotropies constrain the amplitude of the matter power spectrum as $A_S \exp[-2\tau(0, z_{\rm reion})]$ and, in combination with gravitational lensing measurements that are sensitive to A_S, this can be used to place useful constraints on $\tau(0, z_{\rm reion})$ (Hu, 2001; Ade *et al.*, 2016).

The large-scale E-mode polarization of the CMB is a sensitive probe of reionization (Reichardt, 2016). Compton scattering produces polarization only when the incident field has a quadrupole moment (Rees, 1968; Hu and White, 1997). While photons and baryons are tightly coupled, only the dipole anisotropy is present. Thomson scattering generates polarization causally from the quadrupole component of the underlying ionized matter distribution only up to the horizon scale at the time. E polarization is generated only during recombination and reionization and so it reflects the horizon scale at reionization. Any such signal on superdegree scales directly indicates the epoch when reionization started. The amplitude of the polarization anisotropy is proportional to the duration of recombination and reionization and is maximal at the scale of the horizon (Mukhanov, 2005) which corresponds to $\ell \sim 100$ and $\ell \sim 10$, respectively. The angular scale and width of the reionization contribution to the E mode of CMB polarization power spectrum encodes information about the reionization history. At $\ell < 10$ the amplitude of the E-mode polarization power spectrum is 2 orders of magnitude smaller than the temperature anisotropy power spectrum; the measurement requires not only detector sensitivity to those low signals, but control of systematic errors and foreground

TABLE II. Thomson scattering optical depth from WMAP and Planck analyses.

Data	τ_e	Reference
WMAP 1 yr	0.17 ± 0.04	Kogut *et al.* (2003)
WMAP 3 yr	0.10 ± 0.03	Page *et al.* (2007)
WMAP 9 yr	0.089 ± 0.014	Hinshaw *et al.* (2013)
Planck 2013	0.089 ± 0.014	Ade *et al.* (2014)
Planck 2015	0.075 ± 0.013	Ade *et al.* (2016)
TT + lensing + BAO	0.067 ± 0.016	Ade *et al.* (2016)
Planck 2016	0.058 ± 0.012	Planck Collaboration *et al.* (2016a)

residuals down to those levels (Planck Collaboration *et al.*, 2016a).

In Table II we list the values measured over time. The large discrepancies and the constant decline of the central value reflect the difficulty of the measurement. The WMAP 1 yr value was obtained from the temperature E mode of the polarization cross power. The quoted value of the WMAP 3 yr data was based on the E mode of polarization; subsequent WMAP data releases reduced the error bar. The 2013 Planck results used the Planck based power spectra and WMAP polarization data and derived the same result as the final WMAP 9 yr data analysis. In Planck 2015, foreground cleaning using Planck 33 and 353 GHz maps further reduced the value of τ. Adding CMB lensing data, the optical depth decreased to $\tau = 0.066 \pm 0.016$ consistent with the PlanckTT + lensing + BAO result that uses no low-ℓ polarization data. However, since Planck measured a lensing power spectrum larger than the amplitude expected from the ΛCDM model with Planck measured parameters, lensing data tend to prefer lower values of τ. The Planck 2016 result includes Planck temperature and High Frequency Instrument polarization data. These measurements, although derived assuming reionization in a steplike transition, have important implications for the physical processes driving the reionization of the IGM (Greig and Mesinger, 2017; Mitra, Choudhury, and Ferrara, 2018). The high value measured by WMAP 1 yr supported models of early, $z \approx 15$ reionization (Choudhury and Ferrara, 2006) which is driven by metal-free Pop III stars. The decreasing values of τ measured from subsequent observations reduced the need for high-z galaxies as reionization sources (Bouwens *et al.*, 2015; Mitra, Choudhury, and Ferrara, 2015; Robertson *et al.*, 2015). A steep reionization favors models where quasar contributions were negligible at $z \geq 6$ and the earlier reionization was driven by early galaxies. Alternative sources such as dark matter annihilation and decay have also been considered (Liu, Slatyer, and Zavala, 2016).

For a steep reionization the most recent value of Table II implies that the average redshift at which reionization occurred was between $z = 7.8$ and 8.8 and lasted $\Delta z < 2.8$. The Planck Collaboration used the reionization fraction $x_e(z) = (f/2)[1 + \tanh[(u(z_H) - u(z))/\Delta u]$, with $u(z) = (1 + z)^{3/2}$, $\Delta u = (3/2)(1 + z)^{1/2}\Delta z_H$, and $\Delta z_H = 0.5$ (Lewis, 2008) and fit the redshift when half the H has been ionized z_H to the measured value of τ. But the width and location of the polarization peak contains more information than the overall Thomson optical depth. Allowing arbitrary ionization histories shows a preference in the data for more
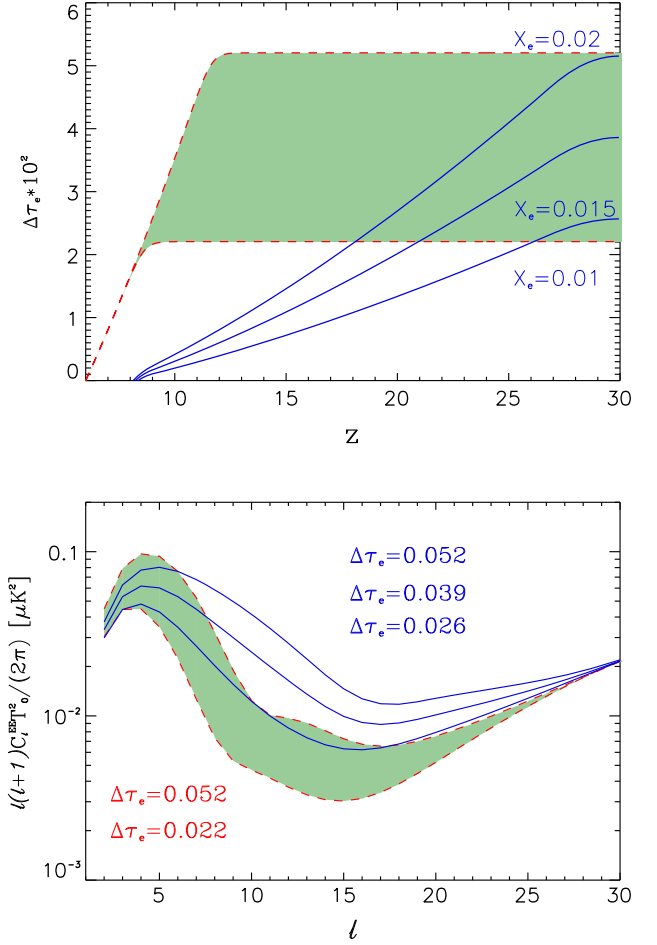

FIG. 8. Top: $\Delta \tau_e$ from $z = 6$ to start of reionization at $z_{\mathrm{reion}} = 30$. The shaded area corresponds to a z-symmetric tanh transition of width $\Delta z_H = 0.5$. Dashed lines bound τ_e for $x_e = 1$ at $z_{0.5} = 8.5$ and 11.5 corresponding to lower and upper limits on net τ_e of Planck Collaboration *et al.* (2016a). The solid blue lines correspond to ionization histories with x_e growing linearly from z_{reion} to $z = 27$ until $x_e = 0.01, 0.015, 0.02$, then remain constant to $z = 9$, and then again grow linearly until $z = 6$ to $x_e = 1$. The contribution to the optical depth from redshifts $z \leq 6$ is taken to be $\tau_e(z < 6) = 0.038$ per Eq. (6). Bottom: Power spectra of the E-polarization anisotropies. The shaded area bounded by the dashed red lines corresponds to the symmetric hyperbolic tangent and the solid blue lines to the constant x_e from $z = 9$ to 27 in the top panel. T_0 is the CMB temperature.

extended reionization processes out to $z \sim 30$ (Heinrich, Miranda, and Hu, 2017). Heinrich, Miranda, and Hu (2017) considered a fiducial model with a constant ionization $x_e = 0.15$ in the range $6 \leq z \leq 30$ although the exact value fluctuates around this fiducial model to fit the C_ℓ^{EE} data. The excess of power in the E mode of polarization in the multipole range $10 \leq \ell \leq 20$, present in Planck 2015 Low Frequency Instrument (LFI) data, is compatible with $\sim 20\%$ of the volume of the Universe being ionized by $z \sim 20$ (Miranda *et al.*, 2017).

In Fig. 8 we plot the contribution to the Thomson optical depth for the two ionization histories as a function of redshift $\tau(0, z)$. When computing the fraction of free electrons, it is necessary to take into account the contribution from He. Its first ionization happens in parallel to that of H but its second

ionization, requiring 54 eV photons, is assumed to have been delayed until quasars that can emit the necessary energetic photons are sufficiently abundant at $z \sim 3$–4 (Madau and Meiksin, 1994; Miralda-Escudé, Haehnelt, and Rees, 2000; Becker *et al.*, 2011). Then we take $f = 1 + f_{\mathrm{He}}$ for singly ionized He and $f = 1 + 2f_{\mathrm{He}}$ for doubly ionized He. We model the He reionization by a tanh function centered at $z_{\mathrm{He}} = 3.5$ and width $\Delta z_{\mathrm{He}} = 0.5$. Since the GP test shows the Universe is ionized by $z \simeq 6$, the total contribution of the IGM to the Thomson optical depth up to $z = 6$ is $\tau(0, 6) = 0.038$. A small fraction of cold gas exists in the form of galaxies and Ly-α systems that could be as large as 10% (Salvador-Solé *et al.*, 2017). Removing this contribution yields a conservative lower bound on the CMB optical depth of $\tau(0, 6) \simeq 0.035$. In Fig. 8 the dashed (blue) and dot-dashed (red) lines correspond to the tanh model with Planck 2015 and Planck LFI 2016 CMB optical depth values while the solid (black) line corresponds to the extended reionization model. The contribution to the optical depth at $z \leq 6$ is $\tau = 0.038$, common to all models. However, when fitting Planck 2016 LFI data, the extended model allows for a much higher contribution from high-z sources since $\Delta \tau \simeq 0.045$ while this contribution is only $\Delta \tau \simeq 0.02$ for the tanh model. Note that the peak of the polarization power spectra of the symmetric hyperbolic tangent reionization model is narrower than the extended reionization model.

D. New high-z populations and their consequences

Here we discuss the various high-z candidates that contribute to CIB and the environments in which they form and subsequently influence. These sources leave potentially detectable signatures of their redshifts through the Lyman break that should truncate their UV emission. The CIB that they leave behind is subject to reionization constraints discussed in Sec. IV.C. For more detailed information regarding emissions from the individual sources possible at high z the interested reader is referred to reviews by Ferrara (2012), Bromm (2013b), and Latif and Ferrara (2016).

1. First halo collapse

Given the underlying matter power spectrum, the number density of available halos can be computed via the Press-Schecter formalism (Press and Schechter, 1974), assuming that any region that reached density contrast $\delta_{\mathrm{col}} = 1.68$ undergoes spherical collapse. The emergence of the first luminous sources at the end of the cosmic dark ages is largely governed by the ability of primordial gas to cool inside these halos (Bromm, 2013a). In the absence of any metal coolants, prior to the dispersal of the first heavy elements from Pop III supernovae, there are two principal cooling channels in the early Universe. At temperatures in excess of $\sim 10^4$ K, line radiation from atomic hydrogen, predominantly concentrated in the Ly-α transition, provides very strong cooling. For the ΛCDM power spectrum, the first DM halos are characterized by shallow gravitational potential wells, with correspondingly low virial temperatures T_{vir}.

Halos with $T_{\mathrm{vir}} \lesssim 10^4$ K will thus not be able to activate atomic hydrogen cooling. In such low-T_{vir} systems, the so-called minihalos, cooling has to rely on molecular

hydrogen. The H_2 formation chemistry in the absence of dust grains is catalyzed by free electrons left over from the epoch of recombination, with a rate that depends on the gas temperature $H + e^- \rightarrow H^- + \gamma$ followed by $H^- + H \rightarrow H_2 + e^-$ (Yoneyama, 1972). [At higher densities three-body reactions become important, $3H \rightarrow H_2 + H$ and $2H + H_2 \rightarrow 2H_2$ (Palla, Salpeter, and Stahler, 1983).] For sufficient H_2 production, temperatures of $\sim 10^3$ K are required. This effect selects DM halos with $T_{\mathrm{vir}} \sim 10^3$ K, minihalos, as the formation sites for the first (Pop III) stars. Molecular hydrogen, however, is fragile and can easily be destroyed by nonionizing soft-UV photons in the Lyman-Werner (LW) (11.2–13.6 eV) bands. Such a pervasive LW background is expected to rapidly emerge in the aftermath of the initial Pop III star formation. It has therefore been argued that the first galaxies, defined as systems that can sustain self-regulated star formation, will be hosted by more massive DM halos. Indeed, "atomic cooling halos" with $T_{\mathrm{vir}} \gtrsim 10^4$ K are considered promising candidates for first-galaxy hosts as they would not have to rely on H_2 as a coolant and could instead tap into the much more efficient, and resilient, atomic hydrogen channel. In summary, there are two characteristic scales for DM host halos, expressed in terms of $T_{\mathrm{vir}} \sim 10^3$ K and $\sim 10^4$ K, where the former is predicted to host the first stars, and the latter the first galaxies (Bromm and Yoshida, 2011).

Figure 9 shows the projected density of collapsed halos with parameters suitable for star formation assuming the power spectrum shown in Fig. 1. The horizontal line shows the confusion limit for the James Webb Space Telescope (JWST) type beam assuming confusion intervenes at >0.02 halo/beam (Condon, 1974). There are various possibilities for boosting the small-scale power in the spectrum of underlying matter fluctuations, from modified inflationary and early Universe physics (Clesse and García-Bellido, 2015; Kashlinsky, 2016; Kawasaki *et al.*, 2017) increasing the levels of the CIB from first stars era.

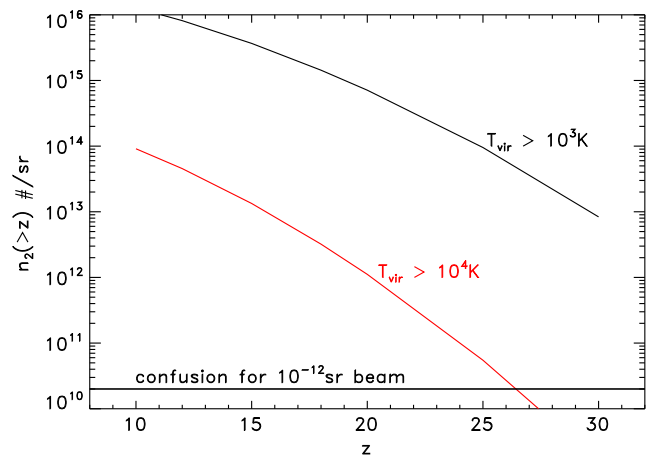FIG. 9. The projected angular density of early luminous halos for $P_{\mathrm{PBH}} = 0$ at redshifts greater than z assuming stars and accreting BHs form when $T_{\mathrm{vir}} \geq 10^3$ K (black) and 10^4 K (red). If PBHs make up the DM, the number would be higher. The horizontal thick solid line shows the confusion limit for a beam of 10^{-12} sr (or 0.04 arcsec^2). Adapted from Kashlinsky, Mather *et al.*, 2015.

2. First stars

Anthropic argument dictates that stars have a typical mass of order solar, i.e., given the values of the fundamental constants a self-gravitating thermonuclear reactor must have mass $M_* \sim M_\odot$. This follows as (1) pressure equilibrium of gas in stars gives their typical temperature $T_* \sim m_p^{4/3} k_B^{-1} G M_*^{2/3} n_p^{1/3}$, where m_p and n_p are proton mass and number density. (2) If all baryons participate in nuclear burning, γ's would have number density similar to protons $n_\gamma \sim n_p$. (3) Stars are optically thick, so photons are at the same thermodynamic temperature. Thus $P_{\text{radiation}} \sim n_\gamma k_B T_* \sim P_{\text{gas}}$. (4) Stars radiate as blackbody $aT_*^4 \sim n k_B T_*$, so $T_* \sim (k_B/a)^{1/3} n^{1/3}$. Combining (1)–(4) leads to

$$M_* \sim M_{\text{Chandra}} = \left(\frac{\hbar c}{G}\right)^{3/2} m_p^{-2} \simeq 1.44 M_\odot.$$

So how do stars reach that mass when collapse starts in much more massive clouds and halos? In his seminal galaxy formation paper Hoyle (1953) proposed the so-called opacity-limited fragmentation theory for the origin of stars. He noted that initially, while the cooling time is much less than the collapse time protostellar clouds collapse isothermally. As a result the Jeans mass in the cloud $M_{\text{Jeans}} \propto T^{3/2} \rho^{-1/2}$ decreases as the density ρ increases during the collapse. The cloud becomes susceptible to fragmentation into progressively smaller clumps. This hierarchical fragmentation stops when density gets high enough to make the fragment opaque and trap the radiation released, via shocks and such, during collapse. For absorption opacity this happens when the optical depth across the fragment reaches $\tau \sim 1$, and the temperature starts rising adiabatically as $T \propto \rho^{2/3}$. The Jeans mass then stops decreasing and the final fragment forms. Hoyle showed that this occurs, for solar metallicity opacities, at a fraction of $M_\odot$, the rest presumably getting accreted after the fragmentation stops.

Prior to enrichment of gas with metals, atomic hydrogen can cool gas only to $T \sim 10^4$ K and H_2, which is hard to form, could lower the temperature a bit as discussed later. Given that the Jeans mass $\propto T^{3/2}$, it was thought early on that first stars would have to be massive. However, Rees (1976) showed very generally that this does not have to be the case: The maximal achievable rate of cooling is the blackbody one, when emission is radiated by the surface of the fragment with radius r at $\simeq aT^4 c(4\pi r^2)$. Collapse ceases being isothermal and fragmentation stops when the cooling is of the order of the free-fall rate of release of binding energy $\simeq (GM^2/r)(G\rho)^{-1/2}$. Combining this with the Jeans criterion for the fragment's mass, $M_F \simeq (\pi k_B T/m_p G)^{3/2} \rho^{-1/2}$ leads to the minimal fragment mass being $M_{F,\text{min}} \simeq M_{\text{Chandra}}(k_B T/m_p c^2)^{-1/4} \propto T^{-0.25}$. Note only the weak dependence on T which arises because while there are no coolants in the absence of metals to keep T low, the same absence of metals makes the onset of $\tau \sim 1$ occur at higher ρ. Thus the absence of metals does not necessarily require high masses for forming stars. The efficiency of fragmentation is also affected by the angular momentum of the collapsing protogalactic clouds (Kashlinsky, 1982).

This assumes that stars formed in efficient fragmentation of collapsing much more massive clouds, a condition that is not necessarily applicable to the first objects forming out of a smooth density field in the metal-free early Universe. Current models suggest that the first, metal-free (Pop III) stars formed at $z < 30$ in dark matter minihalos with virial temperatures $T_{\text{vir}} < 10^4$ K cooling their gas via H_2 line emission. Detailed numerical work (Bromm, Coppi, and Larson, 1999; Abel, Bryan, and Norman, 2002) in the context of the standard ΛCDM model suggested that first stars are likely very massive forming out of high density clumps ($n \sim 10^4$ cm^{-3}) inside the $\sim 10^6 M_\odot$ minihalos [see the review by Bromm and Larson (2004), and references therein].

Once formed, Pop III stars affect their own evolution (feedback) in two ways: (a) by producing copious amounts of LW photons they photodissociate H_2 molecules in nearby objects (Shang, Bryan, and Haiman, 2010; Agarwal *et al.*, 2014; Regan, Johansson, and Wise, 2014; Sugimura, Omukai, and Inoue, 2014), quenching their cooling and star formation; (b) by polluting the star-forming gas with metals dispersed by Pop III SNe, thereby changing the gas fragmentation properties (Schneider *et al.*, 2002, 2006), and inducing a transition to a normal Pop II star formation mode (Tornatore, Ferrara, and Schneider, 2007; Xu, Wise, and Norman, 2013; Pallottini *et al.*, 2014). Numerous evolution modes and stellar activity in the pregalactic Universe have been discussed with varying constituents from quasinormal stellar populations, massive stars, BHs forming in the course of stellar activity, massive binaries, etc. (Kashlinsky and Rees, 1983; Santos, Bromm, and Kamionkowski, 2002; Salvaterra and Ferrara, 2003; Cooray and Yoshida, 2004; Fernandez and Komatsu, 2006; Fernandez *et al.*, 2010, 2012; Mirabel *et al.*, 2011; Helgason *et al.*, 2016).

Massive stars, such as hypothesized to dominate the first stars era, are radiation-pressure dominated and emit nearly at the Eddington limit. In addition, they are close to fully convective with the entire stellar mass taking part in the hydrogen burning (Bromm, Kudritzki, and Loeb, 2001; Schaerer, 2002). This leads to the high radiative efficiency of $\epsilon \sim 0.007$ and a correspondingly more efficient CIB production. For normal Pop II stars, described by a Salpeter initial mass function (IMF), the effective efficiency is an order of magnitude lower since only a small core burns hydrogen.

3. First black holes

For accreting BHs, the radiative efficiency can be as high as $\epsilon = 0.4$ for maximally rotating Kerr holes, reaching values much greater than that of H burning. Thus, BHs can contribute significantly even with a much smaller fraction than stars. Two types of stand-alone BHs appear relevant to discuss in this context: (a) direct collapse BHs (DCBHs) forming during cosmogonic evolution during the first stars era. These BHs would be very massive, as discussed, but of low abundance. (b) Primordial BHs which may have formed in the very early Universe (Carr, 1975) with much lower masses, comparable to the mass within the cosmological horizon at the time of their formation, but having much greater abundance.

a. DCBHs

The process by which astonishingly massive (BH mass $M_\bullet \approx 10^9 M_\odot$) BHs came into existence within 1 Gyr from the big bang is one of the most puzzling mysteries in cosmic

evolution. The current paradigm stipulates that supermassive BHs (SMBHs) have grown from smaller seeds by gas accretion. This hypothesis, however, faces a number of difficulties. The most striking complication is connected with the short time available for the buildup of SMBHs. Assuming that gas accretion occurs at the Eddington rate, assembling the SMBH mass ($M_\bullet = 2 \times 10^9 M_\odot$) deduced for the most distant quasar ULAS J1120 + 0641 (Mortlock *et al.*, 2011) at redshift $z = 7.085$ (or cosmic age 0.77 Gyr) requires a seed mass $M_\bullet > 400 M_\odot$). Such a value is about 10 times larger than the most recent estimates of the mass of first stars (and, consequently, of their remnant BHs). Serious concerns are also raised by the assumption that accretion occurs at the Eddington rate. The most obvious route to form the early BHs during the first stars era is via the final collapse of sufficiently massive Pop III stars [$M > 30 M_\odot$, with the exception of the narrow pair-instability interval $150 < M/M_\odot < 260$ (Aoki *et al.*, 2014; Woosley and Heger, 2015)]. A number of studies (Alvarez, Wise, and Abel, 2009; Milosavljević *et al.*, 2009; Johnson, Dalla, and Khochfar, 2013; Jeon *et al.*, 2014) have shown, however, that stellar BHs accrete inefficiently, although under some extreme conditions they might grow supercritically if accretion occurs through a slim disk (Alexander and Natarajan, 2014; Madau, Haardt, and Dotti, 2014; Volonteri, Silk, and Dubus, 2015) because they spend most of their lifetime in low-density regions. Thus, they appear unable to rapidly build the observed $z = 7$ SMBH population. A compelling solution is to start with a significantly larger seed mass. The early proposals for the formation of massive BHs directly from the gas phase by Loeb and Rasio (1994) and Eisenstein and Loeb (1995) have now developed into more complete scenarios (Begelman, Volonteri, and Rees, 2006; Regan and Haehnelt, 2009; Petri, Ferrara, and Salvaterra, 2012; Johnson, Dalla, and Khochfar, 2013; Latif *et al.*, 2013; Ferrara *et al.*, 2014; Yue *et al.*, 2014). The direct collapse channel invokes the formation of massive BHs in environments where gas gravitational collapse proceeds at sustained rates ($>0.1 M_\odot$ yr^{-1}). The most promising candidates for these superaccreting environments are dark matter halos with virial temperature (a proxy for mass) $T_{\rm vir} \sim 10^4$ K. In these halos primordial gas cools almost isothermally via collisional excitation of the hydrogen $1s - 2p$ transition followed by a Ly-α photon emission. As the accretion rate is $\propto T_{\rm vir}^{3/2}$, this mechanism guarantees extreme accretion rates ~ 0.1–$1 M_\odot$ yr^{-1}, feeding the central object, a central protostellar gas condensation. For efficient feeding, the accretion flow should remain smooth, i.e., it should not fragment. Fragmentation is in general induced by a softening of the equation of state below the isothermal value $\gamma = 1$, i.e., the gas cools as it gets denser. While Ly-α cooling keeps the gas on the isothermal track, the presence of H_2 molecules, heavy elements, or dust provides extra cooling and induces fragmentation. In primordial gas, one has then to prevent only the formation of H_2. This can be achieved by irradiating the collapsing gas with a sufficiently strong external UV field that photodissociates H_2. Such UV radiation field is likely coming from a nearby star-forming galaxy and/or the general collective background radiation from all galaxies present at earlier redshifts. UV radiation effects on larger halos ($T_{\rm vir} > 10^4$ K) are spectacularly

different (Agarwal *et al.*, 2012; Dijkstra, Ferrara, and Mesinger, 2014; Visbal, Haiman, and Bryan, 2014). If H_2 is photodissociated by a sufficiently strong LW intensity $J > J_{\rm crit}$, the hydrogen Ly-α line emission and other processes sustain an almost isothermal collapse preventing gas fragmentation into stellar subunits. Under these conditions, theoretical works (Bromm and Loeb, 2003; Begelman, Volonteri, and Rees, 2006; Volonteri, Lodato, and Natarajan, 2008; Regan and Haehnelt, 2009; Van Borm *et al.*, 2014) show that the most likely outcome is a rapid (≈ 1 Myr) formation of a $M_\bullet = 10^{4-6} M_\odot$ DCBH. However, this process can occur only as long as the gas is metal free; otherwise, fragmentation and star formation would take place (Ferrara, Haardt, and Salvaterra, 2013). As DCBHs also emit LW radiation, they might stimulate additional DCBH formation (Yue *et al.*, 2017). Finally, x rays from DCBHs preheat the intergalactic medium, before galaxies reionize it. In conclusion, the key requirements of the mechanism are that the collapsing gas (a) can be cooled by Ly-α line emission, (b) is metal free, and (c) is exposed to a UV radiation field. Whether and for how long these conditions can be simultaneously met during cosmic evolution is unknown. In halos meeting conditions (a)–(c) the central gas condensation grows rapidly, turning into a supermassive star. The Kelvin-Helmholtz time scale of these objects is much longer than their accretion time, implying that they grow virtually without emitting light. If during the evolution smooth accretion can be maintained, the supermassive star grows until it finally encounters a general relativity instability. This will induce a rapid, direct collapse into a massive BH, i.e., without passing through a genuine stellar phase. These objects, with masses up to $10^6 M_\odot$, are named DCBHs. If they exist, DCBHs would represent the ancestors of SMBHs and offer the ultimate solution of the problems plaguing the field. For a more thorough review of DCBHs see Latif and Ferrara (2016). Finally, in addition to direct collapse, Begelman and Rees (1978) and Kashlinsky and Rees (1983) pointed out that massive seeds may also form as a result of star-star runaway collisions in young ultradense nuclear star clusters [for modern versions, see, e.g., Portegies-Zwart and McMillan (2002) and Lupi *et al.* (2014)].

b. PBHs

The LIGO discovery of GWs from a pair of BHs of similar and unexpected mass ($\sim 30 M_\odot$) (Abbott *et al.*, 2016e) has rekindled suggestions that DM may be composed entirely or predominantly of PBHs (Bird *et al.*, 2016; Kashlinsky, 2016; Clesse and García-Bellido, 2017). PBHs in the mass range of ~ 10–$100 M_\odot$ appear allowed by the available observational data (Carr, Kühnel, and Sandstad, 2016) and the required abundance would appear in broad agreement with a recently claimed abundance of quiescent black hole x-ray binaries in our Galaxy (Tetarenko *et al.*, 2016) and possibly also with the observations of high-velocity clouds near the Galactic center driven by inactive BHs rapidly plunging into molecular clouds (Takekawa *et al.*, 2017; Yamada *et al.*, 2017). The mass range also is within the cosmological horizon at ~ 0.01–0.1 GeV when various mechanisms for generating PBHs in the early Universe operate (García-Bellido, Linde, and Wands, 1996; Jedamzik, 1997). The strongest constraint against them was

claimed by Mack, Ostriker, and Ricotti (2007), Ricotti (2007), and Ricotti, Ostriker, and Mack (2008) to arise from observations of the lack of distortions of a CMB blackbody spectrum from COBE FIRAS (Mather *et al.*, 1990; Fixsen, 2009), but new recent reanalyses of the accretion efficiency onto PBHs during the prerecombination era found significantly weaker constraints and argued against ruling out PBHs of $\lesssim 100 M_\odot$ as the dominant component of DM (Horowitz, 2016; Ali-Haïmoud and Kamionkowski, 2017; Aloni, Blum, and Flauger, 2017). Numerous other observational tests of this proposal have been suggested (Hawkins, 1993; Brandt, 2016; Muñoz *et al.*, 2016; Schutz and Liu, 2017). If DM is made up of PBHs, the latter would introduce a new Poissonian component to the underlying density field as first pointed out by Meszaros (1974, 1975) prior to the development of an inflationary paradigm. This component would substantially accelerate the collapse of the first halos and potentially make a substantial contribution to the CIB (Kashlinsky, 2016). If PBHs are present, they would also require theoretical modifications in the processes affecting first stars era objects. Gas at sound speed c_s in a halo of velocity dispersion v_d is accreted within the radius $r_{acc} = GM_{PBH}/u^2$ with $u^2 = v_d^2 + c_s^2$. The total accretion mass is

$$M_{acc} = 2(n_{gas}/10^4 \text{ cm}^{-3})(M_{PBH}/30M_\odot)^3(u/1 \text{ km s}^{-1})^{-6}M_\odot.$$

For typical parameters this may be a non-negligible fraction of the minihalo baryons at $\sim M_{acc}/M_{PBH} \times \Omega_{CDM}/\Omega_{bar} \propto M_{PBH}^2 u^{-6}$ up to a few percent, but will not increase the PBH mass dramatically. Radiation from accreting PBHs may inhibit H_2 formation and thus influence adjacent star formation and DCBH collapse and evolution as discussed in Bromm and Loeb (2003), Agarwal *et al.* (2012), and Yue *et al.* (2014). At the same time, the increased fractional ionization of the cosmic gas produced by PBHs increases the primordial H_2 abundance by up to 2 orders of magnitude (Ricotti, Ostriker, and Mack, 2008). The increase of the cosmic Jeans mass due to x-ray heating is negligible for models consistent with the CMB data. Hence, the formation rate of the first galaxies and stars would be enhanced by a population of PBHs. Furthermore, stellar dynamical evolution of a PBH minihalo may play an important cosmogonical role. The PBHs in minihalos will evolve via secular stellar dynamical effects similar to those discussed in Kashlinsky and Rees (1983) and by loss of energy to GW emissions. Stellar evaporation will lead to a core-halo structure with the isothermal core of radius r_c and N_{PBH} PBHs evolving on Gyr time scales $t_{evap} \sim N_{PBH}/\ln N_{PBH} \times r_c/v_d$, at constant binding energy, or $v_d \propto N_{PBH}^{-1/2}$, because evaporating PBHs carry zero energy. Formation of massive BHs may be accelerated here. A fraction of PBHs will become binary when GW emission exceeds their kinetic energy ($\sim v_d^2$) (Bird *et al.*, 2016). The fraction of PBHs that will form binaries before evaporation is (Kashlinsky, 2016)

$$f_{PBH,binary} \sim \frac{N_{PBH}^2}{\ln N_{PBH}} \frac{10^{-8} \text{ pc}^2}{r_c^2} \left(\frac{M_{PBH}}{30 \ M_\odot}\right)^{-2} \left(\frac{v_d}{1 \text{ km s}^{-1}}\right)^{-18/7}.$$

Instead of evaporating the resultant binaries will spiral in to the center due to dynamical friction possibly forming a central large

BH contributing to the massive BH formation in the early Universe.

4. Impact on or from thermal history of the IGM

The IGM is heated by the radiative and, to a smaller extent, mechanical energy deposition by stars, black holes, and possibly dark matter annihilation or decay along cosmic evolution. Heating from these sources occurs primarily in the form of photoionization heating. As photons with energies $h\nu > 13.6$ eV ionize neutral hydrogen atoms, the energy of the photoelectron is gradually thermalized in the gas resulting in a temperature increase. The same process controls the ionization of He atoms, requiring 24.6 and 54.4 eV to produce singly or doubly ionized ions of He. Contributions from heavier elements are negligible due to their low abundances.

Photoionization largely dominates the thermal budget of the IGM. Shock heating of the gas produced by supernova-driven galactic outflows is confined in small volumes (Ciardi, Ferrara, and Abel, 2000; Ciardi and Ferrara, 2005) around galaxies, in the so-called circum-galactic medium extending up to about the virial radius of the galaxy host halo. This conclusion is supported by the low level of intergalactic turbulence measured in the IGM (Rauch, Sargent, and Barlow, 2001; Evoli and Ferrara, 2011). Supernova-heated gas might have marginally ($< 10\%$) contributed to reionization by the upscattering of CMB photons inside hot bubbles (Oh, 2001; Johnson and Khochfar, 2011). Additional heating to the IGM can be provided by cosmic rays (Sazonov and Sunyaev, 2015). However, both the production and diffusion of these energetic particles is quite uncertain in the epoch of reionization (EoR).

For this reason, the thermal history of the IGM is intimately connected to the process of cosmic reionization. As ionized (H II) regions grow around the sources and merge, progressively filling the intergalactic space, the gas within them is heated to a temperature typical of ionized regions, i.e., in the range $(1 - 30) \times 10^4$ K. The characteristic volume of these "bubbles" is given by the classical Strömgren formula $V_I = \dot{N}_\gamma/\alpha_B \bar{n}_e^2$, where $\dot{N}_\gamma$ is the source ionizing photon rate, $\alpha_B = 2.6 \times 10^{-13} T_4^{-1/2}$ is the case B recombination rate of hydrogen, and $\bar{n}_e(z)$ is the mean IGM electron density at the relevant redshift. If the sources have hard spectra, containing significant amounts of helium ionizing radiation, analogous He I and H II spheres (typically embedded in the H one) will be produced. These bubbles form the typical "patchy" structure characterizing the reionization process, in which H I is progressively destroyed.

Outside H II regions the IGM remains largely neutral. However, if some x-ray emitting sources such as accreting BHs, high-mass x-ray binaries, annihilating or decaying dark matter, or hot emitting plasma do exist, the IGM can be heated well outside H II regions. This is possible because the comoving mean free path λ_X of an x-ray photon of energy E_X is $\approx (E_X/13.6 \text{ eV})^{2.6}$ times longer than that of UV photons

$$\lambda_X = 20\bar{x}_{HI}^{-1} \left(\frac{E_X}{0.3 \text{ keV}}\right)^{2.6} \left(\frac{1+z}{10}\right)^{-2} \text{ Mpc}, \quad (8)$$

where $\bar{x}_{HI}$ is the IGM mean neutral fraction. Such a long mean free path reduces the patchiness of the ionized gas and results in a more uniform ionization field.

In addition, x-ray ionization is often incomplete, with $\bar{x}_{\mathrm{HI}} \approx 10\%–30\%$, as when $\bar{x}_{\mathrm{HI}}$ exceeds a few percent, most of the photon energy is deposited by secondary electrons (Shull and van Steenberg, 1985; Valdés and Ferrara, 2008) in the form of heat. The x-ray illumination therefore produces extended patches of mostly neutral gas heated to temperatures of ≈ 1000 K in which much smaller H II regions are embedded.

The temperature evolution of the neutral IGM component is of interest for the H I 21 cm redshifted tomography of the IGM (Mesinger, Ferrara, and Spiegel, 2013). Lacking so far sensitive measurements of such signal (this situation is bound to change with the advent of the Square Kilometer Array), only weak lower bounds to the IGM spin temperature—a good proxy of the kinetic temperature as the two are efficiently coupled by the Wouthuysen-Field effect—can be derived: $T_s > 6$ K at $z = 8.4$ (Greig and Mesinger, 2017); see the review by Furlanetto, Oh, and Briggs (2006). Hence, here we concentrate on the temperature of the ionized gas during the reionization process.

The equation describing the IGM kinetic temperature T at mean density (where temperature measurements are available) is (Theuns *et al.*, 2002)

$$\frac{1}{T}\frac{dT}{dt} = -2H + \frac{1}{\mu}\frac{d\mu}{dt} + \frac{2\mu}{3k_{\mathrm{B}}T}\frac{dQ}{dt}, \qquad (9)$$

where H is the Hubble parameter, k_{B} is Boltzmann's constant, μ is the mean molecular weight, and Q is the effective radiative transfer rate. The latter includes photoelectric heating and cooling via recombination, excitation, inverse Compton scattering, collisional ionization, and bremsstrahlung. The second term on the right-hand side is relatively unimportant, accounting for the change in the number of particles in the thermal bath; it becomes marginally important (a few percent level) only during He II reionization.

Note that in the absence of heating the IGM temperature evolution would follow a purely adiabatic evolution imposed by the Hubble expansion [first term on the right-hand side of Eq. (9)], corresponding to $T \propto (1+z)^2$. Adiabatic expansion remains the dominant cooling mechanism for gas around the cosmic mean $\bar{n} \approx 2.3 \times 10^{-7}$ cm$^{-3}(1+z)^3$; however, at $z > 7$ the contribution of inverse Compton cooling off CMB electrons cannot be neglected.

As Eq. (9) depends on the number of particles, and hence on the ionization state of the gas, its solution requires a derivation of x_e. This is usually done by balancing the ionization rate from all the sources Γ with the recombination rate. For hydrogen, such an equation in equilibrium is simply $n_{\mathrm{HI}}\Gamma = n_e^2 \alpha_{\mathrm{B}}(T)$; similar equations hold for the different ionization stages of He. As the photoionization time scale ($\approx \Gamma^{-1}$) is much shorter than the cooling time scale (H^{-1}), the implicit assumption of ionization equilibrium is well justified.

A general expression for Γ valid for both H and He is

$$\Gamma_i = c \int_{\nu_{\mathrm{T}}^i}^{\infty} d\nu \frac{u_\nu}{h\nu} a_\nu^i, \qquad (10)$$

where a_ν^i is the photoelectric cross section of the species $i = $ H, He, ν_{T}^i is the photoionization threshold frequency of species i, and u_ν is the specific energy density of the UV background. The specific energy density is related to the specific intensity of the radiation by $u_\nu = 4\pi J_\nu / c$.

The most standard approach is to adopt the new (Haardt and Madau, 2012) prescription for the UV background intensity evolution and a spectral shape of the form $J_\nu \propto \nu^{-\alpha}$. The power index depends on the spectra of sources considered (α_s) and the filtering due to radiative transfer effects in the Ly-α forest whose logarithmic slope of the column-density distribution is $\beta = 1.3 \pm 0.2$. Then $\alpha = \alpha_s + 3(\beta - 1)$, with $\alpha_s = 0.5$–1.0 for stellar sources and $\alpha_s = 1.5 \pm 0.2$ for quasars. The considerable uncertainty in α does not represent a major problem as the IGM temperature sensitivity to this parameter is limited by the optically thin conditions prevailing in the IGM. Then the photoheating rate $dQ/dt \propto (2 + \alpha)^{-1}$ varies at most by a factor of 2, corresponding to an even smaller temperature change as $T \approx (dQ/dt)^{0.6}$.

Thus, once the initial temperature of the gas T_i at some fiducial z_i is assigned, the thermal history can be computed straightforwardly. Most models take z_i as the redshift of reionization, thus postulating that reionization is instantaneous. While this is known not to be the case, such assumption is justified if Eq. (9) is thought to describe the evolution of a Lagrangian fluid element that has been engulfed by an expanding H II region at z_i.

The outcomes of such models are used to interpret the temperature measurements obtained from the Ly-α forest data in quasar absorption line experiments. These measurements became available around the beginning of this century (Ricotti, Gnedin, and Shull, 2000; Schaye *et al.*, 2000; McDonald *et al.*, 2003). Although uncertain, such measurements allowed one to conclude that the IGM temperature at the mean density T_0 at $z \approx 3$ was too high to be consistent with the heat input produced by hydrogen reionization alone. The most popular solution to this problem involved extra heating due to He II reionization occurring around $z = 3$ (Hui and Haiman, 2003), an idea also supported by the tentative (and debated) detection of a bump in the T_0 evolution located at that epoch.

The situation has become now clearer with the renewed interest in the IGM thermal history with the new observations by Becker *et al.* (2011) [see also Rudie, Steidel, and Pettini (2012)]. The key advance has been to move away from the uncertain determination of T at $\rho = \bar{\rho}$, and measure it at a critical density ρ_* at which the Ly-α Gunn-Peterson optical depth $\tau \approx 1$. In this regime, the Ly-α forest lines are most sensitive to temperature. The difficulty is that to transform $T_* \equiv T(\rho_*)$ into the usually quoted T_0 one needs to know the adiabatic index γ entering the equation of state $T(\rho) = T_0(\rho/\bar{\rho})^{\gamma-1}$. These data, complemented by more recent ones by Boera *et al.* (2014), have allowed one to put together a high-quality sample extending in the range $1.6 < z < 4.8$. The new data confirm the peak at $z \approx 3.1$, where $T_0 \simeq 2 \times 10^4$ K. Such a feature is most straightforwardly interpreted with the extra heating provided by He II reionization, although models involving intergalactic absorption of TeV blazars (Broderick, Chang, and Pfrommer, 2012; Puchwein *et al.*, 2012) or heating from cosmic rays (Lacki, 2015) have been suggested as

alternative explanations. Note that in the absence of He II reionization heating, hydrogen reionization would have left the IGM at a much lower temperature ($\approx$5000 K) at $z = 3$.

These data can also constrain the temperature of the IGM in the EoR (Furlanetto and Oh, 2009; Bolton *et al.*, 2012; Lidz and Malloy, 2014). The models must be anchored to the highest z (Becker *et al.*, 2011) data points, which imply that at $z = 4.8$ the IGM temperature was $(6.5 \pm 1.5) \times 10^3$ K. Then one varies the value of z_i and T_i and selects models that predict values within the error bars. As already mentioned, the UV background spectral index variation has only minor effects on the thermal evolution. One can also explore slightly more sophisticated models in which different parcels of gas are heated at different temperature in a given reionization redshift span $(\Delta z_i, \Delta T_i)$ and then average over the results. Additional models (Bolton *et al.*, 2014) calibrate their predictions on numerical simulations to derive the evolution of γ.

In brief, due to the rapid cooling imposed by adiabatic expansion which forces the temperature to set onto an asymptotic value, a large degeneracy exists among many reionization models with different $\Delta z_i, \Delta T_i$. However, some extreme models in which hydrogen reionization is either (i) very short $\Delta z_i \leq 3$ and ends at $z = 6$, or (ii) produces too high ($> 25\,000$ K) temperatures in the ionized gas are excluded as the gas cannot timely cool to the measured temperatures at $z = 4.8$. It appears that the temperature value which is consistent with the largest number of thermal histories, also including those in which reionization can start earlier than $z = 9$, is $T = 2 \times 10^4$ K.

5. Sunyaev-Zeldovich contributions and imprints

Free electrons in the IGM resulting from reionization produce CMB temperature anisotropies via the Sunyaev-Zeldovich (SZ) effect. The two main contributions to this effect are the anisotropies produced by the thermal motion of electrons, known as thermal SZ (TSZ) (Sunyaev and Zeldovich, 1972) and those produced by their peculiar motion, termed kinematic SZ (KSZ) (Sunyaev and Zeldovich, 1980). The CMB temperature anisotropies generated by the ionized gas in the direction $\hat{n}$ are

$$\frac{\Delta T_{\mathrm{SZ}}(\hat{n})}{T_{\mathrm{CMB}}} = \int \left[G(x) \frac{k_B T_e}{m_e c^2} - \frac{\vec{v}_e \cdot \hat{n}}{c} \right] \frac{d\tau_e}{dz} dz, \quad (11)$$

where m_e, T_e, and $\vec{v}_e$ are the electron mass, temperature, and peculiar velocity. The TSZ has a characteristic frequency dependence $G(x) = x \coth(x/2) - 4$ with $x = h\nu/k_B T_{\mathrm{CMB}}$; ignoring relativistic corrections $G(x) \simeq -2$ below $\sim$217 GHz vanishes at 217 GHz and goes positive at higher ν.

At the physical conditions expected to hold during reionization, the temperature would be $T_e \leq 10^4$ K and the KSZ effect would be about 3 orders of magnitude larger than the TSZ contribution. Nevertheless, the TSZ effect offers a direct probe to the physical conditions of the ionized gas. Cross correlation of CMB temperature anisotropies with CIB fluctuations could provide a direct measurement of the temperature of the IGM during reionization (Atrio-Barandela and Kashlinsky, 2014): the subdominant TSZ component can be isolated in the presence of multifrequency CMB maps, when

frequency differencing removes the primary CMB and any KSZ components. The potentially measurable TSZ component carries information on the condition of the IGM at the pre-reionization epochs being proportional to the product of τ_e and T_e integrated along the line of sight.

In the KSZ effect we can distinguish "homogeneous" linear (Vishniac, 1987) and nonlinear (Hu, 2000) contributions due to the peculiar motion of baryons in a completely ionized IGM and the patchy anisotropies generated by peculiar motions when the ionization fraction varies in space (Aghanim *et al.*, 1996; Gruzinov and Hu, 1998; Knox, Scoccimarro, and Dodelson, 1998; Mesinger, McQuinn, and Spergel, 2012). As the first stars and BHs start producing UV photons, they generate ionization spheres around them. Before those spheres merge, the Universe would be ionized in patches generating KSZ anisotropies of $\Delta T/T_{\mathrm{CMB}} \sim \tau_e(v_{\mathrm{rms}}/c)\theta(1 + z_{\mathrm{reion}})^{3/4}(\Delta z_{\mathrm{reion}})^{1/2}$, where v_{rms} is the rms peculiar velocity, θ is the angular scale subtended by the ionized patches, and $\Delta z_{\mathrm{reion}}$ is the redshift duration of the patchy phase. Thus, the patchy component can be used to set an upper limit on the duration of reionization (Zahn *et al.*, 2012). Munshi *et al.* (2016) discussed how to separate it from the homogeneous contribution.

Numerical radiation-hydrodynamical simulations estimate an amplitude $[\ell(\ell+1)C_\ell^{\mathrm{KSZ}}/2\pi]|_{\ell=3000} \sim 0.6$–2.8 μK^2 at $\ell = 3000$ (Battaglia *et al.*, 2013). Data from Planck, Atacama Cosmology Telescope (ACT), and South Pole Telescope— Sunyaev-Zel'dovich (SPT-SZ) provide consistent constraints. George *et al.* (2015) found $[\ell(\ell+1)C_\ell^{\mathrm{KSZ}}/2\pi]|_{\ell=3000} < 3.3$ μK^2 at the 95% confidence level and translated this upper limit into a constraint on the duration of the period when the electron fraction grows from 20% to 99% of $\Delta z < 5.4$ also at the 95% confidence level. Lower ionization fractions are largely made up of ionized regions too small to be probed by the SPT data (George *et al.*, 2015). Furthermore, if star formation is suppressed in low-mass dwarf galaxies and minihalos located in ionized or LW-dissociated halos, then more extended reionization histories are compatible with upper limits on the KSZ power spectrum (Park and Ricotti, 2013). A similar constrain was derived from the UV luminosity functions of star-forming galaxies at $z \sim 6$–10. Ishigaki *et al.* (2018) concluded that the redshift interval where the ionization fraction grows from 0.1 to 0.99 was $\Delta z = 4.1 \pm 1.7$.

6. Sub-mm first dust emission

Dust grains are a fundamental constituent of the interstellar medium (ISM) of galaxies. A large fraction ($\approx$50% in the Milky Way) of the heavy elements produced by nucleosynthetic processes in stellar interiors can be locked into these solid particles. Most relevant here, they efficiently absorb optical or ultraviolet stellar light, by which they are heated and reemit this energy as longer [far-infrared (FIR) or sub-mm] wavelength radiation that can freely escape from the galaxy. It is then natural to expect a tight relation between the UV "deficit" and the IR excess produced by this process.

The presence of dust at high ($z \gtrsim 6$) redshift implies that conventional dust sources (asymptotic giant branch stars and other evolved stars) are not the dominant contributors. This is because their evolutionary time scales are close to or exceed

the Hubble time at that epoch ($\approx$1 Gyr). Following the original proposal by Todini and Ferrara (2001), it is now believed that the first cosmic dust was formed in the ejecta of supernovae ending the evolution of much more fast-evolving massive stars (Hirashita and Ferrara, 2002; Bianchi and Schneider, 2007; Nozawa *et al.*, 2007; Gall, Hjorth, and Andersen, 2011). For similar reasons the standard grain growth acting on grains during their residence time in molecular clouds of contemporary galaxies cannot increase the amount of dust by considerable amounts (Ferrara, Viti, and Ceccarelli, 2016). Thus, albeit quasar host galaxies show remarkably high dust masses (Beelen *et al.*, 2006; Michalowski *et al.*, 2010), in general the dust-to-gas ratio toward high z rapidly decreases (Dunlop, 2013) as also witnessed by the observed steepening of early galaxies UV spectra. This does not come as a complete surprise given that the average metallicity of the Universe increases with time.

Ferrara *et al.* (1999) noticed another important feature of high-z dust [for a recent calculation see da Cunha *et al.* (2013)]. Because of the redshift increase of the CMB temperature $T_{CMB} = 2.725(1 + z)$ K, the FIR signal from dust becomes increasingly swamped by the CMB. At $z = 6$, for example, $T_{CMB} = 19$ K; as usual dust temperatures in the diffuse ISM of galaxies are in the range 20–40 K, and the effect cannot be neglected. Even more dramatic, if not complete, might be the suppression of the signal from dust in dense regions (e.g., molecular clouds) where the dust is in thermal equilibrium with the CMB.

The superb sensitivity of the Atacama Large Millimeter-Submillimeter Array (ALMA) interferometry has allowed detection of the FIR signal of a handful of Lyman break galaxies (LBGs) for which HST rest-frame UV photometry (and hence the UV slope $\propto \lambda^\beta$ determination) by Capak *et al.* (2015), reporting a puzzling deviation of detected LBGs from the more local infrared excess (IRX) versus β relation (Meurer, Heckman, and Calzetti, 1999). In practice, these galaxies, although characterized by relatively flat $\beta \approx -1$ values indicative of non-negligible dust attenuation, show a noticeable FIR deficit, i.e., they are relatively "FIR dark."

Such a suggested deficit has been strongly reinforced by an even more recent report by the ALMA Spectroscopic Survey in the Hubble Ultra Deep Field (ASPECS) survey (Bouwens *et al.*, 2016). They performed deep 1.2-mm-continuum observations of the Hubble ultradeep field (HUDF) to probe dust-enshrouded star formation from 330 LBGs spanning the redshift range $z = 2$–10. The striking result is that the expectation from the Meurer *et al.* IRX-β relation at $z = 4$ was to detect at least 35 galaxies. Instead, the experiment provided only six tentative detections (in the most massive galaxies of the sample). Clearly, redshift evolution of either the dust temperature and/or mass must play a key role.

An exception to this scenario is the puzzling case of A1689-zD1 (Watson *et al.*, 2015; Knudsen *et al.*, 2017), a $z = 7.5 \pm 0.2$ gravitationally lensed LBG where the thermal dust emission has been detected by ALMA. The large FIR flux $L_{FIR} = (6.2 \pm 0.8) \times 10^{10} L_\odot$ indicates considerable dust amounts, consistent with a Milky Way dust-to-gas ratio. A similar result has been obtained by Laporte *et al.* (2017) for the $z \approx 8$ Y-band dropout galaxy, A2744 YD4. The ALMA 1 mm detection can be interpreted to arise from dust thermal

emission, with an estimated dust mass of $6 \times 10^6 M_\odot$. How this large dust amount formed so quickly is a challenging question for the future.

Overall, the CIB level produced by the dust components from early times is generally expected to be small (De Rossi and Bromm, 2017) in comparison to the mean CIB detected at these wavelengths (Puget *et al.*, 1996; Fixsen *et al.*, 1998). It is unlikely to be detectable in direct measurements, but with enough dust may be isolated in some suitably constructed cross-correlation studies.

7. Reconstructing emission history via Lyman tomography

It is important also to isolate the CIB production as a function of redshift. Different cosmogonical models predict different modes of evolution at various high z including the range of epochs that cannot be probed even after the advent of the JWST. Kashlinsky, Arendt *et al.* (2015) and Kashlinsky, Mather *et al.* (2015) proposed a methodology to reconstruct CIB contributions by z using the Lyman tomography in the presence of two adjacent, nonoverlapping filters at wavelengths $\lambda_2 > \lambda_1$. The discussion assumes that there are no emissions below some Lyman-cutoff wavelength λ_{Ly}, which corresponds to Ly-α at rest 0.1216 μm when reprocessing is done by the halo H I, or Ly continuum (0.0912 μm) otherwise (Santos, Bromm, and Kamionkowski, 2002). Such a cutoff is fundamentally different from situations such as the Balmer break, where emissions, albeit of different amplitudes, exist on both sides of the wavelength and which gets washed out in the CIB integrations over different z.

The projected CIB autopower is related to the underlying P_{3D} of the sources by the relativistic Limber equation (3). The integration range stops at $z_{Ly}(\lambda)$ because at larger redshifts sources emit only longward of the λ_{Ly}, the integration extending to z specified by the long wavelength edge of the filter band pass. The cross power between two bands $\lambda_2 > \lambda_1$ extends only to $z_{Ly}(\lambda_1)$:

$$\frac{q^2 P_{12}}{2\pi} = \int_0^{z_{Ly}(\lambda_1)} \frac{dF_{\lambda_1'}}{dz} \frac{dF_{\lambda_2'}}{dz} \Delta^2(qd_A^{-1}; z) dz. \quad (12)$$

At $\lambda_2 > \lambda_1$, we can write Eq. (3) as

$$\frac{q^2 P_2(q, < z_{Ly}(\lambda_2))}{2\pi} = \int_{z_{Ly}(\lambda_1)}^{z_{Ly}(\lambda_2)} \left(\frac{dF_{\lambda_2'}}{dz}\right)^2 \Delta^2(qd_A^{-1}; z) dz$$
$$+ \frac{q^2 P_2(q, < z_{Ly}(\lambda_1))}{2\pi}$$
$$= \frac{q^2}{2\pi} \left[P_{\Delta z} + \frac{1}{\mathcal{C}_{12}(< z_{Ly}(\lambda_1))} \frac{P_{12}^2}{P_1} \right]. \quad (13)$$

$P_{\Delta z}$ probes emissions spanning Δz at $z_{Ly}(\lambda_1) < z < z_{Ly}(\lambda_2)$ and arises from populations inaccessible to λ_1, but present at λ_2. Here P_1 and P_2 are autopower spectra at the adjacent bands λ_1 and λ_2 with coherence $\mathcal{C}_{12} = P_{12}^2/P_1 P_2$.

One wants to isolate the power $P_{\Delta z}$ arising from luminous sources between $z_{Ly}(\lambda_1)$ and $z_{Ly}(\lambda_2)$. Rewriting Eq. (13) leads to CIB fluctuation generated over $z_{Ly}(\lambda_1) < z < z_{Ly}(\lambda_2)$ as follows:

$$\frac{q^2 P_{\Delta z}(q)}{2\pi} = \left[\frac{q^2}{2\pi}\left(P_2 - \frac{P_{12}^2}{P_1}\right)\right]_{\text{data}} + \frac{q^2}{2\pi}P_{\text{sys}}, \quad (14)$$

where the first right-hand side term is fully given by the data and the last term is driven by incoherence of the sources at the two adjacent bands that occupy the same span of redshifts $z < z_{\text{Ly}}(\lambda_1)$:

$$\frac{q^2}{2\pi}P_{\text{sys}} = \left[\frac{\mathcal{C}_{12}(q, z < z_{\text{Ly}}(\lambda_1)) - 1}{\mathcal{C}_{12}(q, z < z_{\text{Ly}}(\lambda_1))}\right] \times \left[\frac{q^2}{2\pi}\frac{P_{12}^2}{P_1}\right]_{\text{data}} \leq 0. \quad (15)$$

The subscript "data" refers to directly measurable quantities. $P_{\text{sys}} \leq 0$ because $\mathcal{C} \leq 1$ and the measurable quantity $(P_2 - P_{12}^2/P_1)$ sets a strict upper limit on the CIB fluctuations arising at $z_{\text{Ly}}(\lambda_1) < z < z_{\text{Ly}}(\lambda_2)$.

E. New diffuse sources at intermediate and low z

The possibility of non-negligible CIB fluctuations arising at low to intermediate z from a "missing light" associated with galaxy populations but distributed in diffuse structures around masked sources has been proposed by Cooray *et al.* (2012). This missing light is termed the intrahalo light (IHL) which would permeate the Universe. IHL is to be distinguished from an "intracluster light" (ICL) (Lin and Mohr, 2004; Mihos *et al.*, 2005; Mihos, 2016), associated with clusters of galaxies, which in turn are removed in CIB fluctuations studies; much of the ICL is further linked to extended halos of brightest cluster galaxies. The mean luminosity of an IHL contributing halo of mass M is assumed to be modeled at rest λ as $l_\lambda(M, z) = f_{\text{IHL}}(M)[F_\lambda L_{2.2\mu\text{m}}(M)](1+z)^\alpha$ with F_λ being the SED of the IHL component, normalized to unity at 2.2 μm and assumed to be the same as that of the old red stellar populations of elliptical galaxies. The fraction of the halo light stripped away as the IHL is modeled as $f_{\text{IHL}} = A_f(M/10^{12}M_\odot)^\beta$ and the free parameters (α, β, A_f) are adjusted to fit CIB observations. The parental halo luminosity is normalized per ICL observations of Lin, Mohr, and Stanford (2004) to be $L_{2.2\ \mu\text{m}}(M) = 5.6 \times 10^{12}(M/2.7 \times 10^{14}M_\odot)^{0.7}L_\odot$. The angular power spectrum of the IHL is then calculated from the one-halo term associated with the halo assumed to follow the NFW Navarro, Frenk, and White (1997) profile and a two-halo term reflecting the underlying clustering. The halo number density is derived from the underlying ΛCDM hierarchy via a Sheth and Tormen (2002) variant of the Press-Schechter prescription.

A generic prediction of the IHL model is that the CIB excess there is produced by (1) the same types of populations as in known galaxies that (2) are located at $z \ll 10$ and hence their CIB component is coherent with the diffuse light at visible wavelengths, and (3) have no enhanced BH activity of populations. Because the IHL-producing stellar populations have normal Salpeter-type IMF with emissions dominated by normal stars, to produce the same CIB levels one would need to convert more baryons than from very massive stars radiating close to the maximal efficiency of H burning. Additionally, as discussed by Helgason *et al.* (2014), Sec. 4.3, the light-to-mass ratio of the IHL is calibrated based on intracluster light (at $2.7 \times 10^{14}M_\odot$), and extrapolated as a power law down to much lower mass scales. The bulk of the

IHL is thus associated with low-mass systems so that it requires low-mass systems to host IHL exceeding their own stellar light. This results in IHL comparable to the integrated energy produced by the entire galaxy populations.

A possibility also exists of CIB contributions at low z from a new particle decay (Bond, Carr, and Hogan, 1986; Gong *et al.*, 2016; Kohri and Kodama, 2017).

V. CURRENT MEASUREMENTS AND DATA SETS

While mean levels of CIB are generally overwhelmed by foregrounds, Kashlinsky *et al.* (1996) noted that the same is not true for fluctuations and have pioneered the use of fluctuations to study CIB, applying it to DIRBE (Kashlinsky, Mather, and Odenwald, 1996; Kashlinsky and Odenwald, 2000). The low angular resolution (0.7°) of the DIRBE beam did not allow removal of many sources and restricted the probing of the net CIB fluctuation levels at the DIRBE bands from 1.25 to 240 μm. Further development came with the deep Two-Micron All Sky Survey (2MASS) study of a higher angular resolution, but ground-based instrument, where Kashlinsky *et al.* (2002) and Odenwald *et al.* (2003) developed studies of *source-subtracted* CIB to isolate CIB fluctuations at 1.1, 1.6, and 2.2 μm from galaxies fainter than $m_{AB} \simeq 20$–21. The next significant step was made using the IRAC instrument (Fazio *et al.*, 2004b) onboard Spitzer, where Kashlinsky *et al.* (2005) identified significant source-subtracted CIB fluctuations at 3.6 and 4.5 μm, after subtracting known sources to deeper levels, which exceed the contribution from remaining known galaxies. This signal was confirmed with numerous follow-up studies. An AKARI-based analysis by Matsumoto *et al.* (2011) showed consistency with the IRAC measurements, but also identified significant source-subtracted CIB fluctuations at 2.4 μm. A NICMOS-based study (Thompson *et al.*, 2007a, 2007b) reached well beyond the depth of the 2MASS CIB results, but the shallower CIBER results at 1.1 and 1.6 μm (Zemcov *et al.*, 2014) conflicted with both 2MASS and NICMOS.

The currently available results are discussed later after summarizing the requirements for probing CIB fluctuation component as faint as that expected from early sources. While there is currently overall agreement about the source-subtracted CIB signal identified at 2–5 μm, the various measurements, discussed later, at 1–2 μm led to currently conflicting and mutually exclusive measurements, hence the division of the discussion in this section. Figure 10 shows the wavelength range of the filters employed in the data analyses discussed next.

A. Requirements for probing source-subtracted CIB fluctuations from new populations

CIB science goals are driven by the need to reliably uncover, via CIB fluctuations, populations which cannot be resolved because they are fainter than the confusion limit of the present-day instruments. Arendt *et al.* (2010) discussed in detail the exhaustive search for systematics in the analysis of the deep Spitzer data placing particular emphasis on the map-making algorithms and understanding of the instruments. There are three main requirements, broken down into detail as follows: (I) Maps must be prepared that isolate the
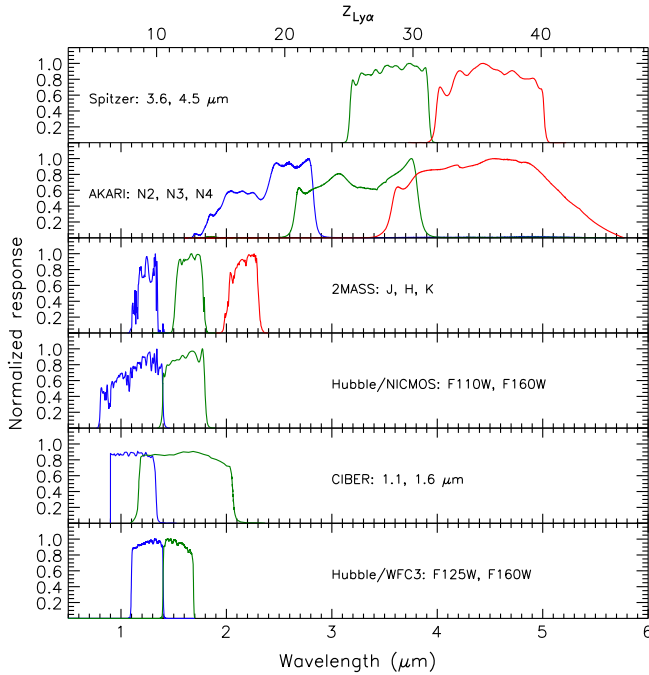
FIG. 10.   Filters used in CIB measurements to date.

source-subtracted CIB fluctuations down to the (faint) levels such as expected from first stars era, (II) tools used to analyze the processed (and clipped) data must properly evaluate random and systematic contributions to large-scale fluctuations, and (III) a robust cosmological interpretation of the results must demonstrate certain characteristics and rule out others.

(I) *Map assembly*: (1) Maps of diffuse emission should be constructed carefully, removing artifacts well below the expected cosmological signal. In practice, this means that the maps should not have any structure at levels above $\delta F \sim 0.01$ nW m^{-2} sr^{-1} at arc min scales at the IRAC wavelengths. (2) No correlations should be introduced when constructing the maps. (3) In constructing the maps, one should avoid spatial filters that may remove the very populations which are in the confusion noise and whose signal is to be identified. (4) Because of temporal variations of the zodiacal light, data should be collected in as short time intervals as possible.

(II) *Analysis tools*: (5) Both the amplitude and the power spectrum of the instrument noise must be estimated from the data (e.g., time-differenced A–B maps). This is particularly necessary for shot-noise estimates. (6) If sources are removed from the images via modeling and subtraction, the source model should accurately account for extended low surface brightness emission, i.e., the low level wings of the point-spread function (PSF) and the intrinsic brightness profile of extended galaxies. The modeling should not be pushed so deep that it alters the random noise distribution of the measurements. (7) The effects on the power spectrum caused by masking sources need to be considered carefully. If the fraction of

removed pixels is small (typically $\lesssim 30\%$) one can apply FTs; otherwise the correlation function must be evaluated to explicitly demonstrate that the power spectra recovered are consistent with the computed correlation functions. (8) The beam must be reconstructed and its large- and small-scale properties understood.

(III) *Interpretation*: (9) A true cosmological signal must be demonstrated to be isotropic on the sky. (10) End-to-end simulations must be done to test that no artifacts mimic the signal found. (11) Foreground contributions must be evaluated: Galactic ISM (cirrus) can be extrapolated from locations and wavelengths where it is brighter, and zodiacal emission can be measured via its temporal changes at different epochs.

B. Measurements at 2–5 μm

First measurements here were motivated by theoretical suggestions of Cooray *et al.* (2004) and Kashlinsky *et al.* (2004) of a measurable CIB fluctuation signal in certain configurations that arises from first stars era. While Cooray *et al.* (2004) proposed a configuration of wide fields with relatively shallow depth, Kashlinsky *et al.* (2004) suggested analyzing deep relatively small regions, where more galaxies can be removed but the angular scales are more limited. Kashlinsky *et al.* (2005) identified the first suitable data set from early Spitzer IRAC observations (Barmby *et al.*, 2004) and laid the ground for future work by establishing the required machinery and identifying for the first time a source-subtracted CIB fluctuation component. This component exceeded that from remaining known ("ordinary") galaxies and was proposed to originate in sources from the first stars era.

1. Spitzer

NASA's Spitzer space telescope is a 0.85 m diameter infrared telescope launched in 2003 on an Earth-trailing orbit (Werner *et al.*, 2004). Its CIB results have been obtained with the IRAC (Fazio *et al.*, 2004b), which covered four channels at 3.6, 4.5, 5.8, and 8 μm when it operated in the cryogenic regime until mid-2009. After its cryogen was exhausted it continued operating in a warm phase at 3.6 and 4.5 μm.

a. Self-calibration and map processing

Self-calibration and map processing were established as described by Arendt *et al.* (2010). A method for self-calibration intended to make optimal use of IR imaging data with minimal (or no) need for separate calibration data was outlined by Fixsen, Moseley, and Arendt (2000). The procedure essentially calculated a least-squares fit between the data and a model of the data. The data model includes parameters describing the astronomical sky (e.g., the intensity at each pixel in an image of the observed field) and various detector parameters (e.g., gain factors and offsets for each pixel of the detector). An example of the use of a more complex data model was provided by Arendt, Fixsen, and Moseley (2002). The self-calibration procedure relies on the
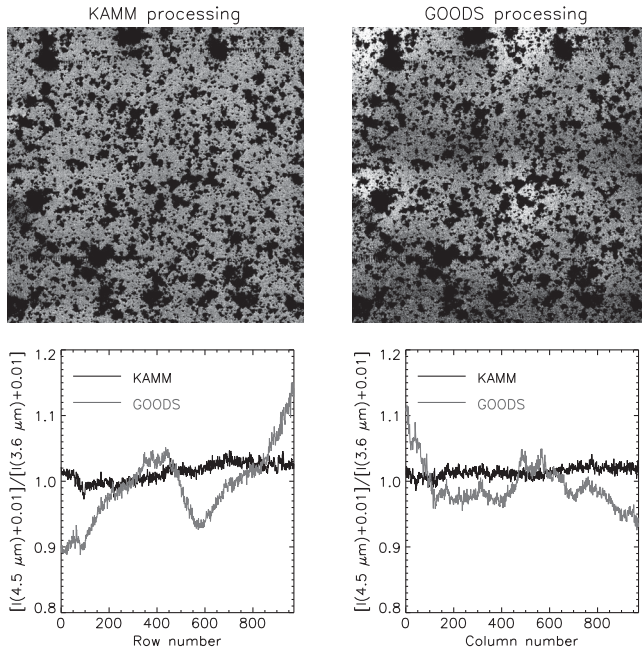
FIG. 11. The effectiveness of self-calibration is illustrated by maps of the ratio of 4.5 to 3.6 μm images of the Chandra deep field south (CDFS) for self-calibrated (left) and more conventional (right) (http://irsa.ipac.caltech.edu/data/SPITZER/GOODS/docs/goods_dr3.html) processing; see the full discussion in Arendt *et al.* (2010). Bright sources in the images have been masked identically. Any color variations in the intrinsic background should not be correlated with the observing mapping pattern. Lower panels compare median intensities across each ratio image as a function of row and column with small offsets added to the ratios so that they are always positive with a mean near 1. The pattern seen in alternative processing is related to the calibration of the detector offsets. From Arendt *et al.*, 2010.

use of an observing strategy that allows the determination of the model parameters for the sky, without degeneracies (Arendt, Fixsen, and Moseley, 2000). Standard Spitzer IRAC observations are designed with this in mind, through the use of relatively large-scale and highly varied dither patterns.

Self-calibration has proved beneficial for the analysis of IRAC data, because it can identify and remove instrumental artifacts that are not fully corrected in IRAC's standard basic calibrated data. The extensive verification of the self-calibration processing was provided by Arendt *et al.* (2010). Figure 11 illustrates the improvement that self-calibration can make in the removal of large-scale background variations induced by the observing strategy and mosaicking procedures.

b. Results

Results obtained with the Spitzer IRAC instrument are discussed in chronological order.

The analysis of early Spitzer observations of the QSO 1700 + 6416 field by Kashlinsky *et al.* (2005) established the methodology later used for such CIB studies and provided the first indication of significant source-subtracted CIB fluctuations. The QSO1700 field encompassed $5' \times 10'$ [1×2 IRAC field of views (FoVs)] integrated over $\sim$8 hr/pix. After applying self-calibration to assemble maps from

individual astronomical observing requests, the assembled maps at 3.6, 4.5, 5.8, and 8 μm were processed by iteratively (1) clipping off resolved sources and (2) removing outer parts of sources via a suitably modified CLEAN algorithm (Högbom, 1974; Arendt *et al.*, 2010) out to a given level of the remaining shot noise (and a given factor above the noise power) to produce the diffuse flux maps suitable for CIB study. The clipped pixels were filled with $\delta F = 0$ as originally done by Kashlinsky *et al.* (2002) and Odenwald *et al.* (2003) so as not to add power per the Parseval theorem. The clipped fraction of the map was $\lesssim 25\%$. The power spectrum of the noise was computed using FFTs from the time-differenced data ($A - B$), and the CIB power was evaluated as $P = P_{A+B} - P_{A-B}$. The clipping was then allowed to run deeper, removing up to $\sim 75\%$ of the map. Then the *correlation function* was evaluated instead and was found to remain consistent in amplitude and shape with the CIB power computed from FFTs at the $\lesssim 25\%$ clipping as shown in the Supplementary Information of Kashlinsky *et al.* (2005). Foreground emission contributions to the measured power were found to be well below the identified fluctuation except at 8 μm, where the signal was consistent with being dominated by Galactic cirrus emissions. However, the diffuse maps at 3.6 and 4.5 μm, on the one hand, and 8 μm, on the other hand, were found correlated at a weak, but statistically significant level suggesting that the populations contributing to the diffuse power at the former wavelengths are also present at the latter. There was no correlation between the removed sources and the residual diffuse flux maps. The power from the remaining known galaxies reproduced well the shot noise at small angular scales, but was shown to be well below the identified CIB power from clustering at $\gtrsim 20''$. It was suggested there that the clustering arises in new populations, posited to be at the first stars era.

After a set of new deeper Spitzer measurements became available through the significantly deeper Great Observatories Origins Deep Survey (GOODS) observing program at $\simeq$24 hr/pix (Dickinson, 2008), Kashlinsky *et al.* (2007b) analyzed the data in four parts of sky probing source-subtracted CIB fluctuations from maps of $10' \times 10'$. Despite the deeper shot-noise levels (see Table III), they identified a similar CIB clustering component extending the measurements to larger angular scales. Importantly, that study allowed one to probe potential systematics better: the deeper observations were from two distinct epochs separated by 6 months, when each epoch was still sufficiently deep ($\sim$12 hr/pix) but when the IRAC detectors were rotated by 180° with respect to the previous epoch. A reanalysis by Kashlinsky *et al.* (2007a) used finer pixelization (0.6″ instead of 1.2″) resulting in a larger fraction of the sky f_{sky} left for the power spectrum computation. If the diffuse fluctuation signal originated from the detectors, it would have been different at the two different orientations contrary to what was observed. Using the new observations at much lower shot noise Kashlinsky *et al.* (2007c) further refined the high-z interpretation of the CIB signal quantifying the high-z luminosity density and the typical source fluxes in that case.

Using an alternative scheme for map production and analysis, Cooray *et al.* (2007) [also Chary, Cooray, and Sullivan (2008)] claimed that the power spectrum drops with

TABLE III.   Analyzed Spitzer CIB data.

(1)	(2)	(3)	(4)	(5)	(6)	(7)	(8)
QSO1700	94.4, 36.1	5×10	7.8	(70, 40)	(24.5, 24.5)	77	Kashlinsky *et al.* (2005)
HDFN-E1	125.9, 54.8	10×10	20.9	(26, 14)	(25.1, 25.1)	77	Kashlinsky *et al.* (2007a, 2007b)
HDFN-E2	125.8, 54.8	10×10	20.7	(26, 14)	*ibid.*	77	Kashlinsky *et al.* (2007a, 2007b)
CDFS-E1	223.7, −54.4	10×10	23.7	(26, 14)	*ibid.*	76	Kashlinsky *et al.* (2007a, 2007b)
CDFS-E2	223.5, −54.4	10×10	22.4	(26, 14)	*ibid.*	77	Kashlinsky *et al.* (2007a, 2007b)
EGS	96, 59.8	8×62	12.5	(50, 30)	(24.75, 24.75)	73	Kashlinsky *et al.* (2012)
UDS	170, −59.9	21×21	13.6	(50, 30)	*ibid.*	73	Kashlinsky *et al.* (2012)
Bootes	57.5, 67.3	$3.5° \times 3°$	0.1	(80, 100)	(24.3, 23.8)	47	Cooray, Gong *et al.* (2012)

[a]Columns: (1) Name of the field. (2) Galactic coordinates $(l_{Gal}, b_{Gal})°$. (3) Size ($'$). (4) $\bar{t}_{exp}$ (hr) (5) P_{SN} at (3.6, 4.5 μm) in nJy nW/m^2/sr. (6) Limiting m_{AB} at (3.6, 4.5 μm). (7) Sky fraction f_{sky} in % remaining for $P(q)$ computation. (8) References.

additional masking from shorter band data and the signal originates in faint blue galaxies located at the peak of star formation and not associated with first stars era. However, their maps had only 20%–30% of the sky remain for FT and Kashlinsky (2007) showed that, in their data, when the correlation function is computed for such heavily masked maps instead, the signal remains the same within the statistical uncertainties. After adopting the self-calibration scheme of Arendt *et al.* (2010) that claim appears to have been abandoned (Cooray *et al.*, 2012). Kashlinsky *et al.* (2007a) found no correlations between the source-subtracted CIB fluctuations from clustering identified in Spitzer data and very faint galaxies found in visible with HST Advanced Camera for Surveys (ACS) out to 0.9 μm and $m_{AB} \gtrsim 28$.

These analyses were all done for the Spitzer cryogenic mission, which ended in 2009 after the telescope's supply of cryogen was exhausted. In the warm Spitzer mission only IRAC's channels at 3.6 and 4.5 μm remained operational. During the warm mission observation, the SEDS observing program (Ashby *et al.*, 2013) supplied new data that, while at a depth of 12–13 hr/pix were intermediate between the QSO1700 and GOODS observations, covered substantially larger areas of the sky. Kashlinsky *et al.* (2012) processed the suitably covered areas extending, for the time, the measurements to ~1° where the signal remained consistent with a high-z population of sources as posited in the original analysis of Kashlinsky *et al.* (2005). It was shown that, correcting a high-z ΛCDM power template for masking effects iteratively, the measured power is well reproduced by a population clustered in that manner.

Figure 12 shows the CIB fluctuation data from seven different regions in the sky analyzed at the shot-noise level of the QSO1700 field. At similar shot-noise levels the signal
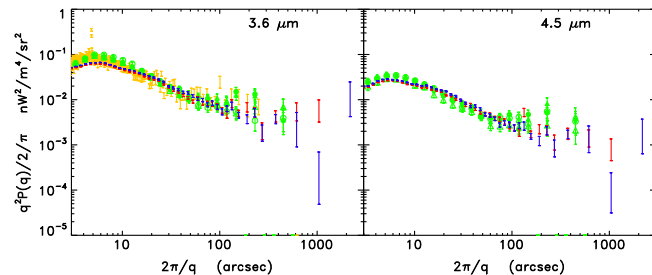
appears isotropically distributed on the sky, consistent with its cosmological origin.

The dependence of the Spitzer first results on the clipping was addressed by Kashlinsky *et al.* (2005). Figure 13 shows the CIB correlation function from that analysis for the various clipping and demonstrates robustness of the measured signal in the presence of more aggressive masking, specified by a deeper cutting parameter N_{cut} and a wide mask size for each pixel applied N_{mask}.

Figure 14 shows the CIB fluctuation, including the cross power, to ~1° averaged over two SEDS field at the shot-noise levels corresponding to $\simeq 13$ hr/pix. The cross power that could be identified because the region of overlap between the
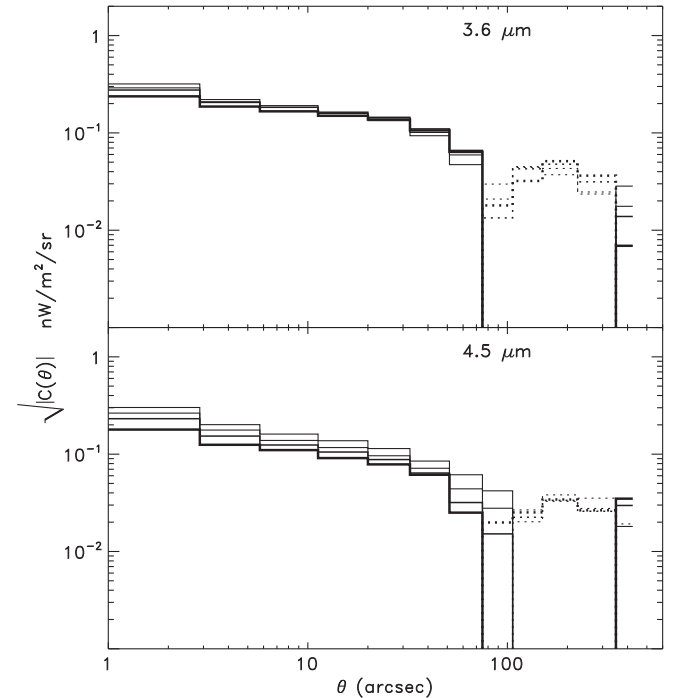

FIG. 13.   A correlation function derived by Kashlinsky *et al.* (2005) for deep clipping of the Spitzer data out to $f_{sky} = 30\%$ of the pixels remaining for the analysis. Deeper clipping is specified by a lower value of the cutting parameter N_{cut}, while the masking area around each pixel is increased by an increased value of N_{mask}. Solid lines show positive $C(\theta)$, and the dotted lines correspond to $C < 0$. Adapted from Kashlinsky *et al.*, 2005.

FIG. 12.   Spitzer-based CIB fluctuation data from seven different fields at similar shot-noise levels. From Kashlinsky *et al.*, 2012.
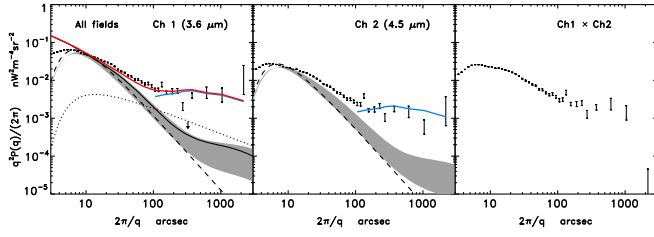
FIG. 14. Field-averaged CIB fluctuations at 3.6 and 4.5 μm and the cross-power spectrum. The dotted line shows the upper limit on CIB fluctuations from remaining known galaxies derived by Kashlinsky *et al.* (2005). The solid black line is the contribution of the remaining ordinary galaxies per Sullivan *et al.* (2007) which clearly lies beneath the data contrary to the text there. Shaded areas show the reconstructed residual fluctuations from Helgason, Ricotti, and Kashlinsky (2012) due to ordinary galaxies. The dashed lines show the shot-noise contribution: $P_{SN} = 57.5$ nJy nW/m^2/sr (or 4.8×10^{-11} nW^2/m^4/sr) at 3.6 μm and $P_{SN} = 31.5$ nJy nW/m^2/sr (2.2×10^{-11} nW^2/m^4/sr) at 4.5 μm. The solid blue lines correspond to the high-z ΛCDM (toy) model processed through the mask of each field and then averaged. The "toy" model here refers to the template of $k^2 P_{3D}$ evaluated at $k = qd_A$ with $d_A \sim 7$ Gpc corresponding to $z \sim 10$ and with the amplitude fitted to the data. The thick solid red line shows the sum of the three components. From Kashlinsky *et al.*, 2012.

two IRAC channels was large for SEDS observations appears consistent between the two IRAC channels despite their separate optical paths. The shape of the clustering component to ~1° is consistent with sources distributed according to the high-z ΛCDM model.

Cooray *et al.* (2012) reproduced the source-subtracted CIB fluctuations from a much shallower, but wider Bootes field. The Spitzer integrations were only 6 min /pix over a net area of 8 deg^2 and additional optical data were used to remove sources to a sufficiently low shot-noise level, but leaving less than 50% of the assembled map for power spectrum computation. They identified the signal to ~1°, consistent with an earlier analysis of Kashlinsky *et al.* (2012) and suggested an alternative origin for the fluctuations arising in the IHL from new populations stripped of their paternal galaxy halo at intermediate redshifts $z \sim 2$–3.

Table III sums up all the Spitzer-based measurements in the various sky configurations discussed. The signal appears the same in different locations and has now been measured to ~1°. Its origin is now agreed upon to arise in new sources with two competing theories of a high-z origin or IHL at low to intermediate z.

c. Foreground contributions

Foreground contributions are important to evaluate. Zodiacal light is the strongest foreground in terms of total intensity. However, the zodiacal light is very smooth on a wide range of angular scales. Apart from distinct orbital structures: the asteroidal dust bands, the Earth-resonant ring, and comet dust trails, only upper limits have been set on the structure of the zodiacal light at mid-IR wavelengths where zodiacal light is brightest (Abraham, Leinert, and Lemke, 1997; Pyo *et al.*, 2012). Extrapolating these limits to Spitzer's

near-IR wavelengths indicates that spatial fluctuations of the zodiacal light must be comparable or less than the observed fluctuations.

More direct and restrictive estimates of the possible contribution of zodiacal light to large-scale fluctuations have been made by examining the power spectra in *A-B* difference maps, where *A* and *B* represent observations of the same field collected ~6 or 12 months apart (Kashlinsky, 2005a). These power spectra isolate the contribution of the zodiacal light, because the structure must vary with time and thus does not cancel out as do the Galactic and extragalactic signals. Similarly, the presence of significant cross correlation between the structure at different epochs indicates that zodiacal light cannot be the dominant signal (Kashlinsky *et al.*, 2012).

Most recently, Arendt *et al.* (2016) examined the 3.6 and 4.5 μm power spectra for a $10' \times 10'$ region in the COSMOS field for five epochs. The epochs were chosen to span the widest possible range of solar elongation and brightness variation of the zodiacal light. They found that the large-scale power showed no correlation with the zodiacal light intensity, but noted that roughly 50% of the white noise (best characterized at the smallest scales) correlates with the zodiacal light intensity, presumably due to the photon shot noise of the zodiacal light.

A different foreground to consider is stellar emission from our Galaxy. The unresolved starlight is a significant contributor to the mean IR background in low resolution studies, such as COBE DIRBE (Arendt *et al.*, 1998; Hauser *et al.*, 1998). However, with higher angular resolution and sensitivity, resolved sources can be identified and subtracted from the data at a level well below the point where extragalactic sources outnumber Galactic stars (Ashby *et al.*, 2013).

Emission from the Galactic ISM (i.e., cirrus) is perhaps the most difficult foreground to address. Estimates of the contribution of cirrus emission to the fluctuations are generally made by extrapolation of measurements made at other wavelengths and locations where the ISM is more easily detected. In some fields, there is evident cirrus at 8 μm where polycyclic aromatic hydrocarbon (PAH) features yield relatively bright emission. In these cases, an upper limit on the cirrus contribution at shorter wavelengths can be made by assuming that the 8 μm power spectrum is dominated by cirrus and rescaling the power spectrum to a shorter wavelength using a spectral energy distribution established from observations in low-latitude Galactic studies (Kashlinsky, 2005a; Arendt *et al.*, 2010; Kashlinsky *et al.*, 2012).

d. Contribution from remaining known galaxies

Contribution from remaining known galaxies needs to be robustly estimated in the balance of the CIB. In the original study Kashlinsky *et al.* (2005) have already shown that CIB clustering from known galaxies below the removal threshold would fall below the observed signal even if the power law of galaxy clustering observed on small scales extends to the larger scales. This is indicated by the dotted line as an upper limit in Fig. 14. In other words, if populations at lower redshifts and spanning longer cosmic periods with less biasing were to explain the measurement, they would require production of much larger CIB, which would be comparable to

the net CIB flux at 3.6 and 4.5 μm from all the known galaxies out to $m_{AB} \gtrsim 26$ (Fazio *et al.*, 2004a; Ashby *et al.*, 2013, 2015). In their calculations Sullivan *et al.* (2007) confirmed this, as shown in their Fig. 8, although the text of the paper contradictorily states throughout that the clustering can be produced by normal galaxies at $22.5 < m_{\text{Vega}} < 26$. Their estimate, shown as the solid line in Fig. 14, is below the upper limit worked out earlier by Kashlinsky (2005a). Helgason, Ricotti, and Kashlinsky (2012) did a sophisticated analysis described in Sec. IV.B and confirmed this, further lowering the possible contributions from known galaxy populations at $z \lesssim 6$.

e. Coherence with unresolved CXB

Coherence with unresolved CXB has been identified by Cappelluti *et al.* (2013) in the Chandra-based cross-correlation analysis of the source-subtracted CIB and CXB maps. The Chandra x-ray observatory is sensitive to x rays in the [0.1–10] keV band with an energy resolution of 150 eV and a FoV of $16.9' \times 16.9'$. The sharp imaging capabilities of Chandra and its highly elliptical orbit allow observations with a very low background. In x-ray observations there are two main background components, one which is purely astrophysical produced by blending of all sources below the detection limit (CXB) and diffuse emission from the Galaxy and the local hot bubble. The source-subtracted CXB flux depends on the observation depth since deeper exposures yield a larger fraction of resolved CXB. The second component, which we call the particle internal background (PIB), arises from charged solar wind or cosmic ray particles interacting with the spacecraft and/or producing secondary x-ray photons by fluorescence. The local (Galactic) components of the x-ray diffuse emission are dominant at low energy ($E < 1.5$–2 keV) while, at higher energies, the PIB and the extragalactic CXB dominate the signal.

Because of the grazing incidence design of x-ray telescopes (in contrast to optical and IR telescopes), regions of the detector close to the optical axis have better point-source sensitivity than outer parts of the field of view: the PSF full width at half maximum (FWHM) varies from $0.5''$ on axis to $>8''$ off axis. Also the effective area varies with the off-axis angle. As a result, on-axis sources would produce a detection while off-axis ones would instead contribute to CXB. This means the mean background level is a function of the off-axis angle. These properties are important to consider when studying unresolved CXB fluctuations. An advantage of x-ray data, compared to optical or near IR, is that for every photon the charge-coupled device (CCD) records time of arrival, energy, and position. In this way, by sorting the events by time of arrival one can produce maps of odd (A) and even (B) events to be used later for time-differenced (A-B) evaluation of the noise floor in power spectra.

Cappelluti *et al.* (2013) used 1.8 Ms data from the All-wavelength Extended Groth Strip International Survey—X Ray, Deep (AEGIS-XD) survey to produce CXB fluctuation maps $\delta F_X(\vec{x})$ after removing x-ray detected sources (Goulding *et al.*, 2012). The AEGIS-XD survey consists of 66 Chandra Advanced CCD Imaging Spectrometer—Imaging arrays (ACIS-I) pointings. The common area between Chandra and Spitzer is a narrow strip of $8' \times 45'$. A subsequent analysis of CIB-CXB cross power by Mitchell-Wynne *et al.* (2016) used 4 Ms of Chandra and Spitzer data in the CDFS area covering $\sim$110 arcmin^2. Both used the approach developed by Cappelluti *et al.* (2012) and improved by Cappelluti *et al.* (2013) for producing x-ray fluctuation maps: resolved point sources such as AGN, star-forming galaxies, x-ray binaries, and diffuse galaxy clusters are removed as the first step of map production. X-ray sources have a low source surface density compared to optical and near-IR sources. Lehmer *et al.* (2012) showed that at the depth of Chandra deep fields, the source density is of the order of $\sim$3 $\times$ 10^4 sources/deg^2. This means that masking x-ray sources removes less than 10% of the pixels. However, when producing x-ray fluctuation maps one must also take into account peculiarities of x-ray telescopes, such as the position-dependent amplitude and the nature of the two components of the background (i.e., the CXB and the PIB). To model the PIB they took advantage of the observations of ACIS-I in the stowed mode. The instrument is exposed but is stowed out of the focal plane and far from the onboard calibration source, when only the PIB signal is present. Since the mean PIB level in this "dark frame" differs from the observation but its spectral shape is constant within 1%–2%, these maps are then scaled to match the actual background level. After masking and subtracting the background they evaluate the position dependence of the astrophysical background using an exposure map. Another effect to account for is the low pixel occupation number of x-ray photons (e.g., in the full [0.5–7] keV band $\sim$1.1 photons/Ms/pix). This means that the Poisson noise dominates the noise on small scales.

To measure the x-ray spectrum of the CIB-CXB cross power, while still minimizing the Poisson noise, Cappelluti *et al.* (2013) divided the total counts into three x-ray bands, [0.5–2], [2–4.5], and [4.5–7] keV, each with $\sim$130 000 x-ray photons. In a later analysis, Mitchell-Wynne *et al.* (2016) used deeper exposures of a much smaller field, collecting about one-fourth of the photons used in the earlier study but with a similar occupation number.

Cappelluti *et al.* (2013) also studied the dependence on the masking by subjecting the data to (1) the IR mask from Kashlinsky *et al.* (2012) and (2) an x-ray mask that specifically removes x-ray groups and cluster down to $\sim$10^{13} $M_\odot$. CIB power spectra with or without the additional x-ray masking agree to better than 5% on all scales, consistent with the populations responsible for the CIB fluctuation signal being unrelated to the remaining known galaxy or galaxy cluster populations in the field.

After verifying that the CIB and CXB map noises were uncorrelated, the cross-correlation analysis between [0.5–2], [2–4.5], and [4.5–7] keV was performed with the IRAC source-subtracted CIB maps at 3.6 and 4.5 μm. Their analysis identified the cross power between $4''$ and $1200''$ and evaluated the significance by characterizing the actual dispersion of the cross power on scales of $10''$–$1000''$. In Cappelluti *et al.* (2013) the overall CXB-CIB cross power was significant at 3.6σ and 5.6σ for 3.6 and 4.5 μm vs [0.5–2] keV, respectively, while no significant correlation between any IRAC maps and harder x-ray channels was identified. Mitchell-Wynne *et al.* (2016) found 3.7σ and 4.7σ significant cross powers above $20''$. Unlike Cappelluti *et al.* (2013) they also found a marginally significant
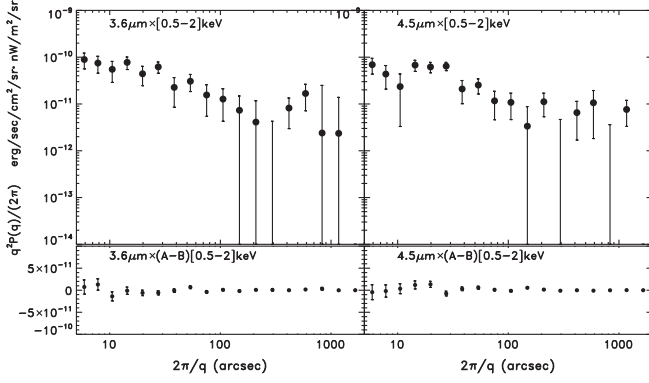
FIG. 15. Based on results from Cappelluti, Arendt *et al.* (2017). Top: The fluctuations' cross-power spectrum between IRAC 3.6 (left) and 4.5 μm CIB and Chandra soft CXB. Bottom: Same but for the noise of Chandra time-differenced data.

signal in 3.6 μm vs [2–7] keV (2.7σ) and 4.5 μm vs [2–7] keV (3.7σ), respectively.

The new study by Cappelluti, Arendt *et al.* (2017) used data from the Chandra Deep Field South (CDFS), Hubble Deep Field North (HDFN), All-wavelength Extended Groth Strip International Survey (AEGIS), and Subaru/XMM-Newton Deep Survey (SXDS) comprising 1160 Spitzer hours and $\simeq$12 Ms of Chandra data collected over a total area of 0.3 deg^2. They showed the consistency between the measured cross powers in each of the regions and, after combining, reported a highly significant detection of a cross-power signal from clustering on large angular scales $> 20''$ between the 3.6 μm or 4.5 μm bands and the [0.5–2] keV band. The total significance of the detected clustering component of the cross power is $\simeq 5\sigma$ and $\gtrsim 6\sigma$. The level of coherence between the two background fluctuations from clustering is at least $\mathcal{C} \sim 0.15$–0.2, this being a *lower* limit with the CXB power of the new sources being unknown and limited from above observationally. At the same time they found no significant correlation with harder x-ray bands. Accounting for the contribution of known unmasked source population at $z < 7$, this excess appears about an order of magnitude at the 5σ level.

Figure 15 presents the overall results for the 3.6 and 4.5 μm cross powers with the soft [0.5–2] keV unresolved CXB from Cappelluti, Arendt *et al.* (2017).

f. Spitzer CIB cross correlations

Spitzer CIB correlations with diffuse light at other wavelengths were probed in several studies as a tool to provide insight in addition to cross correlating source-subtracted CIB from Spitzer with unresolved CXB fluctuations. Of particular relevance to interpretation would be whether the CIB correlates with visible light since any high-z CIB component should not exhibit a visible counterpart because of the Lyman break in the sources around $\simeq 0.12 \, (1 + z) \, \mu$m. Soon after the discovery of the source-subtracted CIB fluctuations with Spitzer, Kashlinsky *et al.* (2007a) demonstrated that there are no correlations between the source-subtracted IRAC maps and the HST ACS data to $m_{AB} \simeq 28$. This result implies that the Lyman-break wavelength is redshifted beyond

the longest ACS wavelength at 0.9 μm unless the CIB anisotropies come from more local but extremely faint ($L < 2 \times 10^7 L_\odot$) and so far unobserved galaxies. This likely requires that the detected CIB fluctuations arise from objects within the first Gyr of the Universe's evolution (Mitchell-Wynne *et al.*, 2015).

At longer wavelengths, Kashlinsky *et al.* (2012) found only marginal correlations between their 3.6 and 4.5 μm source-subtracted diffuse maps with those at 8 μm, consistent with either cirrus, remaining known galaxies, or new populations contributing to diffuse light at both wavelengths. Matsumoto *et al.* (2011) found no correlations of the AKARI source-subtracted diffuse maps with the AKARI far-IR data at 100 μm. Thacker *et al.* (2015) claimed a cross correlation of Spitzer data with diffuse maps from Herschel at 250, 350, and 500 μm. The Spitzer data at 3.6 μm, with a 0.1 hr net integration depth, was repixelized at the common resolution of 6$''$, leading to both significantly larger removed sky and greater shot noise (i.e., shallower depth) in the combined images. The resultant images had less than 40% of the map pixels available for Fourier analysis, yet the correlation function has not been evaluated in the paper to substantiate the robustness of the strong cross power on subdegree scales, which was interpreted as coming mostly from IHL. However, a close look shows that the adopted contribution from remaining known galaxies (Thacker *et al.*, 2015, green dashes in Fig. 9) without uncertainties corresponds to the low-faint end of the HRK12 reconstruction. Our evaluation of the high-faint-end limit of the HRK12 reconstruction for the appropriate parameters, which is equally plausible, increases the CIB power from remaining galaxies by up to an order of magnitude on subdegree scales. Consequently, the power from remaining known galaxies could be revised upward by a high enough factor to largely explain the claimed levels of coherence with remaining known galaxies. The uncertainties in the contributions from remaining known galaxies are thus sufficient to account for the claimed coherence at the levels of $\mathcal{C} \sim (1$–3)%: the cross power can be explained if about $\sqrt{\mathcal{C}} \sim 10\%$ of the sources are common to both the near- and far-IR channels. Galactic cirrus further increases the cross power, particularly at the largest angular scales probed. The claimed necessity of the IHL in explaining the reported cross power advanced by Thacker *et al.* (2015) thus appears unsubstantiated.

2. AKARI

AKARI is the most recent Japanese IR satellite (Murakami *et al.*, 2007). Its 0.68 m telescope is 20% smaller than Spitzer's, leading to a lower angular resolution, but the field of view of AKARI's Infrared Camera (IRC) (Onaka *et al.*, 2007) is 10$'$, which is twice as wide as Spitzer's IRAC. The IRC obtained images in three near-IR bands at 2.4, 3.2, and 4.1 μm, with 1.46$''$ pixels. It also included mid-IR bands at 7, 9, and 11 μm with 2.34$''$ pixels and 15, 18, and 24 μm with $\sim$2.45$''$ pixels.

Matsumoto *et al.* (2011) used IRC data from the north ecliptic pole (NEP) monitor field to investigate fluctuations in the CIB in the three near-IR bands. The NEP monitor field (Wada *et al.*, 2007) was observed regularly throughout the
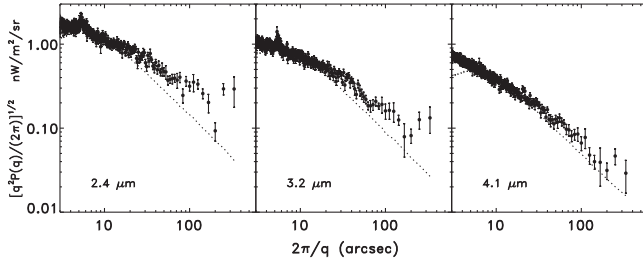
FIG. 16. Power spectra in the AKARI monitor field after subtraction of the noise power measured from dark maps The dotted lines show the fitted shot (white) noise levels of remaining sources that were too faint to subtract or mask. Convolution with the beam attenuates the power in this component at the smallest angular scales. Adapted from Matsumoto *et al.*, 2011.

mission. Observations were dithered over a single $10'$ field of view, but the field rotation throughout the mission yields a uniformly covered circular region of $10'$ in diameter. The shot-noise level after source subtraction and masking corresponds to limiting *AB* magnitudes of 22.9, 23.2, and 23.8 at wavelengths of 2.4, 3.2, and 4.1 μm, respectively (Matsumoto *et al.*, 2011).

Matsumoto *et al.* (2011) described the procedures used for data reduction, including flat fielding, dark subtraction, and corrections for instrumental artifacts. Source subtraction on the final stacked images was very aggressive. Pixels in the maps exceeding 2σ were masked, and the procedure was iterated, until no further pixels exceeded 2σ. To remove lower surface brightness portions of sources, the Image Reduction and Analysis Facility DAOPHOT package was used to find and subtract sources as seen in the unmasked images to the 2σ level, and higher resolution ground-based K_s band images were convolved with the IRC PSF and used to subtract the emission of extended sources. These source-subtracted images were then masked with the original 2σ clipping mask, plus an additional margin of 1 pixel ($1.5''$) around all clipped regions. This left ~47% of the circular field available for analysis.

A power spectrum analysis, using FFT, of the source-subtracted and clipped images revealed spatial fluctuations in the data in excess of the power shown in dark maps, generated from an equivalent number of concurrent dark frames. The dark maps are found to be similar to time-differenced *A-B* maps, which are generated by inverting the sign of half the data, so that any fixed signal cancels out and only noise (and systematic errors) remain. The power that is measured in excess of the *A-B* noise appears to be dominated by shot-noise (white) components at small angular scales, but with a nonwhite excess increasing at large scales ($\gtrsim 50''$), especially at 2.4 and 3.2 μm (Fig. 16).

Because of the large clipping fraction, Matsumoto *et al.* (2011) also verified their FFT-based power results by computing the correlation function. The correlation function, reproduced in Fig. 17, also indicates the presence of large-scale structure, and cross correlations show that the structure is similar in all three near-IR bands. Importantly, the cross power evaluated there confirms that the same populations are present at all wavelengths and cluster on similarly large scales.
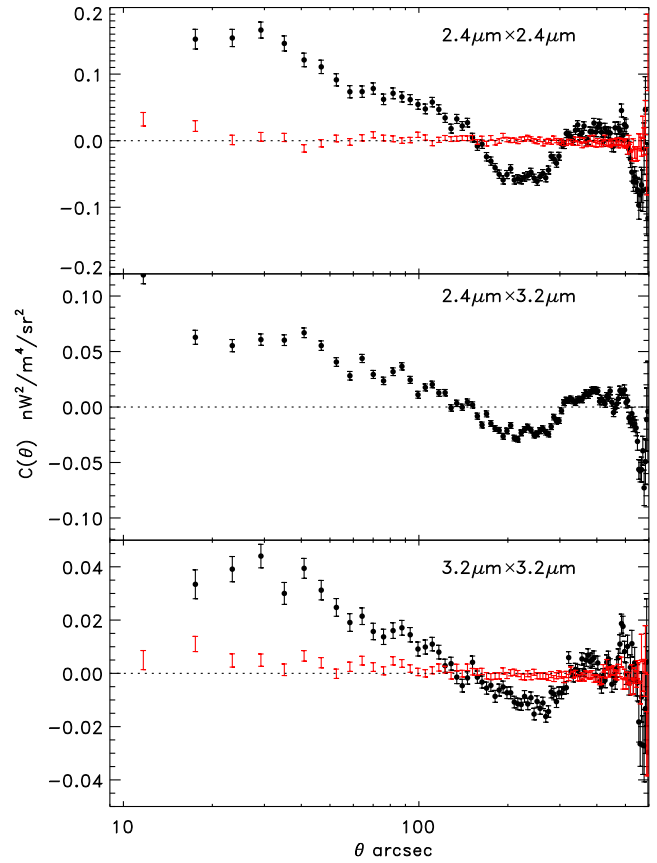

FIG. 17. Correlation and cross-correlation functions for the source-subtracted backgrounds in the AKARI monitor field. The pixel scale of the maps was modified from $1.5''$ to $6''$ to speed up these calculations at the expense of finer resolution. The errors bars without symbols (red) are derived from the dark maps. The black symbols are derived from the actual sky maps and clearly show significant large-scale structures. Adapted from Matsumoto *et al.*, 2011.

Furthermore, since the shot-noise contribution to $C(\theta)$ is contained within $C(0)$, the correlation function directly isolates the clustering component of the underlying populations.

The amplitudes of the power spectra at large angular scales are indicative of the mean SED of the sources that produce the fluctuations. The SED is found to rise toward shorter wavelengths with a slope similar to the Rayleigh-Jeans tail of a blackbody (Fig. 18). This is consistent with the rising SED implied by the Spitzer IRAC data, but extends the trend to shorter wavelengths (2.4 μm).

Seo *et al.* (2015) extended the Matsumoto *et al.* (2011) analysis to larger angular scales by using data from the NEP deep survey (Wada *et al.*, 2008). These data are not as deep as the monitor field, but span angular scales up to $1000''$ (Fig. 19). Seo *et al.* (2015) used only 2.4 and 3.2 μm data from this data set, because the 4.1 μm band had insufficient depth for source-subtracted CIB studies. The data reduction used by Seo *et al.* (2015) is similar to that used by Matsumoto *et al.* (2011). However, the analysis of the source-subtracted images differs as power spectra are corrected for mode coupling due to masking, the map-making transfer function, and the beam via the same procedure as in Cooray *et al.*

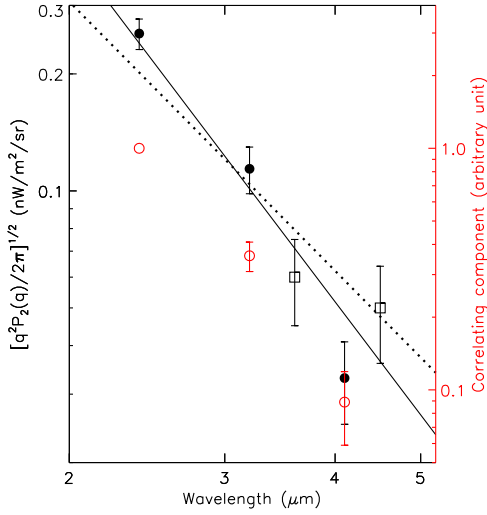FIG. 18. The spectral energy distribution of the source-subtracted background fluctuations averaged over scales of $100''$–$350''$ from AKARI measurements (filled circles) is compared to that of Spitzer (open squares). The open red circles are the SED derived from the slopes of pixel-to-pixel correlation of the AKARI 3.2 and 4.1 μm data with its 2.4 μm data (scaled on the red right-hand vertical axis); the 2.4 μm open red circle hence has no error bar as its correlation is 1.0 by definition. Solid and dotted lines are a Rayleigh-Jeans ($\nu I_\nu \sim \lambda^{-3}$) fit to the AKARI data, and a model of the expected SED of high-z Population III sources [Fig. 20 of Fernandez *et al.* (2010)]. Adapted from Matsumoto *et al.*, 2011.

(2012). Although the clipping fraction approaches 70% in the maps, no correlation function was presented.

Both Matsumoto *et al.* (2011) and Seo *et al.* (2015) considered, tested, and rejected the possibility that zodiacal light or Galactic foregrounds can contribute to the reported power at large angular scales ($\gtrsim 100''$). Matsumoto *et al.* (2011) ruled out zodiacal light because of the lack of signal in *A-B* tests using data collected at different times, the discrepancy between the SED of the residual large-scale power and the zodiacal light, and the extrapolation from limits on the zodiacal light fluctuations established in the mid IR (Pyo *et al.*, 2012). The extrapolation was also used by Seo *et al.* (2015) to rule out zodiacal light. The contribution of faint Galactic stars is dismissed in both papers, as both resolve sources to depths where source counts are strongly dominated by galaxies rather than Galactic stars. Both papers rule out cirrus contributions, based on the lack of correlation with far-IR emission at 90 μm (Matsuura *et al.*, 2011), which does show evidence of cirrus emission at the NEP. In contrast, at mid-IR wavelengths (7–11 μm) Pyo *et al.* (2012) found that the large-scale mid-IR power can be accounted for by rescaling the large-scale power at 90 μm according to a typical cirrus spectrum. At 15–24 μm Pyo *et al.* (2012) reported the photon shot noise as the dominant component of the power spectrum, even at large angular scales.

The upshot of the AKARI-based analysis is (1) consistency with the Spitzer results at 3.6 and 4.5 μm, (2) identification of the source-subtracted CIB at 2.4 μm and demonstrating via cros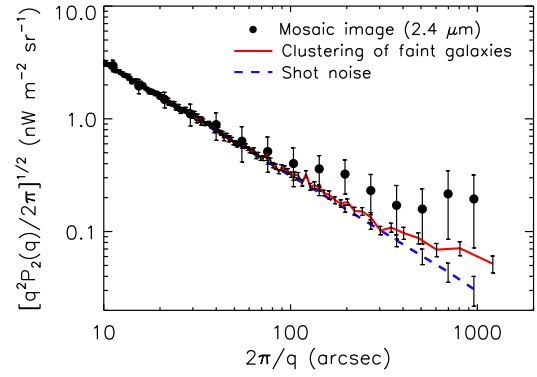s correlation that it arises from the same populations as at the AKARI longer IRC channels, and (3) identifying the energy spectrum of the sources-subtracted CIB which approximates $\nu I_\nu \propto \lambda^{-3}$.

Helgason and Komatsu (2017) suggested possible systematics in the interpretation due to the beam modeling uncertainties of Matsumoto *et al.* (2011): the deduced shot-noise level is sensitive to the beam and with the beam from Seo *et al.* (2015) they recovered a larger shot-noise power. This decreases the effective limiting magnitude by $\Delta m \sim 0.5$ resulting in larger contributions from remaining known galaxies, which they suggested are enough to explain the bulk (although not all) of the detected CIB *power spectrum*. They pointed out, however, that "the same is not true for Spitzer IRAC measurements at similar wavelengths, which still show fluctuations in excess of what can be attributed to faint galaxies" and which are consistent with the AKARI results as discussed next. While this is indeed an important point, we note that the power they attribute is predominantly shot noise, is flat, and will not contribute to the measured by AKARI correlation function beyond the beam scale ($\theta \sim 3''$), which is shown in Fig. 17 and which they do not attempt to model. The correlation function shows the same populations at all of the AKARI wavelengths, which are highly coherent and with a distribution distinct from white or shot noise.

3. Currently established CIB fluctuation properties at 2–5 μm

We now sum up the properties of the source-subtracted CIB fluctuations that currently appear established in this wavelength range.

a. Cosmological origin of fluctuations in new populations

Figure 12 illustrates that the CIB fluctuation signal from clustering detected by Spitzer is consistent with being isotropic on the sky as required by its cosmological origin. Figure 20 shows that the same signal is present in the AKARI measurements at the adjacent wavelengths. The fields analyzed using Spitzer data and shown in Table III span a factor of ~ 3 in cirrus intensity, yet exhibit a consistently similar large-scale component out to $\sim 1°$. Likewise, the signal appears temporarily

FIG. 19. The 2.4 μm power spectrum of the source-subtracted AKARI NEP deep field, compared to the shot-noise level, and the power expected from faint remaining galaxies as derived from simulations. At scales $> 100''$ the measured power exceeds that expected from the remaining galaxies that are too faint to subtract or mask. Adapted from Seo *et al.*, 2015.
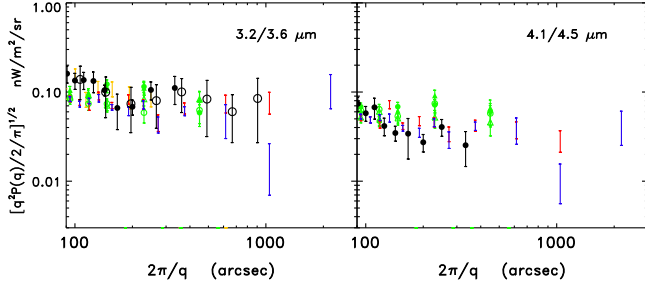
FIG. 20. Comparison of CIB fluctuations from AKARI with Spitzer. Spitzer results are shown in the same color scheme as Fig. 12. AKARI results are scaled to Spitzer wavelengths with the $\propto \lambda^{-3}$ SED: the black filled circles are from Matsumoto *et al.* (2011) and the black open circles on the left panel are the shallower measurements from Seo *et al.* (2015) at 3.2 μm with higher shot-noise levels dominating small scales. All measurements trace the same populations at angular scales $\gtrsim 30''$, although, because of their shallower depth and smaller area, the AKARI data are more polluted by the remaining known sources.

invariant suggesting a small, if any, contribution from zodiacal emission. The detected CIB fluctuation thus appears to arise from clustering of new extragalactic populations. The CIB fluctuations contain two components: small scales arise from the shot noise from remaining galaxies and large scales arise from the clustering of contributing sources.

b. Contribution from remaining known galaxies

The contribution from remaining known galaxies appears negligible at large scales from Spitzer measurements, but the situation may be less clear for AKARI, given the somewhat small deep field (Matsumoto *et al.*, 2011) which leads to larger statistical uncertainties, or the shallower wider field

(Seo *et al.*, 2015) which leaves pollution from remaining known galaxies at larger levels. Nonetheless, the AKARI data at 2.4 μm exhibit excess at larger scales that are consistent with large-scale fluctuations from Spitzer at 3.6 and 4.5 μm, and the correlation functions evaluated there show clear deviations from shot-noise dominating remaining known galaxy contributions at all wavelengths. Figure 21 sums up the contributions from the remaining known galaxies to the measured powers.

c. Spectral energy distribution

The AKARI-based analysis extended the CIB fluctuation measurement to 2.4 μm and suggested an approximately Rayleigh-Jeans–type spectral energy distribution of the sources producing them, $\nu I_\nu \propto \nu^{-\alpha}$ with $\alpha \sim 3$. Figure 21 shows the combined AKARI and Spitzer results with a fit of a high-z ΛCDM template extrapolated from the Spitzer band to the AKARI 2.4 μm channel shown in blue; the solid line shows the least-squares amplitude derived at 2.4 μm and the blue dotted line denotes the 1σ error span.

d. Clustering component versus shot-noise power

The source-subtracted CIB fluctuations measured with Spitzer data appear with low shot noise, while exhibiting a substantial clustering component, which indicates the origin of the clustering component in very faint populations (currently $S \lesssim 20$ nJy at 3.6 and 4.5 μm). The source-subtracted CIB fluctuations measured from Spitzer data at progressively lower shot-noise levels are shown in Fig. 22. The clustering component does not yet appear to decrease as the shot noise is lowered by a factor of ~ 6 in analyses using progressively deeper exposures. This has important cosmological implications for proposed models as summarized in the figure caption and discussed further later.
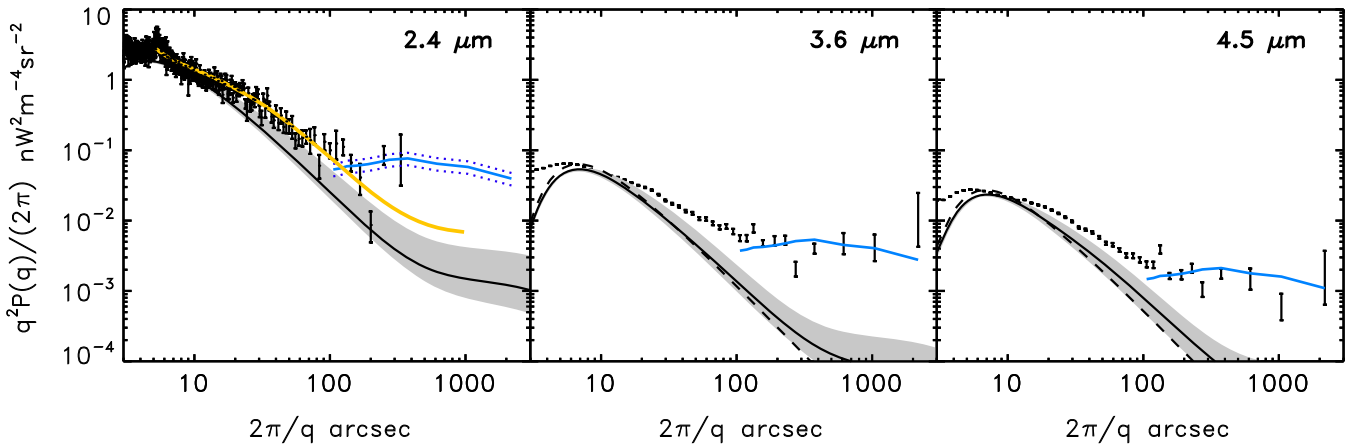

FIG. 21. Mean squared source-subtracted CIB spatial fluctuations at 2.4, 3.6, and 4.5 μm. The black dashes show the shot-noise component remaining in the IRAC maps. The black solid line shows the "default" reconstruction of the CIB from remaining known galaxy populations with uncertainty shown by the shaded area from Helgason, Ricotti, and Kashlinsky (2012); the yellow line shows the contribution from Helgason *et al.* (2016) at the revised AKARI shot noise. The blue solid line shows the template of the high-z ΛCDM model; it is extrapolated to the 2.4 μm data from the IRAC channels using the λ^{-3} energy spectrum with the uncertainty marked with blue dots. Left panel: AKARI results (Matsumoto *et al.*, 2011). Middle and right panels: IRAC results (Kashlinsky *et al.*, 2012). Adapted from Kashlinsky, Mather *et al.*, 2015.
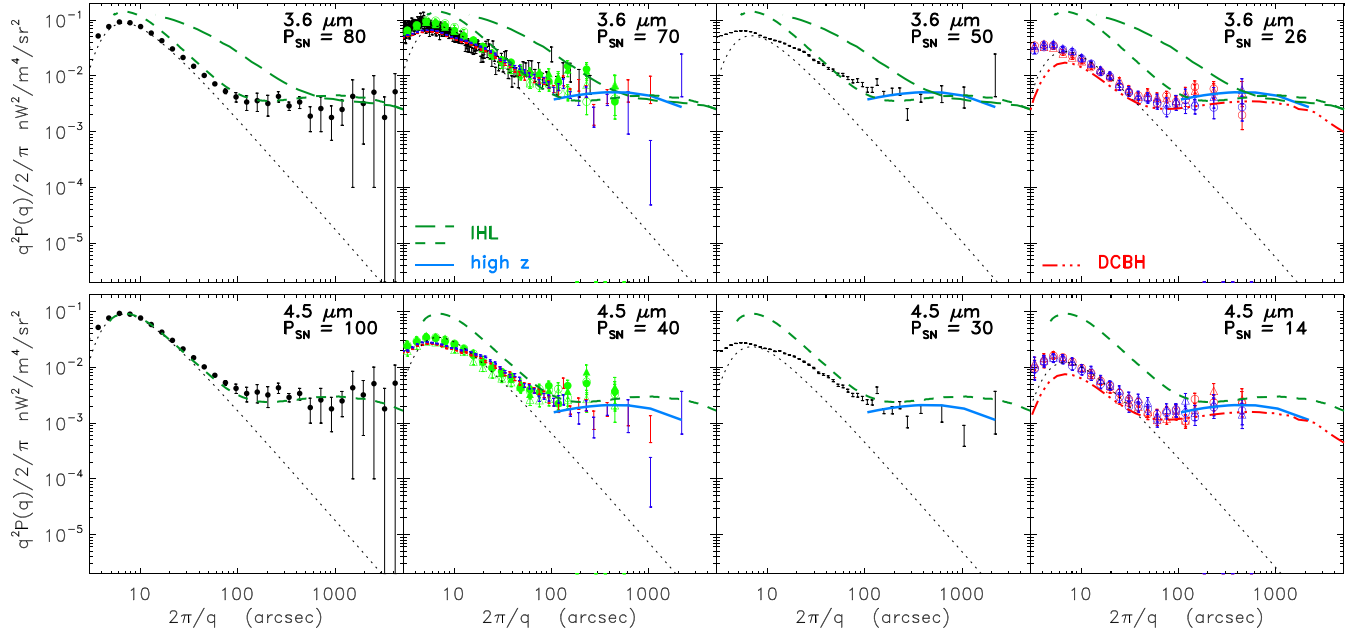
FIG. 22.   Current Spitzer IRAC-based measurements at different shot-noise levels (decreasing in amplitude from left to right) from Kashlinsky (2005a), Kashlinsky *et al.* (2007a, 2012), and Cooray *et al.* (2012). The remaining shot-noise power P_{SN} is shown in each panel in units of nJy nW/m^2/sr. The upper panels correspond to 3.6 μm, and the lower to 4.5 μm. Dotted lines show the remaining shot-noise fluctuation in the Spitzer IRAC maps convolved with the IRAC beam. No decrease of the large-scale clustering component is yet apparent at the lower shot-noise levels. This appears to conflict with the currently developed IHL models, shown in green [from Cooray *et al.* (2012) (short dashes) and Zemcov *et al.* (2014) (long dashes)], where the one-halo component contributes an effective shot noise, which may be related to the large-scale amplitude driven by the two-halo term. The solid blue line shows a high-z ΛCDM template $k^2 P_{3D}(k)$ at $k = q d_A$ with $d_A \sim 7$ Gpc normalized to the CIB fluctuation from Spitzer and corrected for the mask as described by Kashlinsky *et al.* (2012). The PBH model of Kashlinsky (2016) naturally produces the required CIB, has sources located at these distances, and is effectively represented by the solid blue line. The DCBH model of Yue, Ferrara, Salvaterra, Xu, and Chen (2013) is plotted with red triple-dot-dashed lines. Both BH models appear to match the current data since the shot-noise amplitude, being fixed by the abundance of the individual sources and their fluxes, is below the levels reached in these measurements. Adapted from Kashlinsky, Mather *et al.*, 2015.

e. Coherence of new sources between 3.6 and 4.5 μm

Figure 23, derived from the Kashlinsky *et al.* (2012) measurements, shows the coherence between the source-subtracted CIB fluctuations from Spitzer at 3.6 and 4.5 μm.
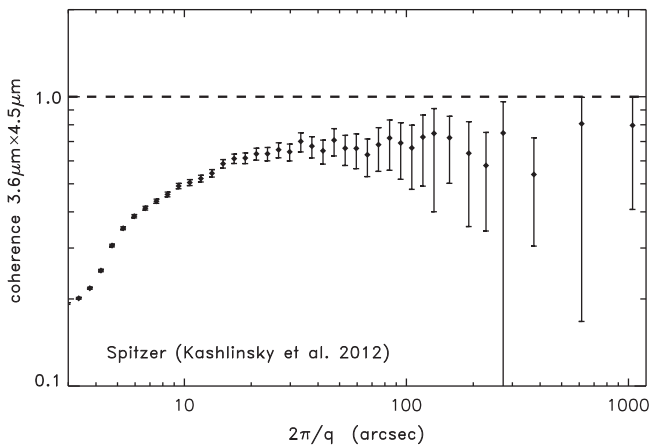

FIG. 23.   Coherence between the CIB at 3.6 and 4.5 μm. Small angular scales show the incoherent contributions due to differentially removed sources at the two bands. Larger scales are dominated by the coherent CIB from new populations. Adapted from Kashlinsky, Mather *et al.*, 2015.

A consistent picture appears of the CIB measurements obtained with Spitzer: (1) the coherence is always bounded from above by unity including the errors, which were evaluated using the Fisher transformation, (2) with small scales dominated by the remaining known galaxy populations, which are independently removed at the two bands and so are less coherent than (3) the large scales, where new populations dominate, which cannot be resolved with Spitzer and, hence, were not yet removed.

f. CIB-CXB cross power

CIB-CXB cross power appears significant between the source-subtracted CIB in the Spitzer measurements and unresolved soft x-ray CXB as illustrated in Fig. 24 with results from Cappelluti, Arendt *et al.* (2017). If the observed arc min scale CIB is produced by sources at the epoch of the first stars, then it arises from sources which would have been coeval with or evolve into, or even be, the first generation of BHs in the Universe. Since BH accretion inevitably produces intense x-ray radiation, one would expect a certain level of coherence between the fluctuations of the two cosmic backgrounds. The coherence uncovered in the measurements can also be interpreted as the fraction of the emission due to the common populations so that $\mathcal{C}_{ij} \approx \zeta_i^2 \zeta_j^2$, where ζ_i and ζ_j are
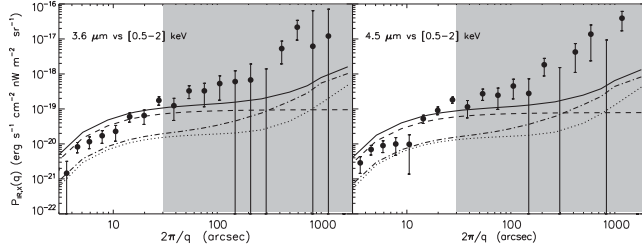
FIG. 24. Cross power between CIB at (left) 3.6 and (right) 4.5 μm and unresolved soft x-ray CXB at [0.5–2] keV is shown with filled circles and 1σ errors. Lines denote contributions from remaining known sources: shot noise (dashes) and clustering component (dot-dashed) from galaxies and AGN, hot gas (dotted), and the total (solid). Shaded regions mark angular scales where clustering components dominate, which is measured to exceed the contributions from known sources for both IR bands at scales $>30''$. From Cappelluti, Arendt *et al.*, 2017.

the fractions of the emissions produced by the common populations between bands i and j. Cappelluti *et al.* (2013) determined the level of coherence between the source-subtracted CIB and CXB and found it of the order of $\mathcal{C}_{\text{CIB-CXB}} \sim 0.05$ at the largest angular scales, so if all the CXB power is produced by sources correlating with the CIB then a lower limit on the CIB fluctuations produced in association with the x-ray sources is 15%–25%. We note that the stated coherence represents a *lower* limit on the true CIB-CXB coherence of the new sources, since the CXB power they contribute is, while observationally unknown, less than the measured power from the diffuse x-ray maps. The level of unresolved CXB around 1 keV is $\lesssim 1$ keV/cm^2/s/sr [see Table III in Cappelluti *et al.* (2017), and Fig. 5], corresponding to comoving number density of the x-ray photons at 1 keV of $n_{\text{CXB}} \lesssim 4 \times 10^{-10}$ cm^{-3}. At the same time the excess CIB of ~ 1 nW/m^2/sr around 3 μm requires comoving density of CIB photons at $n_{\text{CIB}} \sim 6 \times 10^{-4}$ cm^{-3}. Thus the sources producing the two together should have $n_{\text{CXB}}[(1+z)\,\text{keV}]/n_{\text{CIB}}[3/(1+z)\,\mu\text{m}] \lesssim 6.6 \times 10^{-7}$ requiring the X/O ratio [defined as the logarithmic slope from 0.25 μm to 2 keV (Tananbaum *et al.*, 1979)] $\alpha_{OX} \gtrsim 2$.

g. Application of Lyman tomography to Spitzer CIB

The application of Lyman tomography to Spitzer CIB was made by Kashlinsky, Mather *et al.* (2015) with data analyzed in the IRAC configuration of Kashlinsky *et al.* (2012). As Fig. 10 shows the IRAC filters are adjacent and nonoverlapping, presenting a testing ground for the Lyman tomography. The measured CIB powers at the two IRAC channels $P_{3.6}$ and $P_{4.5}$ and the cross power $P_{3.6 \times 4.5}$, shown in Fig. 14, were used to construct per Eq. (14) the excess power component that arises where the Lyman-break populations are present at 4.5 μm, but not at 3.6 μm ($30 \lesssim z \lesssim 40$ assuming the Ly break at these prereionization epochs due to the Ly-α absorption). The CIB data used consisted of two regions of $21' \times 21'$ and $8' \times 62'$ of similar integration depth. The regions have full overlap between 3.6 and 4.5 μm. Figure 25 shows the resultant $P_{\Delta z} = P_{4.5} - P_{3.6 \times 4.5}^2 / P_{3.6}$ with 1σ errors. The slope of the fluctuations is close to that of nonlinear
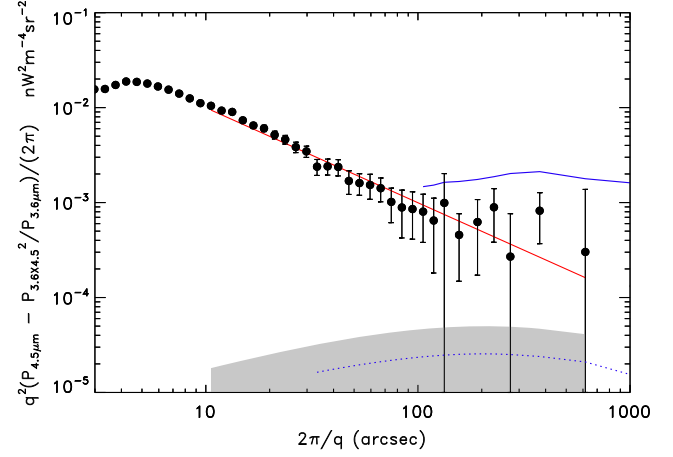

FIG. 25. The Lyman-break based tomography application to the current Spitzer and IRAC measurements of Kashlinsky *et al.* (2012) at 3.6 and 4.5 μm (filled circles). The solid red (straight) line shows the $P \propto q^{-1}$ template that fits the data and is consistent with the nonlinear clustering of known galaxies remaining after differential subtraction at the two bands. The blue line shows the high-z ΛCDM template that fits the CIB fluctuation data at 4.5 μm. The filled region is the 1σ limit on the CIB power remaining for populations at $z > z_{\text{Lyman break}}(4.5 \ \mu\text{m}) \gtrsim 30$ with the dotted blue line showing the central fit. The power left for these populations is $\lesssim 2\%$ of that measured at 4.5 μm. Adapted from Kashlinsky, Mather *et al.*, 2015.

galaxy clustering produced by differentially removed sources at the two IRAC bands. Kashlinsky, Mather *et al.* (2015) decomposed the data shown in the figure into (1) shot noise, (2) nonlinear clustering from remaining differentially removed galaxies at the two IRAC bands, assumed to follow $P \propto q^{-1}$, consistent with the 2MASS CIB measurements, and (3) high-z ΛCDM and evaluate the amplitudes of each component. The solid red line in the figure shows the resultant fit from the nonlinear clustering component. In the presence of the empirically determined remaining galaxy component, the amplitude of the clustering component with the concordance ΛCDM power template at $z \simeq 30$ is shown at its 1σ upper limit. The resultant high-z component is shown in Fig. 25. Its fitted amplitude implies the contribution to the power measured at 4.5 μm in the Spitzer data by Kashlinsky *et al.* (2012) to be at most 2% from $z \gtrsim 30$, setting the best upper limits available to date on emissions from these epochs.

C. Measurements at 1–2 μm

There is significantly less agreement between the various measurements at this wavelength range, and their interpretation is therefore subject to what data set is assumed to represent reality. The measurements have been done in the following chronological order: (1) CIB analysis by Kashlinsky *et al.* (2002) and Odenwald *et al.* (2003) using deep 2MASS data from the ground (Nikolaev *et al.*, 2000) at 1.1, 1.6, and 2.2 μm; (2) a much deeper CIB analysis (Thompson *et al.*, 2007a, 2007b) using space-based HST NICMOS data at 1.1 and 1.6 μm over a smaller region (Thompson *et al.*, 2005); (3) the shallowest of the analyses over a larger area of the

sky (Zemcov *et al.*, 2014) using partially overlapping filters center at 1.1 and 1.6 μm with a suborbital CIBER measurement (Bock *et al.*, 2013); and (4) a deep analysis using the HST Wide Field Camera 3 (WFC3) data by Mitchell-Wynne *et al.* (2015). The four lower panels in Fig. 10 show the filters employed in obtaining the results discussed in this section in chronological order.

1. Deep 2MASS

The 2MASS standard star survey (Nikolaev *et al.*, 2000) was used by Kashlinsky *et al.* (2002) and Odenwald *et al.* (2003) to develop the required methodology and probe for the first time source-subtracted CIB fluctuations. The analysis was done after the assembled field of $\simeq 8.6' \times 1°$ was divided, in order to eliminate artifacts, into seven square patches of $512'' \times 512''$ probing CIB in each patch out to angular scales $2\pi/q \sim 200''$. The resolution was limited by atmospheric seeing at about $2''$. Galaxies have been identified and removed down to the Vega magnitude of $\sim 18.7-20$ (*AB* magnitudes $\sim 20-21$) in the J, H, and K_s photometric bands, with each of the patches clipped to its individual depth. As discussed by Kashlinsky *et al.* (2002) this leaves CIB from galaxies at $z \gtrsim 0.6 - 1$ depending on magnitude and band. The sky fraction removed with the resolved sources was less than 10% allowing a robust CIB FT analysis. After analyzing
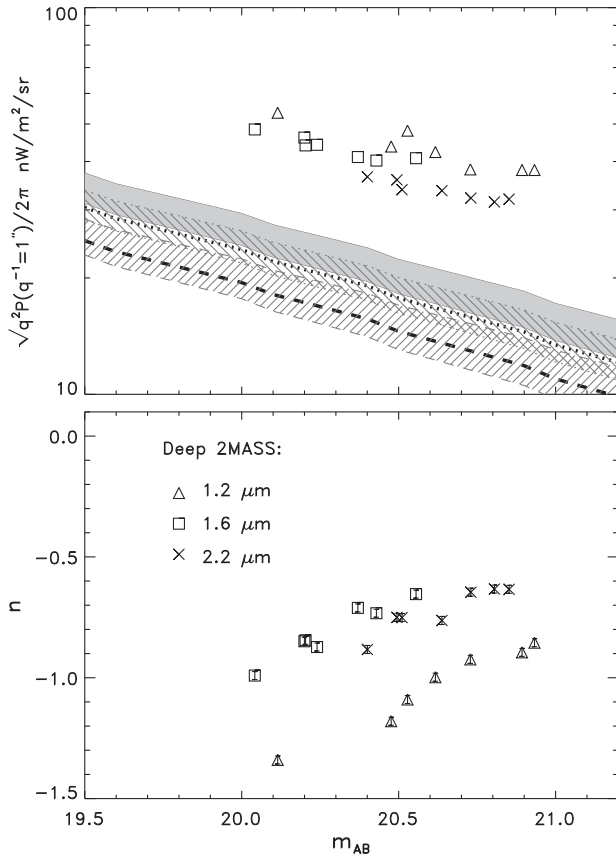

FIG. 26. CIB fluctuations from 2MASS [see data in Fig. 2 of Kashlinsky *et al.* (2002)]. Shaded regions are shot-noise contributions from HRK12 reconstruction from HFE to LFE with the thick central line for the default model (solid—J, dotted—H, and dashed—K).

contributions from atmospheric glow and other foregrounds, CIB fluctuations were claimed with the non-white-noise spatial spectrum produced by (evolving) nonlinear clustering from remaining galaxies with $P \propto q^{-n}$ and the slope varying between $n = 1.4$ for the shallowest removal and $n = 0.6$ for the deepest; for reference the present-day nonlinear clustering has $n \sim 1.3$. Figure 26 shows the amplitude of the resultant source-subtracted CIB fluctuations at the fiducial scale $q^{-1} = 1''$ and the effective deduced slope n in the seven 2MASS CIB patches with sources remaining below the flux corresponding to the *AB* magnitude shown in the horizontal axis.

While it is reported to "identify the signal as CIB fluctuations from the faint unresolved galaxies," there may be possible systematical biases affecting this analysis which may stem from the required in the data destriping corrections, adopted to cover a narrow width of pixels in the Fourier plane, and which in turn affect the conversion of the remaining σ's of the maps to effective magnitudes as discussed by Odenwald *et al.* (2003). In addition, the ground-based observations are significantly affected by the variability of the OH glow. In any event, this study probes the remaining CIB at too shallow a depth (by today's standards) to be useful in probing high-z emissions.

2. HST NICMOS

NICMOS-based source-subtracted CIB fluctuations at 1.1 and 1.6 μm were studied by Thompson *et al.* (2007a, 2007b) after progressively eliminating galaxies down to much fainter fluxes than in 2MASS using data from the NICMOS Ultradeep Field, $\sim 2' \times 2'$ in size (Thompson *et al.*, 2005). After removing identified sources down to the *AB* magnitude of ~ 27.7, 93% of the map remained for robustly direct power spectrum evaluation. The sky maps were at the subarcsecond resolution of HST. Donnerstein (2015) discussed the contributions from the remaining outer parts and found them small. Thompson *et al.* (2007b) showed the Fourier plane of their images to be clean of artifacts from map construction. The resultant CIB fluctuations from that study are plotted with black asterisks in Fig. 27 at various depths of removal. At the magnitude limits corresponding to the depth reached in the 2MASS studies, the NICMOS results do not fully agree with the former study but the difference can be accounted for if one assumes the 2MASS images to be at an effectively brighter removal magnitude due to destriping as discussed. The asterisks in the figure show the diffuse light fluctuations at the ultimate removal threshold. The remaining diffuse light fluctuations appear significantly in excess of those from remaining known galaxies (Helgason, Ricotti, and Kashlinsky, 2012).

Based on the color ratio of the 1.1 to 1.6 μm diffuse fluctuations Thompson *et al.* (2007b) suggested "that the 0.8–1.8 μm near-infrared background is due to resolved galaxies in the redshift range $z < 8$, with the majority of power in the redshift range of 0.5–1.5."

3. CIBER

The CIBER suborbital rocket-borne experiment (Bock *et al.*, 2013; Zemcov *et al.*, 2014) recently suggested CIB fluctuations at 1.1 and 1.6 μm shown in Fig. 28 from Zemcov *et al.* (2014). Its imaging camera probes emissions with $\Delta\lambda/\lambda \simeq 0.5$ around the central wavelengths over a square field of view of 2°
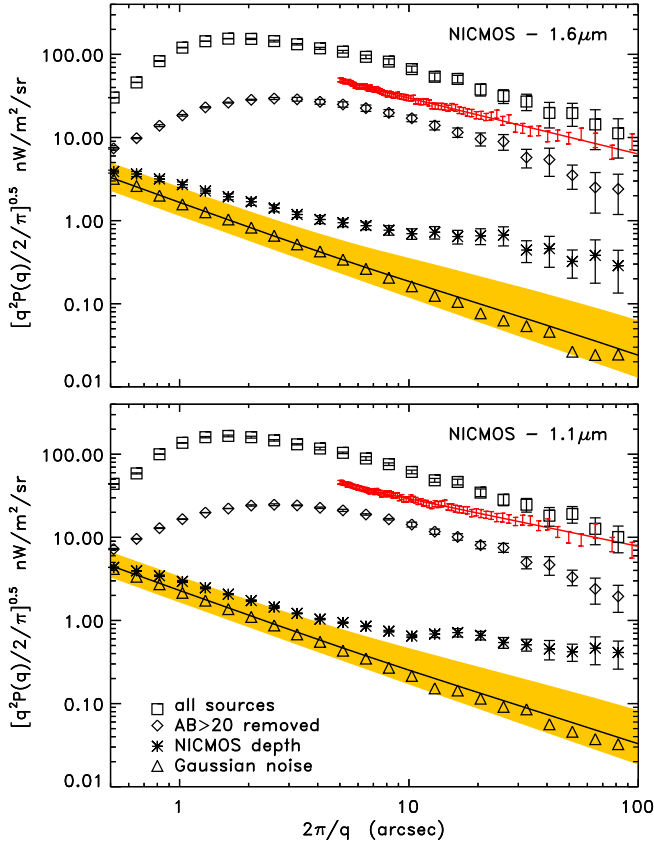
FIG. 27. Root mean square fluctuations from the autopower from the NICMOS analysis (Thompson *et al.*, 2007b) at different magnitude removal thresholds. The squares mark no removal, the diamonds are for removal out to $m_{AB} \simeq 20$, and the asterisks are for the maps cleaned of NICMOS sources to the final depth. The triangles mark the NICMOS noise as estimated by Thompson *et al.* (2007a, 2007b). For comparison the 2MASS-based CIB fluctuations from Kashlinsky *et al.* (2002) and Odenwald *et al.* (2003) are shown as red error bars without symbols. The CIB fluctuations from galaxies remaining at the greatest NICMOS depth are shown in yellow shading using the HRK12 reconstruction. Adapted from Thompson *et al.*, 2007a, 2007b.

on the side with ∼6″ pixels. After removing galaxies to the Vega magnitude of 17.5 at the *J* band (about 3 magnitudes brighter than deep 2MASS), and construction of maps that are the difference of separate fields (to remove common instrumental artifacts), only 30%–50% of the sky is left for Fourier analysis on the CIBER maps; see, e.g., Figs. S4–S7 of Zemcov *et al.* (2014). After rejecting some of the data due to the stratospheric air glow, four fields observed over two flights formed the basis for the analysis.

Their key assertions are that (1) "The observed fluctuations exceed the amplitude from known galaxy populations," (2) since they do not fit the epoch-of-reionization modeling of Cooray *et al.* (2012) they "are inconsistent with EoR galaxies and black holes," and (3) "are largely explained by IHL emission" without accounting for the remaining difference between the measurement and the IHL model.

Although the masking approaches 70% of the pixels in this study, the correlation function has not been evaluated to substantiate the robustness of the claimed power spectra.
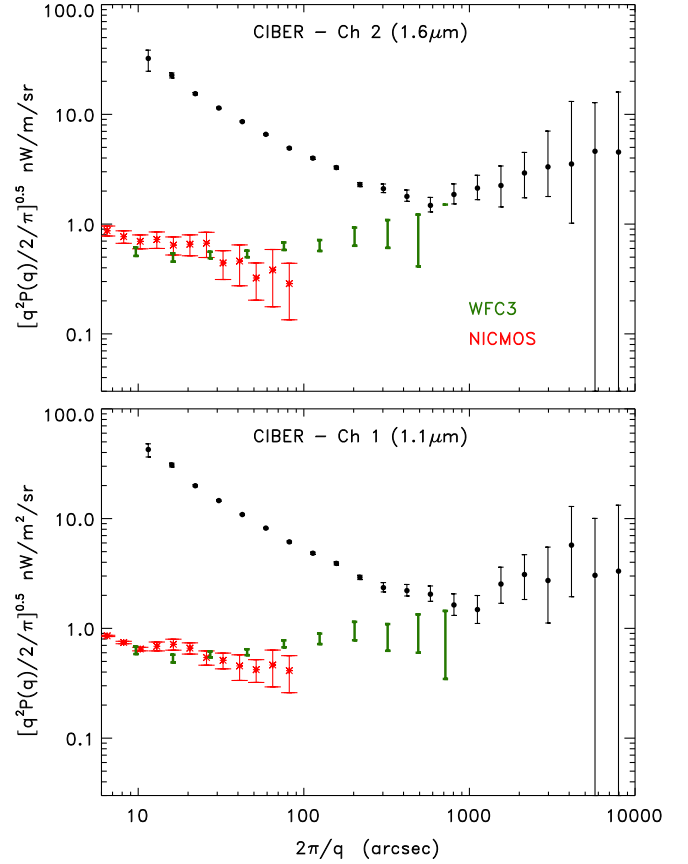
FIG. 28. Mean squared fluctuations from the autopower from the CIBER analysis (Zemcov *et al.*, 2014). For comparison the NICMOS (Thompson *et al.*, 2007b) (red stars) and WFC3 (Mitchell-Wynne *et al.*, 2015) (green error bars without symbols) HST-based results are also shown.

Various potential issues with the analysis have been discussed by Kashlinsky, Mather *et al.* (2015) (Sec. 2.1.2), which are impossible to further assess in the absence of explicit calculation of the correlation function for the heavily masked maps. Yue, Ferrara, and Salvaterra (2016) questioned the extragalactic origin of the claimed CIBER-Spitzer cross power assigning it to the Galactic cirrus instead.

4. HST WFC3

Mitchell-Wynne *et al.* (2015) looked at diffuse background fluctuations in deep HST and WFC3 (and ACS) observations of the CDFS. They applied the self-calibration procedure of Arendt *et al.* (2010) to construct 120 arcmin² maps at 1.25 and 1.6 μm. After masking 47% of the maps, they use the same methodology for computing the power spectrum from FTs as in Zemcov *et al.* (2014); despite the highly substantial masking their correlation function is not shown. Using the assembled WFC3-based images in conjunction with ACS and IRAC data they fit a multicomponent model assuming (1) the existence of IHL with the template from Cooray *et al.* (2012), in addition to (2) remaining known galaxies modeled after Helgason, Ricotti, and Kashlinsky (2012), (3) diffuse Galactic cirrus emission, and (4) a high-*z* component from Cooray, Gong *et al.* (2012). Assuming these components they concluded that the HST-based CIB fluctuations at 1.1 and 1.6 μm
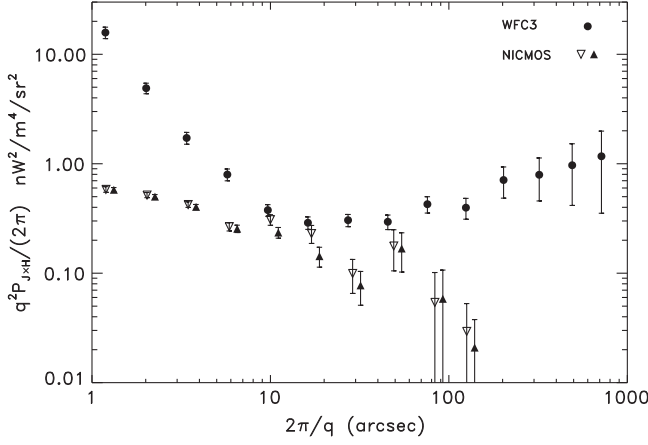
FIG. 29. The black circles show the 1.25×1.6 μm cross power from WFC3 (Mitchell-Wynne *et al.*, 2016). The triangles are the 1.1×1.6 μm cross power evaluated for this review from NIC-MOS maps: the upward triangles are for the "Thompson mask," and the downward triangles are for the extended mask; the two are slightly shifted for easy display.

contain high-z emissions at the luminosity density a factor of $\sim(2–3)$ lower than derived earlier in Kashlinsky *et al.* (2007c) at 3.6 and 4.5 μm from Spitzer CIB measurements. They also obtained with this fit modeling a cirrus level "at least a factor of 3 larger than the upper limit" from CIBER.

The source-subtracted CIB fluctuations from that study at 1.1 and 1.6 μm are shown in green in Fig. 28 and can be interpreted as being in reasonable agreement with the findings of Thompson *et al.* (2007a, 2007b). However, a significant disagreement emerges at both small and large scales when one evaluates the cross power between the two wavelength maps for the NICMOS images from Thompson *et al.* (2007a, 2007b) and that from Mitchell-Wynne *et al.* (2015) as shown in Fig. 29. Thompson *et al.* (2007a, 2007b) did not evaluate this cross power, but the archival images (intensity, sigma, and SExtractor detections) are available.[1] We downloaded the 1.1 and 1.6 μm images, rotated and cropped them, and applied appropriate conversions to νI_ν in nW/m^2/sr. No model is applied to remove sources. Masking the sources using the regions indicated by the SExtractor detection image yields a mask that is similar to, but not exactly the same as, the masking illustrated by Thompson *et al.* (2007a, 2007b). This mask excludes 10% of the data, slightly larger than the stated 7% exclusion. We also tested a more conservative mask analogous to Donnerstein (2015), in which we expanded the masked regions by a radius of 7.5 pixels (0.675″), which leads to excising 31% of the data. The cross power does not require noise subtraction if the noise at the two channels is uncorrelated. There appear significant differences in the cross power of the NICMOS and WFC3-based data sets. Additionally, the autopower and cross power for the Mitchell-Wynne *et al.* (2015) results appear to lead to coherence exceeding unity at both small and large scales. It is not clear what HST data set and diffuse maps better approximate reality.

5. Current state of CIB fluctuations at 1–2 μm

Unlike in the 2–5 μm range, there appears no mutually agreed upon CIB fluctuation results at 1–2 μm, preventing any robust cosmological modeling. This will be reflected in our next discussions, although whenever it makes sense we will make brief, if more speculative, excursions into this range of wavelengths.

D. Integrated CIB excess

The measured CIB fluctuation excess at 2–5 μm appears to have only small (within the uncertainties) variations between $\sim 1'$ and $\sim 1°$. The power spectrum of such CIB fluctuations from the new populations can be characterized with an amplitude at some fiducial scale and a template. The CIB fluctuations, at say $\sim 5'$ which was used for such normalization in Kashlinsky *et al.* (2012), as measured with Spitzer and AKARI can be integrated to give the net CIB flux fluctuations over the wavelengths of the detections leading to

$$
\begin{aligned}
\delta F_{2\text{–}5\ \mu\text{m}}(5') &= \int_{\text{AKARI}}^{\text{IRAC}} \left(\frac{q^2 P_\lambda}{2\pi}\right)^{1/2} \frac{d\lambda}{\lambda} \\
&= \left[\frac{(4.5/2.4)^\alpha - 1}{\alpha}\right] \delta F_{4.5\ \mu\text{m}}(5') \simeq 0.09\ \frac{\text{nW}}{\text{m}^2\ \text{sr}},
\end{aligned}
\tag{16}
$$

where $\nu\delta I_\nu \equiv [q^2 P_\lambda/2\pi]^{1/2}$ is the CIB flux fluctuation in nW m^{-2} sr^{-1} and we assume per Fig. 21 that it scales with wavelength as $\nu\delta I_\nu \propto \lambda^{-\alpha}$ with $\alpha \simeq 3$; for $\alpha = 2$ Eq. (16) gives $\delta F_{2\text{–}5\ \mu\text{m}} \simeq 0.065$ nW m^{-2} sr^{-1}. In Eq. (16) we have taken the AKARI and Spitzer-IRAC filters to have the integrated range of 2–5 μm and the "nominal" central values of the filters were plugged into the middle expression.

Assigning the relative amplitude of a CIB fluctuation for a given template at the fiducial scale of, say $5'$, $\Delta_{5'} \equiv \delta F_{2\text{–}5\mu\text{m}}(5')/ F_{2\text{–}5\mu\text{m}}$ would require the new populations to produce a net integrated CIB flux of $F_{2\text{–}5\mu\text{m}} = \delta F_{2\text{–}5\mu\text{m}}(5')/\Delta_{5'} \sim 1 \text{nW/m}^2/\text{sr}$ for $\Delta_{5'} \sim 10\%$. If its λ^{-3} SED extends to 1.6 μm, the integrated CIB fluctuation excess from the new populations would be higher at $\delta F(5') \sim 0.3$ nW m^{-2} sr^{-1} over the 1.6–5 μm range leading to $F_{1.6\text{–}5\ \mu\text{m}} \lesssim 3$ nW m^{-2} sr^{-1} still within the errors of the current conservative CIB measurements of Thompson *et al.* (2007a, 2007b). Conversely, if the λ^{-3} SED of the CIB excess observed with Spitzer does not extend to the shortest AKARI 2.4 μm channel, the required CIB would be correspondingly smaller.

VI. IMPLICATIONS OF CIB FLUCTUATION RESULTS

A. General implications

The general implications of the source-subtracted CIB fluctuations stem from (1) the properties of the clustering, in shape and amplitude, that appear (2) at very low shot-noise power levels (Kashlinsky *et al.*, 2007c).

As discussed in Sec. IV.A.1, the shot-noise power is $P_{\text{SN}} \simeq S_\nu(\bar{m}) F_{\text{tot}}(> m_{\text{lim}})$, where $F_{\text{tot}}(> m_{\text{lim}})$ is the CIB flux from remaining sources. The measured levels of the shot noise do not currently reach the regime of attenuation of the

large-scale fluctuation from clustering; the point where this happens would then probe the flux of the typical sources responsible for this CIB component. The deepest current limits reached are $P_{SN} = (26, 14)$ nJy nW m^{-2} sr^{-1} at $(3.6, 4.5)$ μm. Since $P_{SN} \sim SF_{tot}$, these limits, imply the upper limits on the typical fluxes of the sources producing them:

$$S_{(3.6, 4.5)\ \mu m} \gtrsim (26,\ 14) \left(\frac{F_{tot}}{nW/m^2/sr} \right)^{-1} nJy. \quad (17)$$

Such objects would have $m_{AB} \gtrsim$ 28–29 and may have fluxes well below what can be probed individually even with the JWST.

A *lower* limit on the projected surface density n_2 of the new sources can be estimated in a similar manner by writing the shot-noise power from these sources as $P_{SN} \sim F_{CIB}^2 / n_2$. The measured shot noise at $P_{SN} \sim 10^{-11}$ nW^2/m^4/sr (Kashlinsky *et al.*, 2007b) gives an *upper* limit on the shot noise from the new populations, so their number per beam of area ω, $\mathcal{N}_2$, must exceed

$$\mathcal{N}_2 \gtrsim 0.1 \left(\frac{F_{CIB}}{nW/m^2/sr} \right)^2 \left(\frac{P_{SN}}{10^{-11}\ nW^2/m^4/sr} \right)^{-1} \frac{\omega}{10^{-12}\ sr}. \quad (18)$$

Confusion intervenes when there are more than 0.02 sources/ beam (Condon, 1974), so this shows that the bulk, perhaps all, of the new populations would be within the confusion noise of the instruments with beams of $\omega \gtrsim 2 \times 10^{-13}$ sr or effective radii $\gtrsim 0.05''$. Note that the shot noise in the current measurements is produced by the remaining known galaxies and the component contributed by the new sources may be much smaller leading to still stronger constraints from confusion.

B. Known populations

It is now generally agreed that known populations appear insufficient to explain the source-subtracted CIB signal measured at 2–5 μm. Its origin is then posited to lie in new sources, at either high z or more recent epochs. It was also shown that even extrapolating from the measured UV LFs (Bouwens *et al.*, 2011) of the known galaxy and stellar populations to higher z does not explain the CIB (Cooray, Gong *et al.*, 2012; Yue, Ferrara, Salvaterra, and Chen, 2013), although latter studies of high-z UV LFs (Finkelstein *et al.*, 2015) may ease the degree of the disparity somewhat.

C. High-z sources

The bolometric flux produced by populations containing a fraction f of the baryons in the Universe after they have converted their mass energy into radiation with efficiency ϵ at an effective redshift $z_{eff} \equiv 1/\langle (1+z)^{-1} \rangle$ is given by Eq. (4). Populations at high z are strongly biased, span a short period of cosmic time, and are expected to produce $\Delta_{5'} \sim 10\%$ relative CIB fluctuations around a 5′ scale. Such populations would then require producing about $F_{CIB} \sim 1$ nW m^{-2} sr^{-1} in the integrated flux at near-IR wavelengths $(2 - 5\ \mu m)$ implying a correspondingly large luminosity density around rest frame UV at $z \gtrsim 10$ as argued by Kashlinsky *et al.* (2007c).

Mitchell-Wynne *et al.* (2015) derived similar numbers from an assumed multicomponent fit, including IHL and high-z sources, to deep Spitzer and HST data. The overall fraction of the Universe's baryons needed to explain the CIB is $f_{Halo} f_*$ [see Sec. 2.3.2 in Kashlinsky, Mather *et al.* (2015)]. Massive stars can convert matter into radiation with an efficiency of $\epsilon \simeq 0.007$, whereas accretion onto BHs can reach $\epsilon \lesssim 0.4$. If the integrated CIB fluctuation approximates the bolometric flux produced by these sources, the mean fraction of baryons that go into the sources inside each halo is

$$f_* = 0.1 \left(\frac{f_{Halo}}{0.01} \right)^{-1} \left(\frac{\epsilon}{0.01} \right)^{-1} \left(\frac{z_{eff}}{10} \right) \left(\frac{\Delta_{5'}}{0.1} \right)^{-1} \left(\frac{F_{tot}}{nW/m^2/sr} \right)$$
$$\times \left[\frac{F_{CIB}(2-5\ \mu m)}{F_{tot}} \right]. \quad (19)$$

Thus in order to produce the measured CIB at $z > 10$ with "reasonable" formation efficiencies ($f_* < 10\%$) one requires a large fraction of matter in collapsed halos capable of producing luminous sources.

1. First stars

Potential CIB contributions from first stars have been discussed by various authors assuming both predominantly massive Pop III stars (Santos, Bromm, and Kamionkowski, 2002; Salvaterra and Ferrara, 2003; Cooray *et al.*, 2004; Kashlinsky *et al.*, 2004; Kashlinsky, Mather *et al.*, 2015) as well as mixed stellar mass functions which include also normal mass stars at high z (Fernandez *et al.*, 2010, 2012; Helgason *et al.*, 2016).

Helgason *et al.* (2016) conducted an extensive study of the contribution to CIB expected from early stellar populations in standard ΛCDM cosmology and Fig. 30 summarizes their results for stellar contributions. The fraction of halos f_{Halo} collapsing at given z according to several variants of the Press and Schechter (1974) prescription is shown in the upper panel of the figure. Then one can evaluate the net CIB assuming stars of a given stellar mass-function form in the collapsed halos with mean efficiency f_*. Four stellar mass functions were considered: (1) IMF$_1$ with a standard Kroupa mass function in the $(0.1–100)M_\odot$ range, (2) IMF$_{10}$ with log-normal mass function with characteristic mass of $10M_\odot$ and dispersion of $1M_\odot$ in the $(1–500)M_\odot$ range, (3) IMF$_{100}$ with Salpeter-type power law $\propto M^{-2.35}$ in the $(50–500)M_\odot$ range, and (4) IMF$_{500}$ with all stars having $500M_\odot$ emitting in the near-Eddington fashion. All stars were assumed to evolve from single zero-age main sequence objects, using calculations of luminosity and spectra computed from the population synthesis code of Zackrisson *et al.* (2011). The resultant mean efficiency f_* required to explain the observed CIB fluctuations at 2–5 μm within the standard ΛCDM density field (Fig. 1) appears high as shown in the lower panel of Fig. 30.

Helgason *et al.* (2016) further discussed the requirements of high-z sources to produce the observed CIB fluctuations within the conventional, if necessarily simplified, framework of gravitational clustering and spherical collapse of adiabatic ΛCDM fluctuations. They concluded that (1) first galaxies if extrapolated to $z > 8$ from known UV luminosity functions
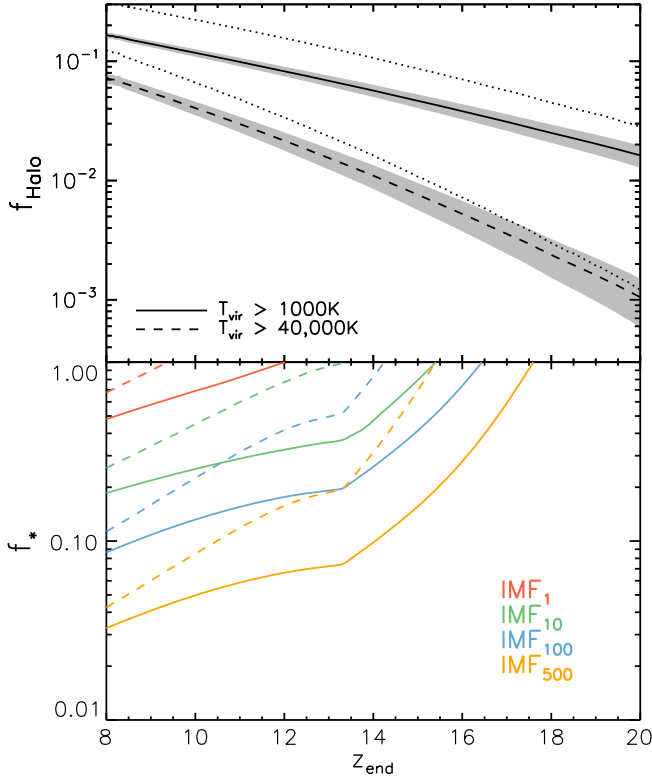
FIG. 30. Top: The mass fraction in collapsed halos as a function of redshift. Solid and dashed lines correspond to halos with different T_{vir} as marked. Dotted lines show the classic Press and Schechter (1974) prediction compared with solid lines for the variant of Sheth and Tormen (2002). Note that the classic Press-Schechter prescription underestimates the abundance of the most extreme objects. Additional complication may arise through UV radiation from first sources, supernova blast waves, and chemical enrichment of the ambient gas. Bottom: The star formation efficiency f_* required to produce the CIB fluctuations by a given redshift z_{end}. The curves assume the entire stellar population forming with IMF_1, IMF_{10}, IMF_{100}, and IMF_{500} (red, green, blue, orange, top to bottom) in all halos. The solid lines show the cases where minihalos $T_{vir} > 1000$ K are included, whereas the dashed lines include $T_{vir} > 40\,000$ K halos only. Adapted from Helgason *et al.*, 2016.

would produce much less CIB fluctuation power than observed (Cooray, Gong *et al.*, 2012; Yue, Ferrara, Salvaterra, Xu, and Chen, 2013), and (2) at still higher z (first) stars would have to (i) form inside the collapsed halos at substantial formation efficiencies (converting $f_* \gtrsim 5\%$ of the available baryons in collapsing halos) and (ii) be very massive ($\sim 500 M_\odot$) if they are to explain by themselves the observed CIB anisotropies. Kashlinsky, Arendt *et al.* (2015) reproduced the observed Spitzer signal with massive early stars forming at the mean formation efficiency $f_* \simeq 4\%$ out to $z = 10$.

The "high-mean-formation-efficiency" difficulty can ultimately be traced to a relative paucity of high-z collapsed halos, with the parameters considered appropriate for star formation, due to the limited amount of power set by the adiabatic ΛCDM component of matter fluctuations, which arose from the period of inflation. Later we discuss how the abundance of the halos collapsed at high z is dramatically increased if PBHs constitute

the DM, and reduce, by large factors, the efficiencies required to produce the observed CIB anisotropies.

We note that various natural evolutionary modes of first stars, e.g., enhanced binary formation in turn leading to high-mass x-ray binaries (Mirabel *et al.*, 2011), would reduce the required efficiency f_*, easing the energetics requirements for producing the observed CIB excess.

2. Direct collapse black holes

The motivation to consider first black holes as CIB sources is twofold: (a) the power from even the faintest reionization sources appears to be insufficient, and (b) the CIB-CXB correlation implies the presence of a substantial population of accreting sources. In addition, DCBH ($M_{DCBH} = 10^{4-6} M_\odot$) seeds can ease the already mentioned problem of explaining the inferred masses of supermassive BHs. It is then appealing to consider high-z accreting DCBHs as additional CIB sources. Such faint "AGN" have so far escaped detection from even the deepest x-ray observations (Willott, 2011; Cowie, Barger, and Hasinger, 2012) at any stage during their growth. Whereas deep x-ray surveys do not cover enough volume at high redshift, current wide-area studies are simply not deep enough [$L_X > 10^{42.75}$ erg s^{-1} (Fiore *et al.*, 2012)]. A possible exception is the discovery of two $z > 6$ DCBHs claimed by Pacucci *et al.* (2016), which has raised considerable hope to firmly identify these supermassive BH ancestors.

CIB fluctuations may also arise from DCBHs providing a viable alternative to discover them. The original proposal of this was made by Yue, Ferrara, Salvaterra, Xu, and Chen (2013) and Yue *et al.* (2014) who showed that under some conditions a high-z DCBH population could explain the observed CIB fluctuations, and, most importantly, also the observed CIB-CXB coherence. The spectrum of accreting black holes formed through the direct collapse of metal-free gas in halos with virial temperature $>10^4$ K is likely to be Compton thick. This fact has several important implications: (a) as most of the photons with energy >13.6 eV are absorbed by the large column density of surrounding gas, the contribution of these objects to reionization is negligible; (b) for the same reason, the DCBH contribution to the CXB is reduced significantly; (c) ionizing photons are reprocessed into optical-UV bands (free-free, free-bound, and two-photon emission) while Ly-α photons are trapped, and finally converted into two-photon emission. These secondary photons eventually escape the object and considerably boost (by a factor of 10) the contribution of these sources to the CIB fluctuations.

According to Yue, Ferrara, Salvaterra, Xu, and Chen (2013) predictions, fitting the latest Spitzer observations at 3.6 and 4.5 μm, the observed CIB fluctuations at $\theta > 100''$ can be explained (Fig. 31) by DCBHs formed in metal-free halos with virial temperature $T_{vir} = (1-5) \times 10^4$ K earlier than $z \simeq 12.5$. These DCBHs are formed with initial masses of the order of $10^{5.8} M_\odot$, and subsequently were able to grow by accreting gas at the Eddington limit for about 30–50 Myr.

A population of DCBHs with these characteristics would produce a CXB intensity at 1.5 keV that is well below the current observational limits as long as the obscuring gas column density exceeds $N_H \simeq 10^{25}$ cm^{-2}. Analogously,
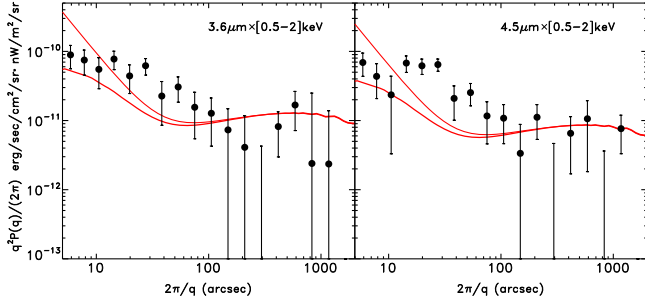
FIG. 31. Mean squared fluctuation spectrum for the CIB-CXB$_{0.5–2.0\,\text{keV}}$ cross power at 3.6 and 4.5 μm (Cappelluti, Arendt *et al.*, 2017). The predicted signal from DCBHs is shown with thin red lines for $N_H \simeq 1.5 \times 10^{25}$ cm^{-2} as revised from Yue, Ferrara, Salvaterra, Xu, and Chen (2013) with modifications for N_H (B. Yue 2017, private communication). The thick red lines show convolution with the IRAC beam of the underlying DCBH model.

DCBHs contribute only marginally to the CXB angular power spectrum. However, the DCBH signal emerges in the CXB-CIB cross correlation at scales >100″. For $N_H = 1.5 \times 10^{25}$ cm^{-2} the cross-correlation level of the DCBH population is $\simeq 8 \times 10^{-12}$ erg s^{-1} cm^{-2} nW m^{-2} sr^{-1}, in tantalizing agreement with recent observations (Cappelluti *et al.*, 2013), despite the remaining large uncertainties in current data.

Thus, the near-IR CIB fluctuations and their coherence with the CXB might be the smoking gun of a peculiar population of early intermediate mass BHs; they might also shed light on the challenging questions posed by the rapid formation of SMBHs seen in quasars.

3. Primordial black holes

Following the original LIGO discovery of GW150914 from two $\sim 30 M_\odot$ coalescing BHs (Abbott *et al.*, 2016a, 2016e) and a tentative detection of another similar object, LVT151012 (Abbott *et al.*, 2016b, 2016c), two more GW events were announced from a total of $\sim$6–7 weeks of advanced LIGO operations: GW151226 (Abbott *et al.*, 2016d) and GW170104 (Abbott *et al.*, 2017), where there appears a marginal evidence for misaligned spins [see discussion in Farr *et al.* (2017)] while no electromagnetic emissions were detected. With the current total of 8–10 BHs,[2] this indicates the presence of BHs with masses peaking near $M_{BH} \sim (20–30) M_\odot$. While the pre-LIGO detection expectations were that the dominant source of detectable GWs would be binary-neutron-star mergers (Abadie *et al.*, 2010), by now a growing population of BHs within the above mass range, while subject to LIGO-specific selection effects, appears to dominate the GW emitting sources.[3] If these BHs are primordial making up or dominating DM, the extra Poissonian component of the density fluctuations would lead to much greater rates of

collapse at early times, which would naturally produce the observed levels of the CIB fluctuations (Kashlinsky, 2016).

As discussed earlier, the DM from PBHs will contain an extra (isocurvature) component due to Poissonian fluctuations (Meszaros, 1974, 1975) with the power component at the time of the PBH formation being $P_{PBH,initial} = n_{PBH}^{-1}$ in comoving units. From their formation to today ($z = 0$) these isocurvature fluctuations would grow, at wavelengths below the horizon at matter-radiation equality z_{eq}, by a scale-independent factor of $(3/2)(1 + z_{eq})$, so the extra power component at redshift z is given by (Afshordi, McDonald, and Spergel, 2003; Kashlinsky, 2016)

$$P_{PBH}(z) = \frac{9}{4}(1 + z_{eq})^2 n_{PBH}^{-1} [g(z)]^{-2}$$

$$\simeq 2 \times 10^{-2} \left(\frac{M_{PBH}}{30 M_\odot}\right) \left(\frac{\Omega_{CDM} h^2}{0.13}\right) g^{-2}(z) \text{ Mpc}^3, \quad (20)$$

where $g(z)$ is the linear growth factor of fluctuations from z to today, with $g(0) = 1$. We assumed all PBHs to have identical mass of $30 M_\odot$; the discussion can be trivially generalized to any PBH mass distribution with a suitably averaged effective M_{PBH}. Figure 32, left, shows the extra power component for $M_{PBH} = 30 M_\odot$ compared to the ΛCDM power spectrum from the purely adiabatic fluctuation component. The power is plotted versus the mass contained in wavelength $2\pi/k$ which is $M(r) = 1.15 \times 10^{12} (r/1 \text{ Mpc})^3 M_\odot$ for the adopted cosmological parameters. This extra power is $\propto M_{PBH}$ and for $M_{PBH} > 1 M_\odot$ dominates the small scales relevant for collapse of the first halos at $z > 10$, but has no impact on the observed
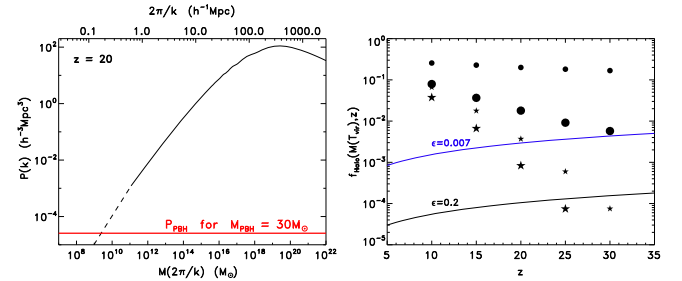

FIG. 32. Left: The solid black line marks the CMBFAST-computed ΛCDM power spectrum at $z = 20$ vs the mass within the comoving radius $2\pi/k$. Black dashes show the $P_{\Lambda CDM} \propto k^{-3}$ extrapolation to scales not accessible to CMBFAST, but relevant for first halos collapse. The horizontal solid red line is the Poissonian power from DM PBHs of $M_{PBH} = 30 M_\odot$, which clearly dominates the scales relevant for halo collapse at this z; $P_{PBH} \propto M_{PBH}$, with M_{PBH} being a suitably averaged mass in case of PBH mass distribution. Right: Fraction of collapsed halos at $T_{vir} > 10^3$ K vs z for standard ΛCDM power spectrum (small stars) and $M_{PBH} = 30 M_\odot$ (small circles); the same for $T_{vir} > 10^4$ K shown with large stars and circles. The thick solid lines mark the overall fraction of baryons $f_{Halo} f_*$ needed to produce the observed CIB with the H-burning radiative efficiency $\epsilon = 0.007$ (blue) and BH-type efficiency $\epsilon = 0.2$ (black). The required mean baryon conversion efficiency into luminous sources inside each halo f_* is the ratio of the solid curves to the symbols. f_*, while high otherwise, is very modest if the PBHs make up DM. Adapted from Kashlinsky, 2016.

---

[2]A further GW from two merging BHs of $\sim 20 M_\odot$ and $30 M_\odot$ was announced toward the completion of the aLIGO O2 run (Abbott *et al.*, 2017) after this review was prepared.

[3]http://www.virgo-gw.eu/docs/GW170814/BHmassChartGW092017.jpg.

CMB anisotropies or BAOs (Eisenstein and Hu, 1999) which appear in CIB fluctuations on arcmin scales. Moreover, unlike the clustering component, white noise power contributions to the angular CIB power spectrum are not affected by biasing amplification (Kashlinsky *et al.*, 2004). This shows that there is a dramatic increase in power from the Poissonian PBH component, normalized to the LIGO results, on scales relevant to first halo collapse.

The higher abundance of collapsed halos in which first sources would form at $z > 10$ for the PBH DM case is shown in Fig. 32 (right) for (1) minihalos where H_2 formation is efficient evolve at $T \lesssim 10^3$ K and (2) where, in the absence of H_2, the metal-free gas will be able to cool to 10^4 K and collapse in halos with larger virial temperature will proceed isothermally. In this case luminous sources within the much more abundant early collapsed halos would reproduce the observed Spitzer and AKARI CIB fluctuations with modest formation efficiency requirements. This can be demonstrated by taking population models from Helgason *et al.* (2016) and rescaling them by the collapse-efficiency ratio from Fig. 32, right. Specifically, Spitzer-based CIB fluctuations would now be reproduced with only $f_* < 0.5\%$ forming out to $z \gtrsim 15$ (instead of 4% with formation continuing to $z \simeq 10$) and the lines in Fig. 5 of Helgason *et al.* (2016) need to be rescaled down by the corresponding factors. Additionally the measured CIB-CXB coherence (Cappelluti *et al.*, 2013) would require that at least $\gtrsim (10–15)\%$ of the luminous CIB-producing sources are accreting BHs, broadly consistent with this scenario. The blackbody temperature of the emissions arising from the Eddington-accreting BHs is $T_{\rm acc} \propto M_{\rm BH}^{-1/4}$ (Kazanas, 2015), so PBHs being much less massive than DCBHs may have a CXB component extending to harder x-ray energies.

Gas collapse and evolution in the PBH minihalos may affect the subsequent emitting source formation inside them as outlined in Sec. IV.D.3.b. The possibility, discussed by Yue, Ferrara, Salvaterra, and Chen (2013) for the DCBH model, whereby the gaseous collapsed halos are Compton thick so the ionizing photons are absorbed and reprocessed into a two-photon continuum, may also apply here.

The arguments are valid only if the PBHs make up all, or at least most, of DM, but at the same time the mechanism appears inevitable if DM is made of PBHs. Upcoming extensive aLIGO observing runs, O3 and beyond, planned to start after increasing sensitivity (Abbott *et al.*, 2016f), and combined with aVIRGO,[4] should be critical in testing this proposition.

D. New intermediate and low-z sources

1. Intrahalo light

The fits to CIB fluctuations at 3.6 and 4.5 μm according to the original IHL model from Cooray *et al.* (2012) are shown by short green dashes in Fig. 22. The revised model fits from Zemcov *et al.* (2014) are shown with long green dashes in the figure; in that most recent form, IHL arises mostly at $z < 0.5$. While the model can be said to reasonably fit the CIB

fluctuations at the highest shot noise, in its presented forms the IHL fails to account for the data at deeper shot-noise levels, available before the introduction of the model, and it remains to be seen whether satisfactory fits to the available data can be constructed by its proponents. In addition, there remain a number of observational and theoretical challenges which make the IHL interpretation problematic. All tests that have been conducted so far have failed to reveal any spatial correlation between the fluctuation signal and extended emission from detected galaxies. If the IHL were to arise from stars originally formed within galaxies, the unresolved fluctuations should produce a measurable spatial correlation with the spatial distribution of resolved galaxies. The apparent absence of such correlations with (i) the subtracted outer parts of galaxies, (ii) artificial halos placed around galaxies, and (iii) the insensitivity to the increased area of source masking all present challenges for the IHL model. These observational tests are described in detail by Arendt *et al.* (2010) and Donnerstein (2015). The IHL also does not account for the measured correlation with the soft x-ray background (Helgason *et al.*, 2014; Mitchell-Wynne *et al.*, 2016; Cappelluti, Arendt *et al.*, 2017).

2. Axion decay

Gong *et al.* (2016) proposed that axions with a mass ∼4 eV decay via two γ's with wavelengths in the near-IR band and in the process leave a signature in the EBL power spectrum over the 0.6–1.6 μm range in agreement with data. It is not clear, however, how the measured high coherence levels between the near-IR CIB and unresolved soft x-ray CXB can be explained in this model.

E. Limitations of current instrumental configurations

Current observations of source-subtracted CIB fluctuations, at 2–5 μm, as discussed suggest the existence of important new cosmological populations, and their coherence with unresolved CXB fluctuations implies that in part they include BHs. It is important to identify the nature and the epochs of these sources and their influence on the contemporaneous high-z universe. We identify here these goals, the limitations of the current surveys in their regard, and the observational capabilities required to resolve them.

1. Directly probing the epochs from Lyman cutoff

Directly probing the epochs from Lyman cutoff is critical to understanding the origin of the new populations responsible for the clustering component of the CIB fluctuations. This can be probed by the implied absence of emissions below the Lyman cutoff which corresponds to the rest Ly-α line in the presence of H I (prior to full reionization). This cutoff around $0.1(1 + z)$ μm provides a critical marker of the epochs when the CIB originated; at $z \simeq 10$ this corresponds to an observer wavelength of ∼1 μm. Determining the epochs of the CIB fluctuation sources requires availability of both visible and near-IR exposures to sufficiently large depths ($m_{AB} \gtrsim 24$) ideally on the same instrument. Figure 33 shows with hashed regions the reconstructed CIB fluctuation levels, with their systematic uncertainties, from galaxies remaining in the
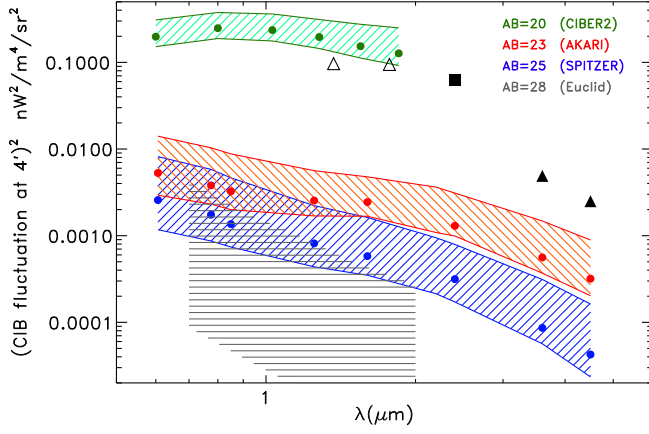

FIG. 33. CIB fluctuations at $2\pi/q = 4'$ vs λ from known galaxies remaining at marked depths (colored bands top to bottom as per legend) are compared to the measured CIB fluctuations at 3.6 and 4.5 μm (Kashlinsky *et al.*, 2012; Kashlinsky, Mather *et al.*, 2015, filled triangles) and 2.4 μm (Matsumoto *et al.*, 2011, filled square). Open triangles show an example of $z > 10$ contribution at J and H bands, which reproduces Spitzer data (Kashlinsky, Arendt *et al.*, 2015; Helgason *et al.*, 2016, see the caption to Fig. 34); it has no emissions below $\simeq 1.1$ μm. Filled circles mark the default HRK12 reconstruction and dashed areas mark the limits due to the HFE and LFE extrapolation extremes. The fiducial scale of $4'$ is shown since the fluctuations at larger scales are approximately constant until $\sim 20'-30'$ where they approach the HZ regime $P \propto q$. Adapted from Kashlinsky, Mather *et al.*, 2015.

currently available and shortly upcoming experimental configurations with their depth and wavelengths accessibility related to this: CIBER2 (Lanz *et al.*, 2014, green), AKARI and HST (red), Spitzer and HST (blue), and the Euclid-based configuration detailed in Sec. VII. The CIB fluctuation signal is illustrated with the amplitudes at $4'$ where the source-subtracted CIB fluctuation is theoretically expected to be near its peak. The amplitude of the mean squared CIB fluctuation detected with AKARI and Spitzer is shown with a solid black square and triangles, respectively. As one can see, CIB fluctuations from the remaining known galaxies are such that, to probe a possible Lyman break of the CIB signal at 3.6 and 4.5 μm, one must eliminate sources to fainter magnitudes than feasible in the current experiments [see the discussion in Kashlinsky, Mather *et al.* (2015)].

2. Probing the CIB cross power and coherence with the CXB with good energy resolution and statistical precision

Probing the CIB cross power and coherence with the CXB with good energy resolution and statistical precision is further critically important in that it tells us in what fraction the CIB emissions come from stellar nucleosynthetic processes or are generated via BH accretion as well as proportions of the two kinds of populations. The use of Chandra as a probe for the CIB versus CXB coherence has intrinsic limitations arising from the design of the telescope itself (Sec. V.B.1.e). In fact, its main feature, the high angular resolution, has been obtained at the price of a relatively low effective area, a limited field of

view, and strong vignetting that limit the observatory's survey grasp. The net effects of this design on the Chandra survey performances and fluctuation studies are (a) deep coverage is reached only on a small portion of the field of view near the optical axis, (b) images are significantly shallower off axis, (c) modeling sources of noise and foreground is complicated by the broad PSF tails, (d) cosmic variance due to the limited corrected field of view severely affects the large-scale measurements of the clustering components, and (e) Poisson fluctuations due to the low photon surface density number (counts/pixel) (i.e., $\delta F_{\text{Poiss},X} \geq \delta F_{\text{CXB}}$) severely affect the maps. The net effect is that $P_{A-B} \gg P_{\text{CXB}}$ or, in other words, the x-ray fluctuations signal is instrument background dominated. These effects limit the reliability of CXB versus CIB coherence with Chandra to $\lesssim 1000''$. Suitably designed raster scans, as used for the UDS or EGS fields (Sec. V.B.1.e), or stacking fields can mitigate these effects (Cappelluti *et al.*, 2013, 2017). Another limitation is that P_{A-B} is 1 order of magnitude larger in the hard x-ray band than in the soft band (Cappelluti *et al.*, 2017). This limits the energy bands where the coherence can be evaluated and hence the precision on the SED of the signal. So far significant cross power has been measured only between CIB and [0.5–2] keV with upper limits derived in the hard x-ray bands, limiting probing of the x-ray spectrum of the sources. No measurement has been performed with XMM-Newton yet, despite its much larger collecting area and smaller vignetting compared to Chandra; XMM-Newton has a rather broad PSF (15'' half-energy width, on axis) that hampers the masking of resolved sources. Moreover XMM-Newton's orbit is such that the instrument suffers from severe background flaring and soft protons, which are difficult to model. For the same reason the larger effective area of XMM-Newton in the hard band cannot be fully exploited in fluctuation studies. Future survey missions, such as the Extended Roentgen Survey with an Imaging Telescope Array (eROSITA), will address these problems by covering an extensive area of sky with a high throughput wide-field telescope with smaller vignetting, which in addition will be canceled out by the scan geometry. The background in the eROSITA's L2 orbit may be more stable than for XMM-Newton. eROSITA's broad PSF will remain an issue, but we suggest possible successful strategies in combining eROSITA and Euclid.

3. Summary

To summarize the following thus appeared to be required to resolve these topics adequately based on the previous discussion: (1) near-IR sky maps over a large part of the sky integrated deep to $m_{AB} \gtrsim 24$, (2) corresponding visible band diffuse maps integrated to a depth of $m_{AB} \gtrsim 25$ or fainter, (3) corresponding diffuse x-ray maps of a large area and good energy resolution between $\lesssim 1$ and $\gtrsim 10$ keV in the observer frame, and (4) corresponding microwave diffuse maps covering large sky areas at several frequencies with $\sim 1'$ resolution and low instrument noise. These are required for the measurement of the power spectrum and SED of CIB, clustering versus shot noise, the Lyman break of the sources, cross powers with other wavelengths, and history of emissions.

VII. LIBRAE

Looking at Infrared Background Radiation Anisotropies with Euclid (LIBRAE) is a NASA approved project[5] to probe the CIB using data from the European Space Agency's M-class mission Euclid.[6] LIBRAE will exploit the Euclid imaging of the wide and deep surveys at near-IR and visible wavelengths to conduct CIB science with unprecedented precision and scope and will be able to probe both the origin of the CIB and its populations together with the conditions existing at high z. We discuss the technical prospects and methodology quantifying the science goals of LIBRAE.

A. Euclid configuration and data reduction methodology

The Euclid spacecraft will carry a 1.2 m telescope to a Sun-Earth L2 orbit with two instruments: the Visible Instrument (VIS) and the Near-Infrared Spectrometer and Photometer (NISP). The VIS instrument performs very broadband ($0.55 - 0.90 \ \mu$m) imaging using an array of 36 4k CCD detectors with a pixel scale of $0.1''$. NISP imaging is done in Y, J, and H bands using an array of 16 2k HgCdTe detectors at a pixel scale of $0.3''$. Via a beam splitter, both instruments have similar fields of view of $\sim 0.7° \times 0.7°$ (~ 0.53 deg^2).

Euclid's main scientific objectives, studying DE evolution to $z \sim 2$, require the mission to carry out two surveys. The wide survey aims to cover $\sim 20\,000$ deg^2 at a nominal depth, whereas the deep survey will total ~ 40 deg^2 observed to 2 magnitudes deeper than the wide survey. Data from both surveys should also be useful for studies of the source-subtracted CIB fluctuations. Laureijs *et al.* (2011, 2014) gave a comprehensive overview of the Euclid primary science goals, telescope, instruments, and observing strategy.

The analysis of source-subtracted CIB fluctuations would involve three largely separable tasks: (1) construction of source-subtracted images of suitable scale and depth, and minimal artifacts, (2) subtraction and masking resolved sources, and (3) evaluating the fluctuations.

The means of producing maps for CIB analysis has varied according to the data being used and the researchers performing the study. Default processing pipelines are usually more focused on the resolved sources and may not be designed to accurately reconstruct diffuse background emission that extends on scales larger than the detector. For Spitzer and IRAC data, self-calibration (Fixsen, Moseley, and Arendt, 2000) has proved a useful means of mosaicking individual frames into wider and deeper mosaic images, while removing a fixed-pattern structure that correlates with the detector rather than the sky (Arendt *et al.*, 2010). This technique may be applied to Euclid data, but given the size of the Euclid surveys there are several issues of scale which need to be addressed to do this efficiently.

The field size of the data that are self-calibrated and analyzed would be limited to sizes up to the maximum scale of interest for the CIB ($\sim 1°$). The limited field size retains the ability to analyze the 2D fluctuations without difficulties of the mapping projection. For some tests, much larger regions could be mapped and analyzed in HEALPIX format (Górski *et al.*, 2005). For angular scales sampled by the limited fields, averaging results from many fields should be equivalent to measurement of the same contiguous area. Multiple smaller fields also allow a wider capability to check field to field consistency.

Savings in processing speed and output data volume can be attained by reducing the resolution of the data. The smallest angular scale information is nonessential as it primarily reveals the shot-noise level of the CIB, which is also revealed at scales of $\sim 10''$ and larger (Fig. 34). In working with degraded resolution data, it will be useful to remove sources from individual exposures before creating mosaic images rather than after. Source removal can be based on the size, shape, and brightness of identified sources from the standard processing pipelines. Low resolution source-subtracted mosaics may also have a decreased fraction of masked pixels, because the low resolution pixel need only be masked if all of the underlying full-resolution pixels are masked.

The analysis of the power spectrum using FFTs, or the correlation function using slower methods, will be more expedient with smaller, lower resolution images and the project will involve both forms of analysis. Processing and analysis will be similar for both the wide and the deep surveys, as both will use the same observing strategy (exposure times and sequence, dithering, etc.). Because the deep survey fields are located near the ecliptic poles and are revisited regularly, the repeated coverage at constantly rotating position angles should lead to a better self-calibration result and improved data quality, beyond the direct increase in sensitivity of the observations.

B. Foregrounds: Galactic stars, ISM, and zodiacal light

The same foregrounds [stars, diffuse Galactic light (DGL), and zodiacal light] that can potentially affect the CIB fluctuation measurements of other spaced-based observations will need to be considered for analysis of the Euclid data as well (Secs. V.B.1.c, V.B.2, V.C.3, and V.C.4).

With high angular resolution and good sensitivity (Table IV), most Galactic stars can be individually resolved and masked at the high latitudes of the Euclid surveys. The stellar luminosity function declines at magnitude $M_J \gtrsim 8$ (Bochanski *et al.*, 2010), but even late M stars at $M_J \sim 11$ can be detected by NISP in the wide survey at a distance of several kpc. However, cooler and fainter brown dwarfs (Dupuy and Liu, 2012) will only be individually detectable on scales $\lesssim 100$ pc.

The DGL energy spectrum is expected to rise as wavelengths decrease from Spitzer IRAC's 3.6 μm band to Euclid NISP's Y band. At the Euclid wavelengths, the DGL should be strongly dominated by scattered light with little to no contribution from thermal emission. The wide survey will necessarily cover many regions of higher DGL intensity than previously studied small deep fields (usually selected in part for low ISM column densities). Thus the DGL will usually be stronger than in most previous studies, but the wide survey observations will allow a much more robust correlation of potential DGL against other tracers of ISM, or even simply Galactic latitude. Measured relative to the 100 μm thermal
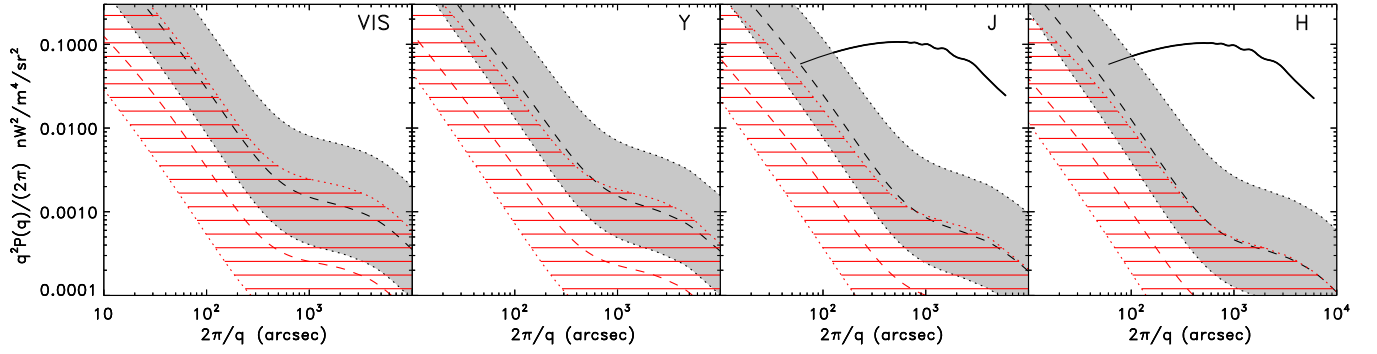

FIG. 34.   HRK12 reconstruction of fluctuations from known galaxies remaining in the Euclid VIS and NISP bands (Table IV) is shown with gray shaded areas for the wide survey and red lined areas for the deep survey; dashed lines denote the default reconstructions and dotted lines show the HFE to LFE limits for each band. The thick solid lines from Kashlinsky, Arendt *et al.* (2015) are examples of high-z CIB, which fits Spitzer 3.6 and 4.5 μm CIB fluctuation data, based on the IMF500 model from Helgason *et al.* (2016) with $f_* = 0.04$ ending at $z_{end} = 10$; it has no emissions in the Y and VIS bands due to the Lyman cutoff of the source emissions.

dust emission, the mean intensity of high latitude DGL at $\sim$0.4–5 μm has been pieced together by a number of studies (Brandt and Draine, 2012; Tsumura *et al.*, 2013; Arai *et al.*, 2015; Sano *et al.*, 2015, 2016). However, these and other studies (Mitchell-Wynne *et al.*, 2015) also reported significant variations in the DGL at varied locations.

To help minimize backgrounds and increase sensitivity, the Euclid surveys avoid low ecliptic latitudes. However, the range of allowed solar elongations is limited compared to most other facilities, and repeat coverage will exist only for the deep survey and calibration fields. Therefore, detection of zodiacal light influences through temporal tests will be limited, and examination of trends versus ecliptic latitude may be the most useful approach for the wide survey. A critical look at the colors of the fluctuations can also be useful as CIBER results indicate that the mean CIB spectrum is redder than the zodiacal light (Matsuura *et al.*, 2017). At longer wavelengths, 3.6–4.5 μm, Arendt *et al.* (2016) showed that the zodiacal light does not affect the power from clustering in large-scale fluctuations, but it does contribute to the white noise component of the power spectrum.

C. Probing the power spectrum and its Lyman break

The configuration of Euclid's near-IR and visible bands and the coverage and depth of the surveys are all uniquely suitable in probing, highly accurately, source-subtracted CIB fluctuations

TABLE IV.   Euclid survey parameters. Remaining known sources CIB, $F(>m_0)$ in nW/m^2/sr, and shot noise, P_{SN} in nJy nW/m^2/sr. Limiting magnitudes for remaining sources use $\sim$2.5σ removal as will be used in CIB studies, which differs from the nominal 5σ by $\Delta m = 0.75$.

Survey	Area (deg^2)	VIS 0.6–0.9μm	NISP-Y 0.9–1.2μm	NISP-J 1.2–1.5μm	NISP-H 1.5–2μm
Wide	2×10^4	$m_{lim}=26$	$m_{lim}=25$	$m_{lim}=25$	$m_{lim}=25$
$F(>m_0)$		$1.1^{+1.4}_{-0.5}$	$1.1^{+1.1}_{-0.5}$	$0.8^{+0.9}_{-0.3}$	$0.6^{+0.7}_{-0.3}$
P_{SN}		46^{+31}_{-17}	120^{+69}_{-39}	95^{+63}_{-34}	73^{+60}_{-29}
Deep	40	$m_{lim}=28$	$m_{lim}=27$	$m_{lim}=27$	$m_{lim}=27$
$F(>m_0)$		$0.5^{+1.0}_{-0.3}$	$0.5^{+0.8}_{-0.3}$	$0.3^{+0.6}_{-0.2}$	$0.2^{+0.4}_{-0.1}$
P_{SN}		$3.3^{+4.1}_{-1.7}$	$8.4^{+8.8}_{-4.0}$	$5.9^{+7.0}_{-3.0}$	$4.2^{+5.7}_{-2.2}$

from new sources at early times. The large area covered by Euclid's wide survey enables measuring the fine features of their power spectrum with unprecedentedly high precision and the deep survey allows probing the clustering component at unprecedentedly faint depth. Table IV gives the mean CIB levels and shot-noise amplitudes due to known galaxies from the HRK12 reconstruction at the Euclid wide and deep survey configurations.

Mask corrections for the evaluated power are not expected to be important with the Euclid configuration: at 0.3″ resolution there would be $\sim$1.44 $\times$ 10^8 pixels/deg^2, whereas at the depth of the deep survey there would be $\sim$2 $\times$ 10^5 sources/deg^2 according to deep counts at the near-IR NISP bands. Even taking conservatively $\sim$30–50 pixels/source on average, the mask would eliminate only a few percent of the pixels in the wide survey and a bit more in the deep survey. However, although the mask fraction is small enough to enable robustly accurate power computation, the images would already be in the confusion limit for their deepest sources, increasing the usefulness of CIB studies. In this limit the correction for masking, even if necessary in this high-precision measurement, can be done using a methodology of Kashlinsky *et al.* (2012) adopting a high-accuracy template as prior, running it through the mask in simulated maps and comparing the output to measurements. At this resolution removing sources at 2.5σ, or even more aggressively, would be possible; in this limit only $\sim$1% of the noise pixels would be additionally removed at this threshold. This makes the expected total fraction of removed pixels comfortably below 10%.

Figure 34 shows the advantages provided by the Euclid configuration for CIB power measurements. The HFE to LFE range of CIB fluctuations from the HRK12 reconstruction of remaining known galaxies is shown with shaded regions for each configuration. Thick lines show high-z CIB examples, which fit Spitzer 3.6 and 4.5 μm CIB fluctuation data (Kashlinsky, Arendt *et al.*, 2015; Helgason *et al.*, 2016). The figure shows that such CIB fluctuation components can be robustly resolved in the presence of the known galaxies remaining here. The bulk of the fluctuation signal is contained between $\sim$1′ and a few degrees with the peak near 10′–15′ corresponding to the ΛCDM power spectrum projected to the distance of the emitting sources. The large total area available

for the CIB maps would enable the CIB power measurement with better than subpercent statistical accuracy below 1° assuming that $10\,000\ \mathrm{deg}^2$ would be useful for CIB analysis. In the $40\ \mathrm{deg}^2$ area of the deep survey, the power spectrum will be measured with better than $\lesssim 15\%\ (\theta/1°)$ statistical accuracy on subdegree scales. Thus the fine structure of the CIB can be resolved with high statistical accuracy in both Euclid configurations.

Figure 34 also shows that in this configuration the Lyman break of the high-z CIB component can be probed robustly. In both the VIS and Y bands the levels of remaining known galaxies are comfortably below the high-z component normalized to the measured source-subtracted CIB from Spitzer and which is prominent at the Euclid J and H bands.

Figure 22 shows that the clustering component of the CIB fluctuations does not yet appear to decrease, within the measurement errors, with the lower shot noise reached in deeper IRAC integrations. As discussed earlier this sets strong constraints on nature of the individual sources producing these CIB anisotropies and finding the shot-noise level which starts affecting (decreasing) the large-scale clustering component of the CIB would provide important information about the sources producing it. The wide and deep surveys of Euclid appear suitable for probing with good accuracy the clustering component as a function of shot noise out to significantly lower depths and larger angular scales than hitherto possible.

To conclude this discussion, the Euclid parameters, designed for independent dark energy studies, are well positioned to (1) probe the fine structure of the CIB power spectrum highly accurately, (2) directly determine the epochs of the sources producing them from the Lyman cutoff by comparing with the signal at the shorter wavelengths, and (3) probe the behavior of the clustering component as one reaches significantly lower shot-noise levels.

D. Probing BH contribution: CXB-CIB cross power

In addition to the already operating x-ray satellites, Chandra and XMM-Newton, the expected 2018 launch of eROSITA will be of significant importance for the LIBRAE measurements of the CXB-CIB cross power. eROSITA[7] is an instrument developed by the Max Planck Institute for Extraterrestrial Physics together with the German Space Agency DLR, to fly on Russia's space mission Spektrum-RG (SRG). It consists of an array of seven Wolter-type I nested mirror systems with seven x-ray CCD detectors in the focal planes. It will perform an all-sky x-ray survey in the [0.1–12] keV range. In the [0.1–2] keV band, the survey will be ∼30 times deeper than the Röntgensatellit (ROSAT) all-sky survey, while in the [2–12] keV band eROSITA will perform the first ever all-sky survey with a focusing x-ray telescope. The eROSITA active field of view will be ∼1 deg², which together with the large collecting area gives eROSITA a grasp of ∼1000 cm² deg² at [0.5–2] keV, about 3 times larger than the combination of the three XMM-Newton telescopes (Merloni *et al.*, 2012). The eROSITA PSF will have a half power diameter (HPD) of ∼15″ on axis and 28″ in survey mode.

The eROSITA All-Sky Survey (eRASS) will map the entire sky with a cadence of 6 months and an average exposure of ∼2.5 ks, plus two ∼100 deg² regions of deep survey, with an exposure of the order of 100 ks at the north and south ecliptic poles (NEP, SEP), corresponding to limiting sensitivity of 1.1×10^{-14} and $2 \times 10^{-15}\ \mathrm{erg\,cm^{-2}\,s^{-1}}$, respectively. In the deep survey the source density will be ∼400 deg⁻². By masking the x-ray sources with a radius of the HPD, about 90% of the image pixels will be available for the analysis, but still a significant fraction of the source flux will leak outside the mask, which will contaminate the diffuse light estimate.

Since the uncertainty on the cross-power spectrum is proportional to the square root of the survey area, eROSITA and Euclid will provide results to better than $\lesssim 10\%$ statistical uncertainties out to 1°–2° scales. LIBRAE will cross correlate the Euclid bands with eROSITA x-ray bands and, on smaller areas with Chandra or XMM-Newton. In theory, if the observed CXB-CIB cross power is due to accreting BHs at high z, we do not expect to measure similarly strong coherence between the CXB and the (VIS, Y) as with J and H bands if the typical sources lie at $z > (4, 6.5)$.

LIBRAE will measure the average x-ray spectrum of the sources contributing to the excess fluctuations by cross correlating multiple x-ray bands with one or more near-IR bands. The eROSITA range could be divided into energy bands compatible with the x-ray CCD energy resolution that reaches 60 eV at low energies and >100–150 eV at high energies (>2 keV). However, in a tradeoff between energy resolution and signal-to-noise ratio a reasonable energy resolution in the x-ray band will be of the order of 0.5 to 1.5 keV. The x-ray spectrum carries information about the amount of intrinsic absorption in the host galaxy (measured with the depression of the low energy signal) and the accretion rate (measured with the spectral index). This information, combined with a precise measurement of the clustering properties, may constrain the number density of the sources. These are important quantities since, if these are high-z BHs, the number density, accretion rate, and column density are key descriptors of these BH populations. If the sources are instead at low z, these are important to characterize the nature of these populations.

How well can Euclid and eROSITA (and Chandra) measure any CXB-CIB cross powers? To provide an estimate of the noise floor for these forthcoming measurements by using realistic assumptions of the instrument configurations, we simulated Euclid deep survey fluctuation maps of $40\ \mathrm{deg}^2$ where the signal is produced only by the shot noise from unresolved discrete sources. The shot-noise levels used are from Table IV and we varied them according to assumptions on the faint end of the luminosity function adopted in the extrapolation to faint Euclid limiting magnitudes (Helgason, Ricotti, and Kashlinsky, 2012). For eROSITA we simulated two deep survey maps of $40\ \mathrm{deg}^2$ each with 100 ks exposure in the [0.5–2] keV and [2–10] keV bands. The maps have an average count rate of 2.14 and 0.92 count/s/arc min² (Merloni *et al.*, 2012) in the two bands, respectively. The count rates have been converted into count maps with an exposure map and Poisson noise was added. The maps have

been then transformed into surface brightness maps with an energy conversion factor given by the instrumental response and finally into fluctuation maps in units of $\mathrm{erg\,cm^{-2}\,sr^{-1}}$. The same procedure has been adopted to create simulated noise maps with the typical configuration of a Chandra medium-deep field of $\sim 0.2\ \mathrm{deg^2}$, and an exposure of 400 ks, by using the background values in the EGS field analysis by Cappelluti *et al.* (2013, 2017).

From those maps we estimated the 3σ noise floor of the cross-power spectrum for every combination of band and instrument configuration. In Fig. 35 we show the computed 3σ upper limit on the noise power, i.e., $3\sqrt{P_{\mathrm{IR}}(q)P_X(q)/N(q)}$, where $P_{\mathrm{IR}}(q)$ and $P_X(q)$ are the IR and x-ray power spectra, respectively. The eROSITA versus Euclid noise floors will be systematically lower (up to one dex) than those of Chandra and Euclid. Such a difference is driven mostly by the larger area sampled by eROSITA, despite the shallower depth compared to Chandra. Noteworthy in this context is the much higher hard x-ray band sensitivity of eROSITA than Chandra.

The expected mean squared amplitude $q^2 P_{\mathrm{IR},X}/2\pi$ for the noise floor is $\lesssim (0.5\text{--}5)\times 10^{-13}\ \mathrm{nW\,m^{-2}\,erg\,cm^{-2}\,sr^{-2}}$ on scales $\sim 100''-500''$, assuming binning of $\Delta\log(q)=0.15$. The observed 3.6 and 4.5 μm vs [0.5–2] keV cross power in the same angular range is $\sim (3\text{--}5)\times 10^{-11}\ \mathrm{nW\,m^{-2}\,erg\,cm^{-2}\,sr^{-2}}$. This means that we can measure dropouts in the cross power between x-ray versus 3.6 μm and x-ray versus Euclid H–VIS bands of the order $\sim 10^2$. This corresponds to [3.6]–[H] through [VIS] colors of up to ~ 5 magnitudes, which are sufficient to obtain significant measurements of the Lyman break. However, this means that, regardless of the nature of the sources, it will be possible for the first time to infer the properties of source populations with a detailed measurement of the broadband SED of the EBL fluctuations.
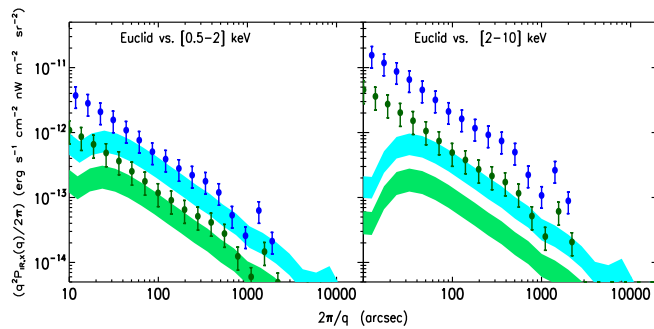

FIG. 35. Left: Estimates of the Euclid vs [0.5–2] keV cross-power noise floor. Solid bands represent the Euclid vs eROSITA configuration for 40 $\mathrm{deg^2}$ survey described here. The symbols represent the 3σ detection floor expected from the HRK12 reconstruction of contributions from known galaxies remaining (Table IV) in the shown binning. Cyan (upper) shading shows the floor for the eROSITA vs Euclid-VIS cross power; green eROSITA vs *Euclid-H*. Blue and dark green (upper and lower) dots (mean value from Table IV) with intervals (HFE and LFE) represent configurations for Chandra vs Euclid-VIS and Chandra vs Euclid-H, respectively. Right: Same as left for [2–10] keV band.

E. Probing IGM at pre-reionization: CMB-CIB crosspower

At high z, the early sources, responsible for CIB fluctuations, would have ionized and heated up the surrounding gas which, in principle, would generate secondary anisotropies in the CMB via the TSZ effect. Given that Euclid will cover $\sim 20\,000\ \mathrm{deg^2}$ with subarcsecond resolution at three near-IR channels, this weak signal may be teased out of the noise, after suitable construction of a comparably large-area, low noise, multifrequency CMB maps at roughly arcmin resolution which are expected to be available in the near future. Atrio-Barandela and Kashlinsky (2014) showed how such measurements can lead to a highly statistically significant result. At the same time, the CIB signal from high z should have no correlation with the diffuse emission maps obtained from the Euclid VIS channel if the sources' epochs are such that the Ly-α line is redshifted beyond 0.9 μm; this would facilitate isolating the CMB-CIB cross power from high z.

For example, massive Population III stars have approximately constant surface temperature $T_* \sim 10^5$ K producing a large number of ionizing photons with energy ≥ 13.6 eV and resulting in a constant ratio of the ionizing photons per H-burning baryon in these objects. There would be $\sim 10^{62} M_*/M_\odot$ ionizing photons produced over the lifetime of these stars ($\sim 3\times 10^6$ yr) (Bromm, Kudritzki, and Loeb, 2001; Schaerer, 2002) by a halo containing M_* in such sources. If κ ionizing photons are required to ionize a H atom, around each halo containing M_* in stars there will be a bubble of $M_{\mathrm{ion}} \sim 10^5 \kappa^{-1} M_*$ ionized gas, heated to a temperature of $T_e \equiv T_{e,4} 10^4$ K. If the electron temperature T_e and density n_e are constant, the Comptonization parameter averaged over the solid angle ω_B subtended by the bubble would be $Y_{C,B} = (4/3)\sigma_T n_e R_{\mathrm{ion}}(kT_e/m_e c^2)$, where R_{ion} is the radius of the ionized cloud. Each ionized bubble would generate a CMB mean distortion over an area of solid angle ω given by $t_{\mathrm{TSZ},B} = G_\nu Y_{C,B}(\omega_B/\omega)T_{\mathrm{CMB}}$, where G_ν is the frequency dependence of the SZ effect. The net distortion will be the added contributions of all bubbles in the CMB pixel $T_{\mathrm{TSZ}} = n_2\omega t_{\mathrm{TSZ},B}$, where $n_2\omega$ is the total number of bubbles along the line of sight on a pixel of solid angle ω.

Since the shot-noise power is $P_{\mathrm{SN}} \sim F_{\mathrm{CIB}}^2/n_2$, the sky density of these sources is given by Eq. (18), leading to

$$T_{\mathrm{TSZ}} \simeq \frac{4}{\pi} G_\nu T_{\mathrm{CMB}} \frac{k_B T_e}{m_e c^2} \frac{\sigma_T}{d_A^2} \frac{M_{\mathrm{ion}}}{\mu m_H} \frac{F_{\mathrm{CIB}}^2}{P_{\mathrm{SN}}}$$

$$\simeq 200 G_\nu \left(\frac{0.5\ \mathrm{Gpc}}{d_A}\right)^2 \frac{M_*}{10^4 \kappa \mu M_\odot} T_{e,4}. \qquad (21)$$

Here F_{CIB} is the net CIB flux from these sources in $\mathrm{nW/m^2/sr}$, μ is the mean gas molecular weight, and k_B is the Boltzmann constant. M_* corresponds to a conservative choice for the mass of the ionizing sources in each early halo and the proper angular diameter distance $d_A = 0.5\text{--}0.9$ Gpc at $z = 20\text{--}10$. For Eq. (21), the effective Thomson optical depth due to the reionized medium $\Delta\tau \equiv 200\,\mathrm{nK}/[T_{\mathrm{CMB}}(k_B T_e/m_e c^2)] = 0.044$ is below the measurement values in Table II.

Because of variation in the number density of bubbles with a relative number fluctuation of $\Delta \simeq 0.1$, the CMB distortion

T_{TSZ} would generate CMB temperature fluctuations. The TSZ temperature anisotropies would have amplitude $\sim T_{TSZ}\Delta$ that is potentially detectable by cross correlating the produced CMB anisotropies with CIB fluctuations. For bubbles coherent with CIB sources, the cross power between CIB and TSZ is $P_{CIB\times TSZ} \simeq \sqrt{P_{CIB}}\sqrt{P_{TSZ}}$. To compute this cross correlation, the subarcsec Euclid CIB and arcmin resolution CMB maps will be brought to a common resolution. When measuring the cross power from IR and microwave (mw) maps of N_{pix} CMB pixels, the error is $\sigma_{P_{CIB\times TSZ}} \simeq \sqrt{P_{IR}}\sqrt{P_{mw}}/\sqrt{N_{pix}}$, since at $\gtrsim 1'$ the Euclid CIB maps will have negligible noise with $P_{IR} = P_{CIB}$. From the Euclid wide survey the CIB power on arc min scales will be measurable by LIBRAE to subpercent statistical accuracy. If primary CMB is removed, the foreground-reduced microwave maps would be dominated by instrument noise σ_n, foreground residuals $\sigma_{f,res}$ and, more importantly, the TSZ of the unresolved cluster population $\sigma_{cl,unr}$. With N_ν microwave frequency channels the variance of the microwave map would be $\sigma_{mw}^2 = \sigma_n^2/N_\nu + \sigma_{f,res}^2 + \sigma_{cl,unr}^2$. The signal-to-noise ratio would be $S/N \simeq T_{TSZ}\Delta\sqrt{N_{pix}}/\sigma_{mw}$, reaching $S/N \gg 1$ for certain experimental configurations. Specifically

$$S/N = 7\frac{T_{TSZ}}{200 \text{ nK}}\frac{\Delta}{0.1}\left(\frac{\sigma_{mw}}{5 \ \mu K}\right)^{-1}\left(\frac{N_{pix}}{3\times 10^6}\right)^{1/2}, \quad (22)$$

where $N_{pix} = 3 \times 10^6$ is the expected sky coverage of the Euclid wide survey at the native Planck resolution of $5'$. At the same time, emissions from early times, $z \gtrsim 10$, should exhibit no correlations at VIS and likely Y bands with CMB enabling the measured cross power from the Euclid's longest wavelength bands to be uniquely interpreted.

The CMB-CIB cross power peaks around $\sim 10'$, scales which can be probed with the forthcoming CMB instruments that plan to cover large areas of the sky with noise of $\sigma_n \lesssim$ a few μK. Also important in eliminating the contribution of primary CMB and the KSZ terms to the measured signal is availability of multiple frequencies covering both sides of the TSZ zero frequency at ~ 217 GHz; any components having blackbody energy spectrum can then be eliminated in taking T differences at different frequency pairs as proposed by Atrio-Barandela and Kashlinsky (2014). The CMB data from the forthcoming experiments planned to complete by the time of the Euclid surveys would reach higher S/N of the CMB-CIB cross power than the combined Planck and SPT data shown in Fig. 36. In its first two years of observation, the ACTPol camera observed ~ 600 deg^2 at 149 GHz with a noise level of 17 μK arc min and a resolution of $1.3' - 2'$ for the different arrays (Sherwin *et al.*, 2017). The NSF-supported new Adv ACTPol camera will observe in five bands spanning the 25–280 GHz range with a resolution of $\sim 1.5'$ (Ward *et al.*, 2016), similar to the currently operating ACTPol. Currently the AdvACTPol configuration is planned to map $\sim 10^4$ deg^2 with subarcmin resolution of $1.3'$ FWHM at frequencies of ~ 97 and ~ 148 GHz (Thornton *et al.*, 2016). At the smallest angular scales, the Silk-Michie damping suppresses the primary CMB temperature anisotropies to an amplitude $\delta T \lesssim 1 \ \mu K$ leaving the variance of the microwave map dominated by the instrument noise and possible foreground residuals.
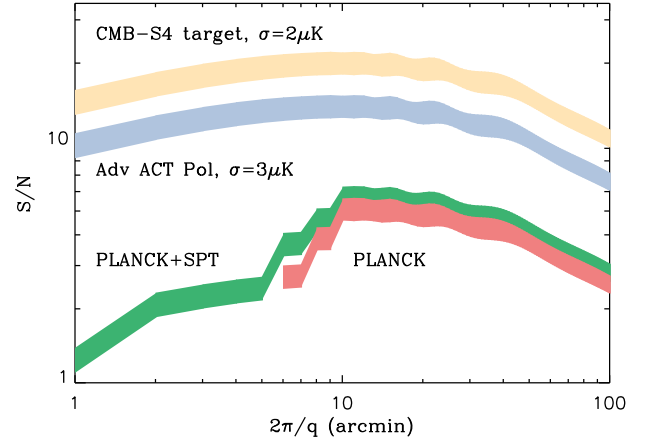

FIG. 36. Filled regions show the range of the S/N of the CIB-TSZ cross power over the Euclid wide survey region covered by the model parameters for different experimental configurations for $T_{e,4} = 1$. Planck parameters are for 2 yr of integration. At $5'$ only 353–217 GHz difference maps would be useful, at $7'$ we also add 143–217 GHz, and at $> 9'$ we can add the data from 100–217 GHz. SPT has lower S/N, but can probe angular scales as low as $\sim 1'$. In its current configuration the ACT does not add appreciably to the measurement, but that can be improved with advanced ACT and CMB stage 4 experiments as shown with the two upper bands. Adapted from Atrio-Barandela and Kashlinsky, 2014.

The larger frequency coverage will allow one to efficiently remove foregrounds. Although the final sensitivity and total observing area are yet to be determined, the noise is a factor of ~ 5–6 lower than in the current data, and the new camera can observe $\gtrsim 2 \times 10^3$ deg^2, covering $\sim 3 \times 10^6$ pixels in a reasonable amount of time. Then the cross correlation of a single map with the source-subtracted CIB data will reach the S/N shown in Fig. 36, if foreground residuals are negligible. These results are easily scalable to other noise levels and different configurations, since $S/N \propto (N_{pix}/\sigma_n^2)^{1/2}$ where N_{pix} is the number of pixels in the survey area, and σ_n^2 is the noise variance of the observations. The CMB-CIB cross power can be determined with a statistical $S/N \sim 25$ if the CMB-S4 generation of experiments currently being designed reach their noise target of $\leq 2 \ \mu K$ arc min with an angular resolution of $\lesssim 2'$ (Abitbol *et al.*, 2017).

F. History of emissions from Lyman tomography

The NISP filters, depth, and sky coverage available for LIBRAE with the Euclid mission appear particularly useful for the application of the Lyman-tomography method (Sec. IV.D.7) (Kashlinsky, Arendt *et al.*, 2015). The large areas covered by the Euclid surveys enable high-precision measurement of the source-subtracted CIB power spectra in each of the bands which then allow accurate construction of the quantity $P_{\Delta z} \equiv P_2 - P_{12}^2/P_1$ in each of the two NISP band pairs $[J\text{-}Y, H\text{-}J]$, with subsequent wavelengths ordered $\lambda_2 > \lambda_1$. In terms of the z range, the Y-J configuration then covers CIB emissions over $8.8 < z < 11.7$ and the J-H isolates CIB from $11.7 < z < 15.4$; the upper and lower redshifts of these ranges are denoted as z_1 and z_2. This assumes the Lyman cutoff at rest Ly-α of $\lambda_{Ly} = 0.12 \ \mu m$,
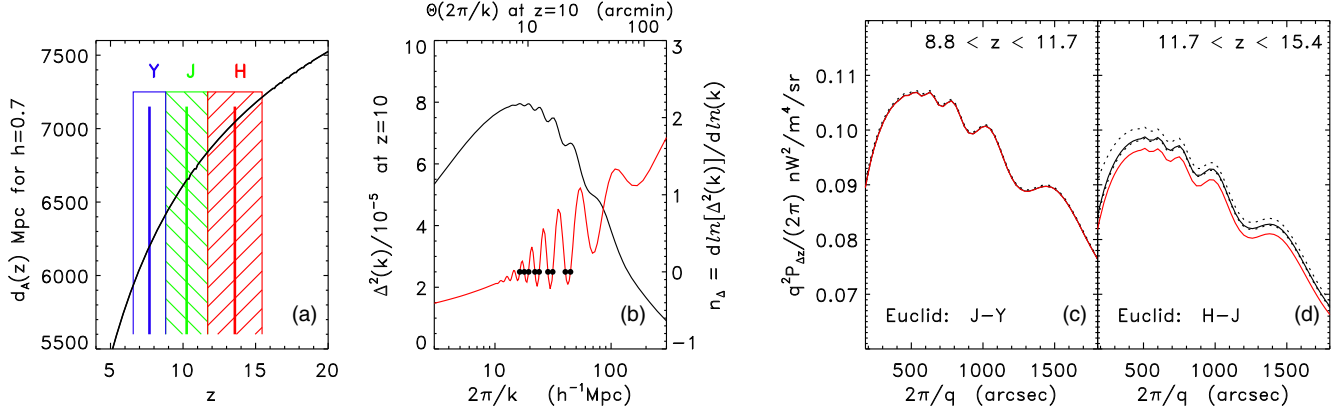
FIG. 37. (a) The solid line shows the d_A span vs z over the Y, J, and H Euclid filters; vertical lines mark the central wavelength of each filter. At these z the Lyman break corresponds to Ly-α at 0.1216 μm. (b) The solid line shows $\Delta^2(k)$ at $z = 10$. The red line and the right axis show the spatial spectral index n_Δ of $\Delta^2(k)$ with the solid dots marking its extrema. For the HZ regime, $n_\Delta = 3$, which is reached at larger scales. (c), (d) The Lyman-tomography reconstruction of the history of emissions and BAOs for Euclid's (Y, J, and H) filters and wide survey depth at each redshift range displayed in red. The red line shows the underlying CIB fluctuations by sources in the marked z range from high-z stellar populations reproducing Spitzer measurements. The black lines show the reconstructed one with contributions by known remaining galaxies from HRK12 with the dotted lines showing the HFE to LFE limits. Adapted from Kashlinsky, Arendt *et al.*, 2015.

appropriate for the pre-ionization conditions at these epochs. Figure 37(a) shows that these Euclid filters isolate emissions over a narrow range of distances about $\simeq$5%–7% in comoving d_A, centered at d_0. For reference, $2\pi/q = 10'$ corresponds to $\ell = 2160$ and subtends a comoving scale of $\simeq$20h^{-1} Mpc at $z = 10$, scales that are in a highly linear regime at those epochs.

The power spectrum of the emitting sources would be proportionally related to the underlying ΛCDM one, since the relevant angular scales subtend tens of comoving Mpc where the density field was highly linear. Because the procedure isolates a narrow shell in $d_A(z)$ around d_0, the comoving angular distance to the central filter wavelength, one can further expand

$$\Delta^2_{\Lambda CDM}(q/d_A) \simeq \Delta^2_{\Lambda CDM}(qd_0^{-1})\left\{1 - n_\Delta(qd_0^{-1})\left[\frac{\delta d_A}{d_0}\right]\right\},$$

where $n_\Delta(k) \equiv d\ln\Delta^2_{\Lambda CDM}(k)/d\ln k$ is the spatial spectral index of the ΛCDM template and $\delta d_A \equiv d_A(z) - d_0 \lesssim$ (5–7)%d_0. Figure 37(b) shows the template expected from the concordance ΛCDM model and the spectral index n_Δ. Given the narrow range of d_A spanned by each Euclid filter for the Lyman tomography and the values of n_Δ the power from sources over the narrow range of epochs can be approximated as

$$\frac{q^2P_{\Delta z}}{2\pi} \simeq \Delta^2_{\Lambda CDM}(qd_0^{-1})\int_{z_{Ly}(\lambda_1)}^{z_{Ly}(\lambda_2)}\left(\frac{dF_{\lambda_2'}}{dz}\right)^2 dz. \quad (23)$$

Equation (23) shows that (1) the history of emissions over $z_{Ly}(\lambda_1) < z < z_{Ly}(\lambda_2)$ is recoverable in the Euclid adjacent filter configurations and (2) the resultant $P_{\Delta z}$ preserves information about underlying parameters over these z. Both can be recovered in the LIBRAE CIB measurements.

Figures 37(c) and 37(d) illustrate the potential accuracy of this procedure in recovering the history of CIB emissions with an example normalized to reproduce Spitzer fluctuations at 3.6 and 4.5 μm. It is taken from Kashlinsky, Arendt *et al.* (2015) using (1) an IMF500 modeling (Helgason *et al.*, 2016) and (2) a Euclid-specific reconstruction of the contribution from remaining known galaxies from HRK12. The red lines show the true history of the emissions inside halos collapsing according to the standard ΛCDM model. Incoherence due to remaining known galaxies is explicitly incorporated in this example and the history recovered with this method is shown with the black lines covering the span of systematic uncertainties of the reconstruction. Except for a slight bias upward of a few percent, the history of emissions appears recovered accurately with the Euclid configuration, even preserving the BAO features in the underlying power spectrum in this example. Kashlinsky, Arendt *et al.* (2015) showed that good accuracy is achieved even when only a few percent of the Spitzer-based CIB fluctuations originate at high z. In practice, with the Spitzer CIB measurements the true z will be verified by measuring the distance from fitting the angular template which appears accurately recoverable.

G. Probing BAOs and dark energy at $10 < z < 16$

Euclid's goal is to explore the Universe's expansion history to understand the origin of the current accelerated period and the nature of DE by measuring the clustering of galaxies out to $z \simeq 2$ and the weak lensing distortion out to $z \leq 3$. Amendola *et al.* (2018) summarized the main observables to be extracted from the data to forecast future performance of the satellite in testing the various models. The Ly tomography described will, in principle, be possible using all four Euclid filters, VIS, Y, J, and H. The results will contribute to these goals by exploring the BAOs and cosmological parameters at redshifts $6 \lesssim z \lesssim 16$, much higher than those available with the standard techniques (Kashlinsky, Arendt *et al.*, 2015).
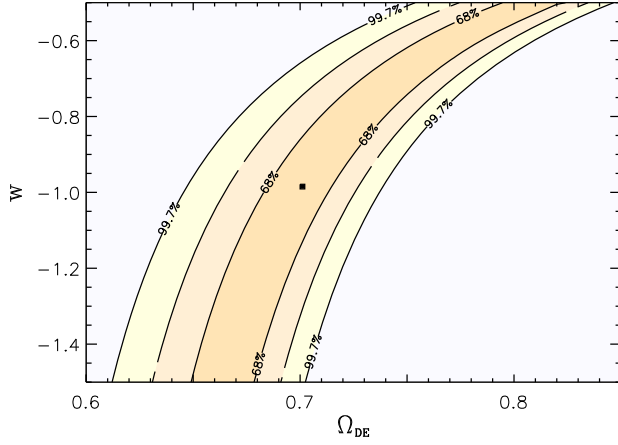
FIG. 38. Constraints on the DE equation of state parameter w and DE density Ω_{DE} from the Ly-α tomography with the Euclid diffuse maps using differencing configurations of [Y-VIS], [J-Y], and [H-J]. Contours correspond to the 68%, 95.5%, and 99.7% (1σ, 2σ, and 3σ) confidence levels as marked.

FIG. 39. Panoramic diagram of the LIBRAE goals.

From the derived CIB maps used in the tomographic reconstruction, [Y-VIS], [J-Y], and [H-J], isolating populations over $\Delta d_A \ll d_A$, LIBRAE will test the expected ΛCDM template at this new range of z. The location and amplitude of the maximum and BAOs imprinted in the matter power spectrum can be used then to determine cosmological parameters. To that purpose, the power spectrum needs to be sampled with sufficient angular resolution. In the frequency domain the resolution Δq is set by the maximum size Θ_0 of the region being analyzed $\Delta q = 2\pi/\Theta_0$. To achieve a resolution of $\Delta\theta = 0.5'$ requires $\Theta_0 \sim 20°$ (Kashlinsky, Arendt *et al.*, 2015). Since the power is measured from CIB fluctuations that are biased with respect to the underlying matter power spectrum, the data constrain the overall shape but not its amplitude. Consequently, all cosmological parameters that modify the shape and location of the acoustic peaks, such as Ω_{bar}, Ω_K, massive neutrino energy density, etc., can be constrained by the tomographic reconstruction of the power spectrum.

BAOs encode information about the sound horizon at recombination, whose value is $r_s = 144.81 \pm 0.24$ Mpc (Ade *et al.*, 2014). The angular scale subtended by the sound horizon can be measured from the correlation function of galaxies to derive angular diameter distances at epochs probed by galaxy catalogs (Eisenstein and Hu, 1998). The technique can also be applied to the frequency domain (Percival *et al.*, 2010) to constrain Ω_{DE}, the DE equation of state $p = w\rho c^2$, and/or the interactions within the dark sector (Wang *et al.*, 2016). The dynamical evolution of DE affects reionization of the Universe (Xu, Zhang, and Wang, 2017) and Lyman tomography will provide angular diameter distances to that z, allowing us to test the effect of models on an epoch that cannot be probed with current techniques (Aubourg *et al.*, 2015).

Figure 38 shows constraints on the equation of state w and energy density Ω_{DE} at the 68%, 95%, and 99.7% confidence
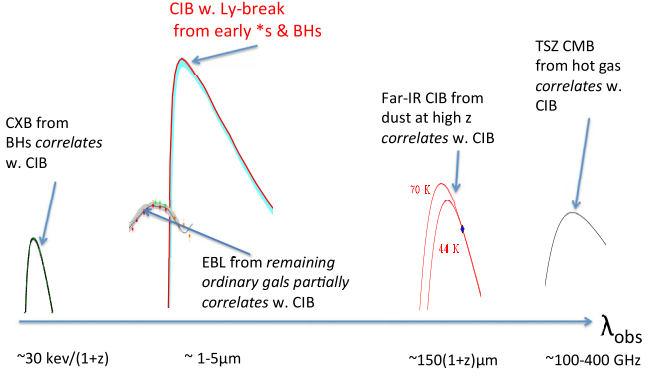
levels derived applying the Lyman-tomography technique to Euclid data. The simulations are centered around the ΛCDM model with $\Omega_\Lambda = 0.68$. The cosmic variance errors are for a rectangular patch of area $20° \times 10'$ and do not include instrumental noise and systematic effects. While the method may not constrain the parameters as well as other techniques, it extends the BAO regime to epochs not yet tested and could be complemented with measurements at lower z such as those of Hemantha, Wang, and Chuang (2014) and Wang (2014) to put stronger constraints on DE properties (Wang and Mukherjee, 2006). In addition, it gives an important self-consistency test and could supply valuable information to resolve the current discrepancy in BAO measurements at $z < 1$ and $z \simeq 2$–3 (Aubourg *et al.*, 2015).

H. LIBRAE summary

LIBRAE's goals are summed panoramically in Fig. 39 as follows:

- Measuring the power spectrum of source-subtracted CIB fluctuations at near-IR to subpercent statistical accuracy with the wide survey's NISP data.
- Probing epochs of sources producing the CIB fluctuations by cross correlating with diffuse light from the wide survey's VIS data.
- Probing the CIB properties as a function of depth from the deep survey.
- Determining the nature of the sources (BHs versus stars) by cross correlating with x-ray data assembled for this project.
- Probing the condition of the IGM at pre-reionization by cross correlating source-subtracted CIB from the wide survey with multifrequency all-sky CMB data.
- Probing the history of emissions at $10 < z < 20$ using Lyman tomography.
- Probing BAOs and DE evolutions at $10 < z < 20$ using the Lyman tomography.

LIBRAE will thus identify the net emissions from the first stars era, lead to a better understanding of the IGM at that epoch, isolate the contributions from the first BHs, and probe the history of emissions at $9 \lesssim z \lesssim 16$ and the cosmological parameters at those times.

VIII. OTHER FORTHCOMING EXPERIMENTAL CONFIGURATIONS

JWST with its near-IR camera, NIRCam, will identify individual sources to much fainter fluxes than either Spitzer or AKARI creating an opportunity to measure cumulative CIB emissions produced at still earlier epochs or from fainter sources. The NIRCam wavelength coverage spans seven wide overlapping filters from 0.7 to 5 μm and so will have a built-in capability to directly probe the Lyman break of the unresolved populations, provided the instrument noise, astronomical foregrounds, and foreground galaxy populations can be isolated. Kashlinsky, Mather *et al.* (2015) identified an experimental configuration of the JWST which, together with the strategies developed there, can provide critical insight into the origin of the source-subtracted CIB fluctuations detected in Spitzer and AKARI measurements, identify the epochs where the fluctuations arise, probe the fluxes of the sources producing them, and reconstruct or constrain the history of the emissions via the proposed adjacent two-band Lyman tomography. They showed that the CIB science dictates a configuration with 400 hr of NIRCam mapping for all seven wide NIRCam filters of 1 deg^2 contiguous area to $m_{AB} \simeq 28$ in a low cirrus region, e.g., the Lockman hole or CDFS. With that setup one would be able to address important questions pertaining to the details and nature of populations that led the Universe out of the Dark Ages. They also discussed the effects of the open configuration of the JWST on the CIB study arguing that the potential stray light effects may be mitigated to yield a fundamental constraint on the otherwise inaccessible range of epochs (and fluxes) of the CIB sources that are expected to lie in the confusion noise of the JWST beam. This measurement will supply additional important data for cross correlating with the CIB to be measured by LIBRAE and expand the Euclid's reach to the greater depth and wavelength coverage available with NIRCam.

The Wide Field Infrared Survey Telescope (WFIRST) is a flagship NASA mission[8] that will provide further venues for accurate measurements of source-subtracted CIB fluctuations from its deep coverage of 2000 deg^2 of the sky in the planned wide survey mode. The survey will employ four (out of six) near-IR bands at 1, 1.3, 1.6, and 1.8 μm and will have deeper than Euclid integrations to $m_{AB} \sim 27.5$ (2.5σ). In addition, as of this writing, the mission is planned to have two extra channels centered at 0.6 and 0.87 μm. The visible channel available around 0.6 μm (J. Kruk, private communication) in the planned guest observer program would allow probing the Lyman break of source-subtracted CIB fluctuations with the WFIRST data alone, although probably from mapping a smaller area than the wide survey. The net sky area covered by WFIRST is an order of magnitude smaller than Euclid's wide survey, but would still allow probing the CIB power spectrum with subpercent statistical accuracy at arc min scales. Its deeper exposures will enable probing the evolution of the CIB clustering component at still lower shot-noise levels than with Euclid. The large area of the survey, mapped at four near-IR channels to greater depths than Euclid, will provide an opportunity for further application of the Lyman tomography and BAO study at the $6.5 \lesssim z \lesssim 15.5$ epochs.

CIBER-2 is planned to probe EBL in six bands at [0.6, 0.8, 1, 1.3, 1.6, 1.9] μm with a 28.5 cm Cassegrain telescope after removing sources to $m_{AB} \sim 19$ (1.3 μm, *J* band) over a $\sim 1° \times 2°$ FoV (Lanz *et al.*, 2014). The instrument will be flown to suborbital altitudes on board a series of sounding rockets. CIBER-2 is tasked to "explore cross correlations on both sides of the Lyman break to distinguish between low and high redshift components of the EBL" fluctuations.[9] However, Fig. 33 shows the challenges and problems when trying to achieve this goal with CIB and EBL anisotropies in such a shallow configuration where the high-*z* component appears subdominant compared to, and is much smaller than, the uncertainties in, the CIB fluctuations from remaining known galaxies. Other configurations designed to similarly shallow exposures would be subject to similar limitations.

The Spectro-Photometer for the History of the Universe, Epoch of Reionization, and Ices Explorer (SPHEREx) is a proposed NASA MIDEX mission selected for phase A study.[10] If selected further, it will employ linear variable filters to carry out an all-sky spectral survey with spectral resolution $R \simeq 41$ at [0.75–4.18] μm and $R \simeq 135$ at [4.18–5] μm. The survey will have angular resolution of 6.2$''$ and depth $m_{AB} \sim 18$–19 (5σ). Although one of the planned goals of the survey is to probe the origin of CIB fluctuations, the shallow depth, and hence the uncertainties of the substantial component of the remaining known galaxies, would preclude reliably isolating high-*z* CIB fluctuations as discussed in Sec. VI.E and illustrated in Fig. 33. Additionally, the low angular resolution of the instrument would remove a large fraction of the sky at $\sim 50\%$, on par with CIBER; this will require development and application of the correlation function tools to verify any FT-based CIB fluctuation analysis.

The Square Kilometer Array (SKA) will provide observations of the H I 21 cm line from the EoR, which can be cross correlated with the CIB to provide additional information. To first order, if galaxies were the CIB and reionization sources, one would expect a CIB 21 cm anticorrelation produced by ionized bubbles around the sources (Fernandez *et al.*, 2014; Mao, 2014). If instead CIB sources are obscured black holes from which only x rays can escape (i.e., no UV emission), the situation can be different. With their long mean free paths and efficient IGM heating, x rays could dramatically boost the 21 cm signal during the early EoR stages (Haiman, 2011; Mesinger, Ferrara, and Spiegel, 2013). The anticorrelation is the strongest when the ionization fraction is about 50%. Although there are free parameters in these models, the cross-correlation signal is rather insensitive to their variation, as many of the same parameters (such as the star formation efficiency, stellar mass, metallicity) affect both the infrared and the 21 cm line emission. Cross correlations can also reduce some of the limitations of both types of experiments, such as the lack of redshift information for CIB sources. If detected, the CIB-21 cm correlation will inform us precisely on the redshift distribution of the sources (McQuinn and

White, 2013). This will be made possible by the forthcoming SKA[11] data.

IX. OUTLOOK FOR THE FUTURE

This review summarized current observational status of the near-IR CIB anisotropy measurements and their cosmological implications. Following many new measurements and observations this novel field has recently come from a relative obscurity to significant, rapid development, to become a subject of lively scientific debate. The coming years will bring more accurate CIB fluctuation measurements with new upcoming missions. We discussed these here with a particular emphasis on the LIBRAE project which will utilize data from the Euclid dark energy mission, currently planned for launch in late 2020 or early 2021, for source-subtracted CIB measurements. To achieve decisive interpretation, one needs diffuse light measurements with experimental configurations that (1) reach deep exposures to be able to identify the potential Lyman cutoff of the high-z CIB sources, (2) combined with availability of the space-borne data in visible bands, (3) measured over a wide area to reach high-accuracy determination of the source-subtracted CIB power spectrum, and to simultaneously be able to correlate the measured CIB with (4) suitable x-ray background data (from eROSITA and Chandra) to probe the contributions from accreting BHs from nucleosynthetic sources at high z, and (5) multifrequency CMB data over large areas of the sky with low noise and high angular resolution, such as planned from the currently planned surveys (AdvACTPol and CMB-S4), to identify the condition of high-z IGM. Newly developed methodologies will enable precision science with the future CIB data.

LIST OF SYMBOLS AND ABBREVIATIONS

ACIS-I	Advanced CCD Imaging Spectrometer—Imaging arrays
ACS	Advanced Camera for Surveys
ACT	Atacama Cosmology Telescope
AEGIS-XD	All-wavelength Extended Groth Strip International Survey—X Ray, Deep
AKARI	Japanese infrared satellite
ALMA	Atacama Large Millimeter-Submillimeter Array
ASPECS	ALMA Spectroscopic Survey in the Hubble Ultra Deep Field
BAO	baryonic acoustic oscillation
BH	black hole
CCD	charge-coupled device
CIB	cosmic infrared background
CIBER	Cosmic Infrared Background Experiment
CLEAN	a deconvolution algorithm
CMB	cosmic microwave background
COB	cosmic optical background
COBE	Cosmic Background Explorer

COSMOS	Cosmological Evolution Survey
CXB	cosmic x-ray background
DAOPHOT	Dominion Astrophysical Observatory stellar photometry package
DCBH	direct collapse black hole
DE	dark energy
DGL	diffuse Galactic light
DIRBE	Diffuse Infrared Background Experiment (on COBE)
DM	dark matter
EBL	extragalactic background light
EoR	epoch of reionization
eRASS	eRosita All-Sky Survey
eROSITA	Extended Roentgen Survey with an Imaging Telescope Array
FFT	fast Fourier transform
FIRAS	Far-Infrared Absolute Spectrophotometer
FoV	field of view
FT	Fourier transform
FWHM	full width at half maximum
GOODS	Great Observatories Origins Deep Survey
GP	Gunn-Peterson (effect)
GW	gravitational wave
H I	neutral hydrogen
H II	ionized hydrogen
HFE	high faint end (of HRK12 reconstruction)
HPD	half power diameter
HRK12	Helgason, Ricotti, and Kashlinsky (2012)
HST	Hubble Space Telescope
HZ	Harrison-Zeldovich
ICL	intracluster light
IGM	intergalactic medium
IHL	intrahalo light
IMF	initial mass function
IRAC	Infrared Array Camera
IRC	Infrared Camera (on AKARI)
IRTS	Infrared Telescope in Space
IRX	infrared excess
ISM	interstellar medium
JWST	James Webb Space Telescope
KSZ	kinematic SZ (effect)
LBG	Lyman-break galaxy
ΛCDM	lambda cold dark matter
LF	luminosity function
LFE	low-faint end (of HRK12 reconstruction)
LIBRAE	Looking at Infrared Background Radiation Anisotropies with Euclid
LIGO	Laser Interferometer GW Observatory
LW	Lyman-Werner
NEP	north ecliptic pole
NICMOS	Near-Infrared Camera and Multiobject Spectrometer (on HST)
NIRCam	Near-Infrared Camera (on JWST)

NISP	Near-Infrared Spectrometer and Photometer (on Euclid)
OH glow	OH (molecular) emission
PBH	primordial black hole
PIB	particle internal background
PSF	point-spread function
QSOs	quasistellar objects
ROSAT	Röntgensatellit
SDSS	Sloan Digital Sky Survey
SED	spectral energy distribution
SEDS	Spitzer extended deep survey
SEP	south ecliptic pole
SMBH	supermassive black hole
SPT	South Pole Telescope
SZ	Sunyaev-Zeldovich (effect)
TSZ	thermal SZ (effect)
VIS	Visible Instrument (on Euclid)
WFC3	HST Wide Field Camera 3
WMAP	Wilkinson Microwave Anisotropy Probe
XMM	X-ray Multimirror Mission
2MASS	Two-Micron All Sky Survey

REFERENCES

Abadie, J., *et al.*, 2010, Classical Quantum Gravity **27**, 173001.
Abbott, B. P., *et al.*, 2016a, Astrophys. J. Lett. **818**, L22.
Abbott, B. P., *et al.*, 2016b, Phys. Rev. X **6**, 041015.
Abbott, B. P., *et al.*, 2016c, Phys. Rev. D **93**, 122003.
Abbott, B. P., *et al.*, 2016d, Phys. Rev. Lett. **116**, 241103.

Abbott, B. P., *et al.*, 2016e, Phys. Rev. Lett. **116**, 061102.
Abbott, B. P., *et al.*, 2016f, Living Rev. Relativity **19**, 1.
Abbott, B. P., *et al.* (LIGO Scientific and Virgo Collaboration), 2017, Phys. Rev. Lett. **118**, 221101.
Abbott, L. F., and M. B. Wise, 1984, Astrophys. J. **282**, L47.
Abel, T., G. L. Bryan, and M. L. Norman, 2002, Science **295**, 93.
Abitbol, M. H., *et al.*, 2017, arXiv:1706.02464.
Abraham, P., C. Leinert, and D. Lemke, 1997, Astron. Astrophys. **328**, 702 [http://adsabs.harvard.edu/abs/1997A%26A...328..702A].
Abramowski, A., *et al.* (H. E. S. S. Collaboration), 2013, Astron. Astrophys. **550**, A4.
Ackermann, M., *et al.*, 2012, Science **338**, 1190.
Ade, P. A. R., *et al.* (Planck Collaboration), 2014, Astron. Astrophys. **571**, A16.
Ade, P. A. R., *et al.* (Planck Collaboration), 2016, Astron. Astrophys. **594**, A13.
Afshordi, N., P. McDonald, and D. N. Spergel, 2003, Astrophys. J. Lett. **594**, L71.
Agarwal, B., C. Dalla Vecchia, J. L. Johnson, S. Khochfar, and J.-P. Paardekooper, 2014, Mon. Not. R. Astron. Soc. **443**, 648.
Agarwal, B., S. Khochfar, J. L. Johnson, E. Neistein, C. Dalla Vecchia, and M. Livio, 2012, Mon. Not. R. Astron. Soc. **425**, 2854.
Aghanim, N., F. X. Desert, J. L. Puget, and R. Gispert, 1996, Astron. Astrophys. **311**, 1 [http://adsabs.harvard.edu/abs/1996A%26A...311....1A].
Aharonian, F., *et al.*, 2006, Nature (London) **440**, 1018.
Ahnen, M. L., *et al.*, 2016, Astron. Astrophys. **590**, A24.
Alexander, T., and P. Natarajan, 2014, Science **345**, 1330.
Ali-Haïmoud, Y., and M. Kamionkowski, 2017, Phys. Rev. D **95**, 043534.
Aloni, D., K. Blum, and R. Flauger, **2017**, J. Cosmol. Astropart. Phys. 05, 017.
Alpher, R. A., 1948, Phys. Rev. **74**, 1577.
Alpher, R. A., and R. C. Herman, 1948, Phys. Rev. **74**, 1737.
Alvarez, M. A., J. H. Wise, and T. Abel, 2009, Astrophys. J. Lett. **701**, L133.
Amendola, L., *et al.*, 2018, Living Rev. Relativity **21**, 2.
Aoki, W., N. Tominaga, T. C. Beers, S. Honda, and Y. S. Lee, 2014, Science **345**, 912.
Arai, T., *et al.*, 2015, Astrophys. J. **806**, 69.
Arendt, R. G., D. J. Fixsen, and S. H. Moseley, 2000, Astrophys. J. **536**, 500.
Arendt, R. G., D. J. Fixsen, and S. H. Moseley, 2002, in *Astronomical Data Analysis Software and Systems XI*, Astronomical Society of the Pacific Conference Series, Vol. 281, edited by D. A. Bohlender, D. Durand, and T. H. Handley (Astronomical Society of the Pacific, San Francisco), p. 217.
Arendt, R. G., A. Kashlinsky, S. H. Moseley, and J. Mather, 2010, Astrophys. J. Suppl. Ser. **186**, 10.
Arendt, R. G., A. Kashlinsky, S. H. Moseley, and J. Mather, 2016, Astrophys. J. **824**, 26.
Arendt, R. G., *et al.*, 1998, Astrophys. J. **508**, 74.
Ashby, M. L. N., *et al.*, 2013, Astrophys. J. **769**, 80.
Ashby, M. L. N., *et al.*, 2015, Astrophys. J. Suppl. Ser. **218**, 33.
Atrio-Barandela, F., and A. G. Doroshkevich, 1994, Astrophys. J. **420**, 26.
Atrio-Barandela, F., and A. Kashlinsky, 2014, Astrophys. J. Lett. **797**, L26.
Aubourg, É., *et al.* (BOSS Collaboration), 2015, Phys. Rev. D **92**, 123516.
Ballantyne, D. R., Y. Shi, G. H. Rieke, J. L. Donley, C. Papovich, and J. R. Rigby, 2006, Astrophys. J. **653**, 1070.

Bañados, E., *et al.*, 2016, Astrophys. J. Suppl. Ser. **227**, 11.

Bardeen, J. M., J. R. Bond, N. Kaiser, and A. S. Szalay, 1986, Astrophys. J. **304**, 15.

Barmby, P., *et al.*, 2004, Astrophys. J. Suppl. Ser. **154**, 97.

Battaglia, N., A. Natarajan, H. Trac, R. Cen, and A. Loeb, 2013, Astrophys. J. **776**, 83.

Becker, G. D., J. S. Bolton, M. G. Haehnelt, and W. L. W. Sargent, 2011, Mon. Not. R. Astron. Soc. **410**, 1096.

Becker, G. D., J. S. Bolton, and A. Lidz, 2015, Pub. Astron. Soc. Aust. **32**, e045.

Beckwith, S. V. W., *et al.*, 2006, Astron. J. **132**, 1729.

Beelen, A., P. Cox, D. J. Benford, C. D. Dowell, A. Kovács, F. Bertoldi, A. Omont, and C. L. Carilli, 2006, Astrophys. J. **642**, 694.

Begelman, M. C., and M. J. Rees, 1978, Mon. Not. R. Astron. Soc. **185**, 847.

Begelman, M. C., M. Volonteri, and M. J. Rees, 2006, Mon. Not. R. Astron. Soc. **370**, 289.

Bennett, C. L., *et al.*, 2013, Astrophys. J. Suppl. Ser. **208**, 20.

Bernardi, M., *et al.*, 2003, Astron. J. **125**, 32.

Bernstein, R. A., 2007, Astrophys. J. **666**, 663.

Bianchi, S., and R. Schneider, 2007, Mon. Not. R. Astron. Soc. **378**, 973.

Bird, S., I. Cholis, J. B. Muñoz, Y. Ali-Haïmoud, M. Kamionkowski, E. D. Kovetz, A. Raccanelli, and A. G. Riess, 2016, Phys. Rev. Lett. **116**, 201301.

Biteau, J., and D. A. Williams, 2015, Astrophys. J. **812**, 60.

Bochanski, J. J., S. L. Hawley, K. R. Covey, A. A. West, I. N. Reid, D. A. Golimowski, and Ž. Ivezić, 2010, Astron. J. **139**, 2679.

Bock, J., *et al.*, 2013, Astrophys. J. Suppl. Ser. **207**, 32.

Boera, E., M. T. Murphy, G. D. Becker, and J. S. Bolton, 2014, Mon. Not. R. Astron. Soc. **441**, 1916.

Bolton, J. S., G. D. Becker, M. G. Haehnelt, and M. Viel, 2014, Mon. Not. R. Astron. Soc. **438**, 2499.

Bolton, J. S., G. D. Becker, S. Raskutti, J. S. B. Wyithe, M. G. Haehnelt, and W. L. W. Sargent, 2012, Mon. Not. R. Astron. Soc. **419**, 2880.

Bolton, J. S., and M. G. Haehnelt, 2007, Mon. Not. R. Astron. Soc. **382**, 325.

Bolton, J. S., and M. G. Haehnelt, 2013, Mon. Not. R. Astron. Soc. **429**, 1695.

Bond, J. R., B. J. Carr, and C. J. Hogan, 1986, Astrophys. J. **306**, 428.

Bond, J. R., and G. Efstathiou, 1984, Astrophys. J. **285**, L45.

Bouwens, R., *et al.*, 2016, Astrophys. J. **833**, 72.

Bouwens, R. J., G. D. Illingworth, P. A. Oesch, J. Caruana, B. Holwerda, R. Smit, and S. Wilkins, 2015, Astrophys. J. **811**, 140.

Bouwens, R. J., *et al.*, 2010, Astrophys. J. Lett. **709**, L133.

Bouwens, R. J., *et al.*, 2011, Astrophys. J. **737**, 90.

Brandt, T. D., 2016, Astrophys. J. Lett. **824**, L31.

Brandt, T. D., and B. T. Draine, 2012, Astrophys. J. **744**, 129.

Brandt, W. N., and D. M. Alexander, 2015, Astron. Astrophys. Rev. **23**, 1.

Brandt, W. N., and G. Hasinger, 2005, Annu. Rev. Astron. Astrophys. **43**, 827.

Brightman, M., and Y. Ueda, 2012, Mon. Not. R. Astron. Soc. **423**, 702.

Broderick, A. E., P. Chang, and C. Pfrommer, 2012, Astrophys. J. **752**, 22.

Bromm, V., 2013a, Rep. Prog. Phys. **76**, 112901.

Bromm, V., 2013b, in *The Intriguing Life of Massive Galaxies*, IAU Symposium, Vol. 295, edited by D. Thomas, A. Pasquali, and I. Ferreras (Cambridge University Press, Cambridge), pp. 3–12.

Bromm, V., P. S. Coppi, and R. B. Larson, 1999, Astrophys. J. Lett. **527**, L5.

Bromm, V., R. P. Kudritzki, and A. Loeb, 2001, Astrophys. J. **552**, 464.

Bromm, V., and R. B. Larson, 2004, Annu. Rev. Astron. Astrophys. **42**, 79.

Bromm, V., and A. Loeb, 2003, Astrophys. J. **596**, 34.

Bromm, V., and N. Yoshida, 2011, Annu. Rev. Astron. Astrophys. **49**, 373.

Capak, P. L., *et al.*, 2015, Nature (London) **522**, 455.

Cappelluti, N., R. Arendt, A. Kashlinsky, Y. Li, G. Hasinger, K. Helgason, M. Urry, P. Natarajan, and A. Finoguenov, 2017, Astrophys. J. Lett. **847**, L11.

Cappelluti, N., A. Kashlinsky, R. G. Arendt, A. Comastri, G. G. Fazio, A. Finoguenov, G. Hasinger, J. C. Mather, T. Miyaji, and S. H. Moseley, 2013, Astrophys. J. **769**, 68.

Cappelluti, N., *et al.*, 2012, Mon. Not. R. Astron. Soc. **427**, 651.

Cappelluti, N., *et al.*, 2017, Astrophys. J. **837**, 19.

Carr, B., F. Kühnel, and M. Sandstad, 2016, Phys. Rev. D **94**, 083504.

Carr, B. J., 1975, Astrophys. J. **201**, 1.

Chary, R.-R., A. Cooray, and I. Sullivan, 2008, Astrophys. J. **681**, 53–57.

Choudhury, T. R., and A. Ferrara, 2006, Mon. Not. R. Astron. Soc. Lett. **371**, L55.

Ciardi, B., and A. Ferrara, 2005, Space Sci. Rev. **116**, 625.

Ciardi, B., A. Ferrara, and T. Abel, 2000, Astrophys. J. **533**, 594.

Clesse, S., and J. García-Bellido, 2015, Phys. Rev. D **92**, 023524.

Clesse, S., and J. García-Bellido, 2017, Phys. Dark Universe **15**, 142.

Comastri, A., R. Gilli, A. Marconi, G. Risaliti, and M. Salvati, 2015, Astron. Astrophys. **574**, L10.

Comastri, A., G. Setti, G. Zamorani, and G. Hasinger, 1995, Astron. Astrophys. **296**, 1 [http://adsabs.harvard.edu/abs/1995A%26A.. .296....1C].

Condon, J. J., 1974, Astrophys. J. **188**, 279.

Cooray, A., J. J. Bock, B. Keatin, A. E. Lange, and T. Matsumoto, 2004, Astrophys. J. **606**, 611.

Cooray, A., Y. Gong, J. Smidt, and M. G. Santos, 2012, Astrophys. J. **756**, 92.

Cooray, A., and R. Sheth, 2002, Phys. Rep. **372**, 1.

Cooray, A., I. Sullivan, R.-R. Chary, J. J. Bock, M. Dickinson, H. C. Ferguson, B. Keating, A. Lange, and E. L. Wright, 2007, Astrophys. J. Lett. **659**, L91.

Cooray, A., and N. Yoshida, 2004, Mon. Not. R. Astron. Soc. **351**, L71.

Cooray, A., *et al.*, 2009, in *Astro2010: The Astronomy and Astrophysics Decadal Survey*, Science White Papers, No. 54 [http://adsabs.harvard.edu/abs/2009astro2010S..54C].

Cooray, A., *et al.*, 2012, Nature (London) **490**, 514.

Cowie, L. L., A. J. Barger, and G. Hasinger, 2012, Astrophys. J. **748**, 50.

da Cunha, E., *et al.*, 2013, Astrophys. J. **766**, 13.

Davis, M., and P. J. E. Peebles, 1983, Astrophys. J. **267**, 465.

de Bernardis, P., *et al.*, 2000, Nature (London) **404**, 955.

De Rossi, M. E., and V. Bromm, 2017, Mon. Not. R. Astron. Soc. **465**, 3668.

Dicke, R. H., P. J. E. Peebles, P. G. Roll, and D. T. Wilkinson, 1965, Astrophys. J. **142**, 414.

Dickinson, M., 2008, in American Astronomical Society Meeting Abstracts #212, *Bulletin of the American Astronomical Society*, Vol. 40, p. 251.

Dijkstra, M., A. Ferrara, and A. Mesinger, 2014, Mon. Not. R. Astron. Soc. **442**, 2036.

Donnerstein, R. L., 2015, Mon. Not. R. Astron. Soc. **449**, 1291.

Driver, S. P., S. K. Andrews, L. J. Davies, A. S. G. Robotham, A. H. Wright, R. A. Windhorst, S. Cohen, K. Emig, R. A. Jansen, and L. Dunne, 2016, Astrophys. J. **827**, 108.

Dunlop, J. S., 2013, in *The First Galaxies*, Astrophysics and Space Science Library, Vol. 396, edited by T. Wiklind, B. Mobasher, and V. Bromm (Springer, Heidelberg), p. 223.

Dupuy, T. J., and M. C. Liu, 2012, Astrophys. J. Suppl. Ser. **201**, 19.

Dwek, E., R. G. Arendt, and F. Krennrich, 2005, Astrophys. J. **635**, 784.

Dwek, E., F. Krennrich, and R. G. Arendt, 2005, Astrophys. J. **634**, 155.

Eisenstein, D. J., and W. Hu, 1998, Astrophys. J. **496**, 605.

Eisenstein, D. J., and W. Hu, 1999, Astrophys. J. **511**, 5.

Eisenstein, D. J., and A. Loeb, 1995, Astrophys. J. **443**, 11.

Essey, W., O. E. Kalashev, A. Kusenko, and J. F. Beacom, 2010, Phys. Rev. Lett. **104**, 141102.

Essey, W., and A. Kusenko, 2010, Astropart. Phys. **33**, 81.

Evoli, C., and A. Ferrara, 2011, Mon. Not. R. Astron. Soc. **413**, 2721.

Fan, X., C. L. Carilli, and B. Keating, 2006, Annu. Rev. Astron. Astrophys. **44**, 415.

Fan, X., M. A. Strauss, R. H. Becker, R. L. White, J. E. Gunn, G. R. Knapp, G. T. Richards, D. P. Schneider, J. Brinkmann, and M. Fukugita, 2006, Astron. J. **132**, 117.

Farr, W. M., S. Stevenson, M. C. Miller, I. Mandel, B. Farr, and A. Vecchio, 2017, Nature (London) **548**, 426.

Fazio, G. G., *et al.*, 2004a, Astrophys. J. Suppl. Ser. **154**, 39.

Fazio, G. G., *et al.*, 2004b, Astrophys. J. Suppl. Ser. **154**, 10.

Fernandez, E. R., I. T. Iliev, E. Komatsu, and P. R. Shapiro, 2012, Astrophys. J. **750**, 20.

Fernandez, E. R., and E. Komatsu, 2006, Astrophys. J. **646**, 703.

Fernandez, E. R., E. Komatsu, I. T. Iliev, and P. R. Shapiro, 2010, Astrophys. J. **710**, 1089.

Fernandez, E. R., S. Zaroubi, I. T. Iliev, G. Mellema, and V. Jelić, 2014, Mon. Not. R. Astron. Soc. **440**, 298.

Ferrara, A., 2012, in *American Institute of Physics Conference Series*, Vol. 1480, edited by M. Umemura and K. Omukai (AIP, Melville, NY), pp. 317–324.

Ferrara, A., F. Haardt, and R. Salvaterra, 2013, Mon. Not. R. Astron. Soc. **434**, 2600.

Ferrara, A., B. Nath, S. K. Sethi, and Y. Shchekinov, 1999, Mon. Not. R. Astron. Soc. **303**, 301.

Ferrara, A., S. Salvadori, B. Yue, and D. Schleicher, 2014, Mon. Not. R. Astron. Soc. **443**, 2410.

Ferrara, A., S. Viti, and C. Ceccarelli, 2016, Mon. Not. R. Astron. Soc. Lett. **463**, L112.

Ferrarese, L., and D. Merritt, 2000, Astrophys. J. Lett. **539**, L9.

Finkelstein, S. L., *et al.*, 2015, Astrophys. J. **810**, 71.

Fiore, F., *et al.*, 2012, Astron. Astrophys. **537**, A16.

Fisher, R., 1915, Biometrika **10**, 507.

Fixsen, D. J., 2009, Astrophys. J. **707**, 916.

Fixsen, D. J., E. Dwek, J. C. Mather, C. L. Bennett, and R. A. Shafer, 1998, Astrophys. J. **508**, 123.

Fixsen, D. J., S. H. Moseley, and R. G. Arendt, 2000, Astrophys. J. Suppl. Ser. **128**, 651.

Fontana, A., *et al.*, 2014, Astron. Astrophys. **570**, A11.

Fotopoulou, S., *et al.*, 2016, Astron. Astrophys. **587**, A142.

Furlanetto, S. R., and S. P. Oh, 2009, Astrophys. J. **701**, 94.

Furlanetto, S. R., S. P. Oh, and F. H. Briggs, 2006, Phys. Rep. **433**, 181.

Gall, C., J. Hjorth, and A. C. Andersen, 2011, Astron. Astrophys. Rev. **19**, 43.

García-Bellido, J., A. Linde, and D. Wands, 1996, Phys. Rev. D **54**, 6040.

Gardner, J. P., L. L. Cowie, and R. J. Wainscoat, 1993, Astrophys. J. Lett. **415**, L9.

Gebhardt, K., *et al.*, 2000, Astrophys. J. **539**, L13.

George, E. M., *et al.*, 2015, Astrophys. J. **799**, 177.

Giacconi, R., H. Gursky, F. R. Paolini, and B. B. Rossi, 1962, Phys. Rev. Lett. **9**, 439.

Gilli, R., A. Comastri, and G. Hasinger, 2007, Astron. Astrophys. **463**, 79.

Gilli, R., G. Risaliti, and M. Salvati, 1999, Astron. Astrophys. **347**, 424 [http://adsabs.harvard.edu/abs/1999A%26A...347..424G].

Glazebrook, K., J. A. Peacock, C. A. Collins, and L. Miller, 1994, Mon. Not. R. Astron. Soc. **266**, 65.

Gong, Y., A. Cooray, K. Mitchell-Wynne, X. Chen, M. Zemcov, and J. Smidt, 2016, Astrophys. J. **825**, 104.

Górski, K. M., E. Hivon, A. J. Banday, B. D. Wandelt, F. K. Hansen, M. Reinecke, and M. Bartelmann, 2005, Astrophys. J. **622**, 759.

Gould, R. J., and G. P. Schréder, 1967, Phys. Rev. **155**, 1404.

Goulding, A. D., *et al.*, 2012, Astrophys. J. Suppl. Ser. **202**, 6.

Graham, A. W., and N. Scott, 2013, Astrophys. J. **764**, 151.

Greenhouse, M. A., S. W. Benson, R. D. Falck, D. J. Fixsen, J. P. Gardner, J. B. Garvin, J. W. Kruk, S. R. Oleson, and H. A. Thronson, 2012, in Space Telescopes and Instrumentation 2012: Optical, Infrared, and Millimeter Wave, *Proc. SPIE* Vol. 8442 (SPIE–International Society for Optical Engineering, Bellingham, WA), p. 844214.

Greig, B., and A. Mesinger, 2017, Mon. Not. R. Astron. Soc. **465**, 4838.

Gruzinov, A., and W. Hu, 1998, Astrophys. J. **508**, 435.

Gunn, J. E., and B. A. Peterson, 1965, Astrophys. J. **142**, 1633.

Guth, A. H., 1981, Phys. Rev. D **23**, 347.

Guth, A. H., and S.-Y. Pi, 1982, Phys. Rev. Lett. **49**, 1110.

Haardt, F., and P. Madau, 2012, Astrophys. J. **746**, 125.

Haiman, Z., 2011, Nature (London) **472**, 47.

Hasinger, G., 2008, Astron. Astrophys. **490**, 905.

Hauser, M. G., and E. Dwek, 2001, Annu. Rev. Astron. Astrophys. **39**, 249.

Hauser, M. G., *et al.*, 1998, Astrophys. J. **508**, 25.

Hawkins, M. R. S., 1993, Nature (London) **366**, 242.

Heinrich, C. H., V. Miranda, and W. Hu, 2017, Phys. Rev. D **95**, 023513.

Helgason, K., N. Cappelluti, G. Hasinger, A. Kashlinsky, and M. Ricotti, 2014, Astrophys. J. **785**, 38.

Helgason, K., and A. Kashlinsky, 2012, Astrophys. J. Lett. **758**, L13.

Helgason, K., and E. Komatsu, 2017, Mon. Not. R. Astron. Soc. Lett. **467**, L36.

Helgason, K., M. Ricotti, and A. Kashlinsky, 2012, Astrophys. J. **752**, 113.

Helgason, K., M. Ricotti, A. Kashlinsky, and V. Bromm, 2016, Mon. Not. R. Astron. Soc. **455**, 282.

Hemantha, M. D. P., Y. Wang, and C.-H. Chuang, 2014, Mon. Not. R. Astron. Soc. **445**, 3737.

Hinshaw, G., *et al.*, 2013, Astrophys. J. Suppl. Ser. **208**, 19.

Hirashita, H., and A. Ferrara, 2002, Mon. Not. R. Astron. Soc. **337**, 921.

Högbom, J. A., 1974, Astron. Astrophys. Suppl. Ser. **15**, 417 [http://adsabs.harvard.edu/abs/1974A%26AS...15..417H].

Horowitz, B., 2016, arXiv:1612.07264.

Hoyle, F., 1953, Astrophys. J. **118**, 513.

Hu, W., 2000, Astrophys. J. **529**, 12.

Hu, W., 2001, Phys. Rev. D **65**, 023003.

Hu, W., and M. White, 1997, New Astron. **2**, 323.

Hui, L., and Z. Haiman, 2003, Astrophys. J. **596**, 9.

Ishigaki, M., R. Kawamata, M. Ouchi, M. Oguri, and K. Shimasaku, 2018, Astrophys. J. **854**, 73.

Jedamzik, K., 1997, Phys. Rev. D **55**, R5871.

Jensen, L. G., and A. S. Szalay, 1986, Astrophys. J. **305**, L5.

Jeon, M., A. H. Pawlik, V. Bromm, and M. Milosavljević, 2014, Mon. Not. R. Astron. Soc. **440**, 3778.

Johnson, J. L., V. C. Dalla, and S. Khochfar, 2013, Mon. Not. R. Astron. Soc. **428**, 1857.

Johnson, J. L., and S. Khochfar, 2011, Astrophys. J. **743**, 126.

Kaiser, N., 1984, Astrophys. J. **284**, L9.

Kashlinsky, A., 1982, Mon. Not. R. Astron. Soc. **200**, 585.

Kashlinsky, A., 1991, Astrophys. J. **376**, L5.

Kashlinsky, A., 1998, Astrophys. J. **492**, 1.

Kashlinsky, A., 2005a, Phys. Rep. **409**, 361.

Kashlinsky, A., 2005b, Astrophys. J. Lett. **633**, L5.

Kashlinsky, A., 2007, arXiv:astro-ph/0701147.

Kashlinsky, A., 2016, Astrophys. J. Lett. **823**, L25.

Kashlinsky, A., R. Arendt, J. P. Gardner, J. C. Mather, and S. H. Moseley, 2004, Astrophys. J. **608**, 1.

Kashlinsky, A., R. G. Arendt, M. L. N. Ashby, G. G. Fazio, J. Mather, and S. H. Moseley, 2012, Astrophys. J. **753**, 63.

Kashlinsky, A., R. G. Arendt, F. Atrio-Barandela, and K. Helgason, 2015, Astrophys. J. Lett. **813**, L12.

Kashlinsky, A., R. G. Arendt, J. Mather, and S. H. Moseley, 2005, Nature (London) **438**, 45.

Kashlinsky, A., R. G. Arendt, J. Mather, and S. H. Moseley, 2007a, Astrophys. J. Lett. **666**, L1.

Kashlinsky, A., R. G. Arendt, J. Mather, and S. H. Moseley, 2007b, Astrophys. J. Lett. **654**, L5.

Kashlinsky, A., R. G. Arendt, J. Mather, and S. H. Moseley, 2007c, Astrophys. J. Lett. **654**, L1.

Kashlinsky, A., and D. Band, 2007, in *The First GLAST Symposium*, American Institute of Physics Conference Series, Vol. 921, edited by S. Ritz, P. Michelson, and C. A. Meegan (AIP, Melville, NY), pp. 243–245.

Kashlinsky, A., J. C. Mather, K. Helgason, R. G. Arendt, V. Bromm, and S. H. Moseley, 2015, Astrophys. J. **804**, 99.

Kashlinsky, A., J. C. Mather, and S. Odenwald, 1996, Astrophys. J. Lett. **473**, L9.

Kashlinsky, A., J. C. Mather, S. Odenwald, and M. G. Hauser, 1996, Astrophys. J. **470**, 681.

Kashlinsky, A., and S. Odenwald, 2000, Astrophys. J. **528**, 74.

Kashlinsky, A., S. Odenwald, J. Mather, M. F. Skrutskie, and R. M. Cutri, 2002, Astrophys. J. Lett. **579**, L53.

Kashlinsky, A., and M. J. Rees, 1983, Mon. Not. R. Astron. Soc. **205**, 955.

Kawara, K., Y. Matsuoka, K. Sano, T. D. Brandt, H. Sameshima, K. Tsumura, S. Oyabu, and N. Ienaka, 2017, Publ. Astron. Soc. Jpn. **69**, 31.

Kawasaki, M., A. Kusenko, L. Pearce, and L. Yang, 2017, Phys. Rev. D **95**, 103006.

Kazanas, D., 1980, Astrophys. J. **241**, L59.

Kazanas, D., 2015, in *The Formation and Disruption of Black Hole Jets*, Astrophysics and Space Science Library, Vol. 414, edited by I. Contopoulos, D. Gabuzda, and N. Kylafis (Springer, Heidelberg), p. 207.

Keenan, R. C., A. J. Barger, L. L. Cowie, and W.-H. Wang, 2010, Astrophys. J. **723**, 40.

Kelsall, T., *et al.*, 1998, Astrophys. J. **508**, 44.

Knox, L., R. Scoccimarro, and S. Dodelson, 1998, Phys. Rev. Lett. **81**, 2004.

Knudsen, K. K., D. Watson, D. Frayer, L. Christensen, A. Gallazzi, M. J. Michalowski, J. Richard, and J. Zavala, 2017, Mon. Not. R. Astron. Soc. **466**, 138.

Kocevski, D. D., 2017, Astrophys. J. (to be published).

Kocevski, D. D., *et al.*, 2015, Astrophys. J. **814**, 104.

Kogut, A., *et al.*, 2003, Astrophys. J. Suppl. Ser. **148**, 161.

Kohri, K., and H. Kodama, 2017, Phys. Rev. D **96**, 051701.

Kormendy, J., and L. C. Ho, 2013, Annu. Rev. Astron. Astrophys. **51**, 511.

Kormendy, J., and D. Richstone, 1995, Annu. Rev. Astron. Astrophys. **33**, 581.

Lacki, B. C., 2015, Mon. Not. R. Astron. Soc. Lett. **448**, L20.

Lange, A. E., *et al.*, 2001, Phys. Rev. D **63**, 042001.

Lanz, A., *et al.*, 2014, in Space Telescopes and Instrumentation 2014: Optical, Infrared, and Millimeter Wave, *Proc. SPIE* Vol. 9143 (SPIE–International Society for Optical Engineering, Bellingham, WA), p. 91433N.

Laporte, N., R. S. Ellis, F. Boone, F. E. Bauer, D. Quénard, G. W. Roberts-Borsani, R. Pelló, I. Pérez-Fournon, and A. Streblyanska, 2017, Astrophys. J. Lett. **837**, L21.

Latif, M. A., and A. Ferrara, 2016, Pub. Astron. Soc. Aust. **33**, e051.

Latif, M. A., D. R. G. Schleicher, W. Schmidt, and J. Niemeyer, 2013, Mon. Not. R. Astron. Soc. **433**, 1607.

Laureijs, R., *et al.*, 2011, arXiv:1110.3193.

Laureijs, R., *et al.*, 2014, in Space Telescopes and Instrumentation 2014: Optical, Infrared, and Millimeter Wave, *Proc. SPIE* Vol. 9143 (SPIE–International Society for Optical Engineering, Bellingham, WA), p. 91430H.

Lehmer, B. D., *et al.*, 2012, Astrophys. J. **752**, 46.

Leinert, C., *et al.*, 1998, Astron. Astrophys. Suppl. Ser. **127**, 1.

Levenson, L. R., and E. L. Wright, 2008, Astrophys. J. **683**, 585.

Lewis, A., 2008, Phys. Rev. D **78**, 023002.

Lidz, A., and M. Malloy, 2014, Astrophys. J. **788**, 175.

Limber, D. N., 1953, Astrophys. J. **117**, 134.

Lin, Y.-T., and J. J. Mohr, 2004, Astrophys. J. **617**, 879.

Lin, Y.-T., J. J. Mohr, and S. A. Stanford, 2004, Astrophys. J. **610**, 745.

Linde, A. D., 1982, Phys. Lett. B **108**, 389.

Liu, H., T. R. Slatyer, and J. Zavala, 2016, Phys. Rev. D **94**, 063507.

Loeb, A., and F. A. Rasio, 1994, Astrophys. J. **432**, 52.

Lupi, A., M. Colpi, B. Devecchi, G. Galanti, and M. Volonteri, 2014, Mon. Not. R. Astron. Soc. **442**, 3616.

Mack, K. J., J. P. Ostriker, and M. Ricotti, 2007, Astrophys. J. **665**, 1277.

Madau, P., F. Haardt, and M. Dotti, 2014, Astrophys. J. Lett. **784**, L38.

Madau, P., and A. Meiksin, 1994, Astrophys. J. Lett. **433**, L53.

Madau, P., and L. Pozzetti, 2000, Mon. Not. R. Astron. Soc. **312**, L9.

Magorrian, J., *et al.*, 1998, Astron. J. **115**, 2285.

Maihara, T., *et al.*, 2001, Publ. Astron. Soc. Jpn. **53**, 25.

Mao, X.-C., 2014, Astrophys. J. **790**, 148.

Marconi, A., and L. K. Hunt, 2003, Astrophys. J. Lett. **589**, L21.

Marconi, A., G. Risaliti, R. Gilli, L. K. Hunt, R. Maiolino, and M. Salvati, 2004, Mon. Not. R. Astron. Soc. **351**, 169.

Marshall, F. E., E. A. Boldt, S. S. Holt, R. B. Miller, R. F. Mushotzky, L. A. Rose, R. E. Rothschild, and P. J. Serlemitsos, 1980, Astrophys. J. **235**, 4.

Mather, J. C., *et al.*, 1990, Astrophys. J. **354**, L37.

Matsumoto, T., M. G. Kim, J. Pyo, and K. Tsumura, 2015, Astrophys. J. **807**, 57.

Matsumoto, T., S. Matsuura, H. Murakami, M. Tanaka, M. Freund, M. Lim, M. Cohen, M. Kawada, and M. Noda, 2005, Astrophys. J. **626**, 31.

Matsumoto, T., H. J. Seo, W.-S. Jeong, H. M. Lee, S. Matsuura, H. Matsuhara, S. Oyabu, J. Pyo, and T. Wada, 2011, Astrophys. J. **742**, 124.

Matsuura, S., *et al.*, 2011, Astrophys. J. **737**, 2.

Matsuura, S., *et al.*, 2017, Astrophys. J. **839**, 7.

Mattila, K., K. Lehtinen, P. Väisänen, G. von Appen-Schnur, and C. Leinert, 2017, Mon. Not. R. Astron. Soc. **470**, 2133.

Mattila, K., P. Väisänen, K. Lehtinen, G. von Appen-Schnur, and C. Leinert, 2017, Mon. Not. R. Astron. Soc. **470**, 2152.

Matuura, S., H. Yano, D. Yonetoku, R. Funase, O. Mori, and Y. Shirasawa (Solar Sail Working Group), 2014, Transactions of the Japan Society for Aeronautical and Space Sciences, Aerospace Technology Japan **12**, Tr_1.

McDonald, P., J. Miralda-Escudé, M. Rauch, W. L. W. Sargent, T. A. Barlow, and R. Cen, 2003, Astrophys. J. **598**, 712.

McDowell, J. C., 1986, Mon. Not. R. Astron. Soc. **223**, 763.

McQuinn, M., and M. White, 2013, Mon. Not. R. Astron. Soc. **433**, 2857.

Merloni, A., 2004, Mon. Not. R. Astron. Soc. **353**, 1035.

Merloni, A., *et al.*, 2012, arXiv:1209.3114.

Merritt, D., and L. Ferrarese, 2001, Astrophys. J. **547**, 140.

Mesinger, A., 2016, in *Understanding the Epoch of Cosmic Reionization: Challenges and Progress*, Astrophysics and Space Science Library, Vol. 423, edited by A. Mesinger (Springer, Heidelberg).

Mesinger, A., A. Ferrara, and D. S. Spiegel, 2013, Mon. Not. R. Astron. Soc. **431**, 621.

Mesinger, A., M. McQuinn, and D. N. Spergel, 2012, Mon. Not. R. Astron. Soc. **422**, 1403.

Meszaros, P., 1974, Astron. Astrophys. **37**, 225 [http://adsabs.harvard.edu/abs/1974A%26A....37..225M].

Meszaros, P., 1975, Astron. Astrophys. **38**, 5 [http://adsabs.harvard.edu/abs/1975A%26A....38....5M].

Meurer, G. R., T. M. Heckman, and D. Calzetti, 1999, Astrophys. J. **521**, 64.

Michalowski, M. J., E. J. Murphy, J. Hjorth, D. Watson, C. Gall, and J. S. Dunlop, 2010, Astron. Astrophys. **522**, A15.

Mihos, J. C., 2016, in The General Assembly of Galaxy Halos: Structure, Origin and Evolution, *IAU Symposium*, Vol. 317, edited by A. Bragaglia, M. Arnaboldi, M. Rejkuba, and D. Romano (Cambridge University Press, Cambridge), pp. 27–34.

Mihos, J. C., P. Harding, J. Feldmeier, and H. Morrison, 2005, Astrophys. J. Lett. **631**, L41.

Milosavljević, M., V. Bromm, S. M. Couch, and S. P. Oh, 2009, Astrophys. J. **698**, 766.

Mirabel, I. F., M. Dijkstra, P. Laurent, A. Loeb, and J. R. Pritchard, 2011, Astron. Astrophys. **528**, A149.

Miralda-Escudé, J., M. Haehnelt, and M. J. Rees, 2000, Astrophys. J. **530**, 1.

Miranda, V., A. Lidz, C. H. Heinrich, and W. Hu, 2017, Mon. Not. R. Astron. Soc. **467**, 4050.

Mitchell-Wynne, K., A. Cooray, Y. Xue, B. Luo, W. Brandt, and A. Koekemoer, 2016, Astrophys. J. **832**, 104.

Mitchell-Wynne, K., *et al.*, 2015, Nat. Commun. **6**, 7945.

Mitra, S., T. R. Choudhury, and A. Ferrara, 2015, Mon. Not. R. Astron. Soc. Lett. **454**, L76.

Mitra, S., T. R. Choudhury, and A. Ferrara, 2018, Mon. Not. R. Astron. Soc. **473**, 1416.

Miyaji, T., *et al.*, 2015, Astrophys. J. **804**, 104.

Mortlock, D. J., *et al.*, 2011, Nature (London) **474**, 616.

Mukhanov, V., 2005, *Physical Foundations of Cosmology* (Cambridge University Press, Cambridge, UK), p. 442.

Muñoz, J. B., E. D. Kovetz, L. Dai, and M. Kamionkowski, 2016, Phys. Rev. Lett. **117**, 091301.

Munshi, D., I. T. Iliev, K. L. Dixon, and P. Coles, 2016, Mon. Not. R. Astron. Soc. **463**, 2425.

Murakami, H., *et al.*, 2007, Publ. Astron. Soc. Jpn. **59**, S369.

Navarro, J. F., C. S. Frenk, and S. D. M. White, 1997, Astrophys. J. **490**, 493.

Nikishov, A. I., 1962, Sov. Phys. JETP **633**, 549.

Nikolaev, S., M. D. Weinberg, M. F. Skrutskie, R. M. Cutri, S. L. Wheelock, J. E. Gizis, and E. M. Howard, 2000, Astron. J. **120**, 3340.

Nozawa, T., T. Kozasa, A. Habe, E. Dwek, H. Umeda, N. Tominaga, K. Maeda, and K. Nomoto, 2007, Astrophys. J. **666**, 955.

Odenwald, S., A. Kashlinsky, J. C. Mather, M. F. Skrutskie, and R. M. Cutri, 2003, Astrophys. J. **583**, 535.

Oh, S. P., 2001, Astrophys. J. **553**, 499.

Oke, J. B., and J. E. Gunn, 1983, Astrophys. J. **266**, 713.

Onaka, T., *et al.*, 2007, Publ. Astron. Soc. Jpn. **59**, S401.

Ota, K., *et al.*, 2017, Astrophys. J. **844**, 85.

Pacucci, F., A. Ferrara, A. Grazian, F. Fiore, E. Giallongo, and S. Puccetti, 2016, Mon. Not. R. Astron. Soc. **459**, 1432.

Page, L., *et al.*, 2007, Astrophys. J. Suppl. Ser. **170**, 335.

Palla, F., E. E. Salpeter, and S. W. Stahler, 1983, Astrophys. J. **271**, 632.

Pallottini, A., A. Ferrara, S. Gallerani, S. Salvadori, and V. D'Odorico, 2014, Mon. Not. R. Astron. Soc. **440**, 2498.

Park, K., and M. Ricotti, 2013, Astrophys. J. **767**, 163.

Partridge, R. B., and P. J. E. Peebles, 1967, Astrophys. J. **148**, 377.

Penzias, A. A., and R. W. Wilson, 1965, Astrophys. J. **142**, 419.

Percival, W. J., *et al.*, 2010, Mon. Not. R. Astron. Soc. **401**, 2148.

Petri, A., A. Ferrara, and R. Salvaterra, 2012, Mon. Not. R. Astron. Soc. **422**, 1690.

Planck Collaboration, Adam, R., *et al.*, 2016a, Astron. Astrophys. **594**, A1.

Planck Collaboration, Adam, R., *et al.*, 2016b, Astron. Astrophys. **596**, A108.

Portegies-Zwart, S. F., and S. L. W. McMillan, 2002, Astrophys. J. **576**, 899.

Press, W. H., and P. Schechter, 1974, Astrophys. J. **187**, 425.

Puchwein, E., C. Pfrommer, V. Springel, A. E. Broderick, and P. Chang, 2012, Mon. Not. R. Astron. Soc. **423**, 149.

Puget, J.-L., A. Abergel, J.-P. Bernard, F. Boulanger, W. B. Burton, F.-X. Desert, and D. Hartmann, 1996, Astron. Astrophys. **308**, L5 [http://adsabs.harvard.edu/abs/1996A%26A...308L...5P].

Pyo, J., T. Matsumoto, W.-S. Jeong, and S. Matsuura, 2012, Astrophys. J. **760**, 102.

Rauch, M., W. L. W. Sargent, and T. A. Barlow, 2001, Astrophys. J. **554**, 823.

Rees, M. J., 1968, Astrophys. J. **153**, L1.

Rees, M. J., 1976, Mon. Not. R. Astron. Soc. **176**, 483.

Rees, M. J., 1978, Nature (London) **275**, 35.

Regan, J. A., and M. G. Haehnelt, 2009, Mon. Not. R. Astron. Soc. **396**, 343.

Regan, J. A., P. H. Johansson, and J. H. Wise, 2014, Astrophys. J. **795**, 137.

Reichardt, C. L., 2016, in Understanding the Epoch of Cosmic Reionization: Challenges and Progress, *Astrophysics and Space Science Library*, Vol. 423, edited by A. Mesinger (Springer, Heidelberg), p. 227.

Ricotti, M., 2007, Astrophys. J. **662**, 53.

Ricotti, M., N. Y. Gnedin, and J. M. Shull, 2000, Astrophys. J. **534**, 41.

Ricotti, M., J. P. Ostriker, and K. J. Mack, 2008, Astrophys. J. **680**, 829.

Robertson, B. E., R. S. Ellis, S. R. Furlanetto, and J. S. Dunlop, 2015, Astrophys. J. Lett. **802**, L19.

Rudie, G. C., C. C. Steidel, and M. Pettini, 2012, Astrophys. J. Lett. **757**, L30.

Salvador-Solé, E., A. Manrique, R. Guzman, J. M. Rodríguez Espinosa, J. Gallego, A. Herrero, J. M. Mas-Hesse, and A. Marín Franch, 2017, Astrophys. J. **834**, 49.

Salvaterra, R., and A. Ferrara, 2003, Mon. Not. R. Astron. Soc. **339**, 973.

Sano, K., K. Kawara, S. Matsuura, H. Kataza, T. Arai, and Y. Matsuoka, 2015, Astrophys. J. **811**, 77.

Sano, K., K. Kawara, S. Matsuura, H. Kataza, T. Arai, and Y. Matsuoka, 2016, Astrophys. J. **818**, 72.

Santos, M. R., V. Bromm, and M. Kamionkowski, 2002, Mon. Not. R. Astron. Soc. **336**, 1082.

Sazonov, S., and R. Sunyaev, 2015, Mon. Not. R. Astron. Soc. **454**, 3464.

Schaerer, D., 2002, Astron. Astrophys. **382**, 28.

Schaye, J., T. Theuns, M. Rauch, G. Efstathiou, and W. L. W. Sargent, 2000, Mon. Not. R. Astron. Soc. **318**, 817.

Schechter, P., 1976, Astrophys. J. **203**, 297.

Schneider, R., A. Ferrara, P. Natarajan, and K. Omukai, 2002, Astrophys. J. **571**, 30.

Schneider, R., K. Omukai, A. K. Inoue, and A. Ferrara, 2006, Mon. Not. R. Astron. Soc. **369**, 1437.

Schutz, K., and A. Liu, 2017, Phys. Rev. D **95**, 023002.

Seo, H. J., H. M. Lee, T. Matsumoto, W.-S. Jeong, M. G. Lee, and J. Pyo, 2015, Astrophys. J. **807**, 140.

Shang, C., G. L. Bryan, and Z. Haiman, 2010, Mon. Not. R. Astron. Soc. **402**, 1249.

Shankar, F., M. Bernardi, R. K. Sheth, L. Ferrarese, A. W. Graham, G. Savorgnan, V. Allevato, A. Marconi, R. Läsker, and A. Lapi, 2016, Mon. Not. R. Astron. Soc. **460**, 3119.

Shectman, S. A., 1973, Astrophys. J. **179**, 681.

Shectman, S. A., 1974, Astrophys. J. **188**, 233.

Sherwin, B. D., *et al.*, 2017, Phys. Rev. D **95**, 123529.

Sheth, R. K., and G. Tormen, 2002, Mon. Not. R. Astron. Soc. **329**, 61.

Shull, J. M., and M. E. van Steenberg, 1985, Astrophys. J. **298**, 268.

Smoot, G. F., *et al.*, 1992, Astrophys. J. **396**, L1.

Sugimura, K., K. Omukai, and A. K. Inoue, 2014, Mon. Not. R. Astron. Soc. **445**, 544.

Sullivan, I., *et al.*, 2007, Astrophys. J. **657**, 37.

Sunyaev, R. A., and Y. B. Zeldovich, 1972, Comments Astrophys. Space Phys. **4**, 173 [http://adsabs.harvard.edu/abs/1972CoASP...4..173S].

Sunyaev, R. A., and Y. B. Zeldovich, 1980, Mon. Not. R. Astron. Soc. **190**, 413.

Takekawa, S., T. Oka, Y. Iwata, S. Tokuyama, and M. Nomura, 2017, Astrophys. J. Lett. **843**, L11.

Tananbaum, H., *et al.*, 1979, Astrophys. J. Lett. **234**, L9.

Tetarenko, B. E., *et al.*, 2016, Astrophys. J. **825**, 10.

Thacker, C., Y. Gong, A. Cooray, F. De Bernardis, J. Smidt, and K. Mitchell-Wynne, 2015, Astrophys. J. **811**, 125.

Theuns, T., J. Schaye, S. Zaroubi, T.-S. Kim, P. Tzanavaris, and B. Carswell, 2002, Astrophys. J. Lett. **567**, L103.

Thompson, R. I., D. Eisenstein, X. Fan, M. Rieke, and R. C. Kennicutt, 2007a, Astrophys. J. **657**, 669.

Thompson, R. I., D. Eisenstein, X. Fan, M. Rieke, and R. C. Kennicutt, 2007b, Astrophys. J. **666**, 658.

Thompson, R. I., *et al.*, 2005, Astron. J. **130**, 1.

Thornton, R. J., *et al.*, 2016, Astrophys. J. Suppl. Ser. **227**, 21.

Todini, P., and A. Ferrara, 2001, Mon. Not. R. Astron. Soc. **325**, 726.

Toller, G. N., 1983, Astrophys. J. Lett. **266**, L79.

Tornatore, L., A. Ferrara, and R. Schneider, 2007, Mon. Not. R. Astron. Soc. **382**, 945.

Totani, T., N. Kawai, G. Kosugi, K. Aoki, T. Yamada, M. Iye, K. Ohta, and T. Hattori, 2006, Publ. Astron. Soc. Jpn. **58**, 485.

Totani, T., Y. Yoshii, F. Iwamuro, T. Maihara, and K. Motohara, 2001, Astrophys. J. Lett. **550**, L137.

Totani, T., Y. Yoshii, T. Maihara, F. Iwamuro, and K. Motohara, 2001, Astrophys. J. **559**, 592.

Treister, E., and C. M. Urry, 2006, Astrophys. J. Lett. **652**, L79.

Treister, E., C. M. Urry, and S. Virani, 2009, Astrophys. J. **696**, 110.

Tsumura, K., T. Matsumoto, S. Matsuura, I. Sakon, and T. Wada, 2013, Publ. Astron. Soc. Jpn. **65**, 121.

Tsumura, K., *et al.*, 2010, Astrophys. J. **719**, 394.

Ueda, Y., M. Akiyama, G. Hasinger, T. Miyaji, and M. G. Watson, 2014, Astrophys. J. **786**, 104.

Ueda, Y., M. Akiyama, K. Ohta, and T. Miyaji, 2003, Astrophys. J. **598**, 886.

Valdés, M., and A. Ferrara, 2008, Mon. Not. R. Astron. Soc. Lett. **387**, L8.

Van Borm, C., S. Bovino, M. A. Latif, D. R. G. Schleicher, M. Spaans, and T. Grassi, 2014, Astron. Astrophys. **572**, A22.

Visbal, E., Z. Haiman, and G. L. Bryan, 2014, Mon. Not. R. Astron. Soc. **445**, 1056.

Vishniac, E. T., 1987, Astrophys. J. **322**, 597.

Volonteri, M., G. Lodato, and P. Natarajan, 2008, Mon. Not. R. Astron. Soc. **383**, 1079.

Volonteri, M., J. Silk, and G. Dubus, 2015, Astrophys. J. **804**, 148.

Wada, T., *et al.*, 2007, Publ. Astron. Soc. Jpn. **59**, S515.

Wada, T., *et al.*, 2008, Publ. Astron. Soc. Jpn. **60**, S517.

Wang, B., E. Abdalla, F. Atrio-Barandela, and D. Pavón, 2016, Rep. Prog. Phys. **79**, 096901.

Wang, Y., 2014, Mon. Not. R. Astron. Soc. **443**, 2950.

Wang, Y., and P. Mukherjee, 2006, Astrophys. J. **650**, 1.

Ward, J. T., *et al.*, 2016, in Millimeter, Submillimeter, and Far-Infrared Detectors and Instrumentation for Astronomy VIII, *Proc. SPIE* Vol. 9914 (SPIE–International Society for Optical Engineering, Bellingham, WA), p. 991437.

Watson, D., L. Christensen, K. K. Knudsen, J. Richard, A. Gallazzi, and M. J. Michałowski, 2015, Nature (London) **519**, 327.

Werner, M. W., *et al.*, 2004, Astrophys. J. Suppl. Ser. **154**, 1.

Willott, C. J., 2011, Astrophys. J. Lett. **742**, L8.

Windhorst, R. A., *et al.*, 2011, Astrophys. J. Suppl. Ser. **193**, 27.

Woosley, S. E., and A. Heger, 2015, in Very Massive Stars in the Local Universe, *Astrophysics and Space Science Library*, Vol. 412, edited by J. S. Vink (Springer, Heidelberg), p. 199.

Wright, E. L., 1998, Astrophys. J. **496**, 1.

Xu, H., J. H. Wise, and M. L. Norman, 2013, Astrophys. J. **773**, 83.

Xu, X., J. Zhang, and B. Wang, 2017, arXiv:1702.06358.

Yamada, M., T. Oka, S. Takekawa, Y. Iwata, S. Tsujimoto, S. Tokuyama, M. Furusawa, K. Tanabe, and M. Nomura, 2017, Astrophys. J. Lett. **834**, L3.

Yoneyama, T., 1972, Publ. Astron. Soc. Jpn. **24**, 87 [http://adsabs.harvard.edu/abs/1972PASJ...24...87Y].

Yue, B., A. Ferrara, F. Pacucci, and K. Omukai, 2017, Astrophys. J. **838**, 111.

Yue, B., A. Ferrara, and R. Salvaterra, 2016, arXiv:1601.02514.

Yue, B., A. Ferrara, R. Salvaterra, and X. Chen, 2013, Mon. Not. R. Astron. Soc. **431**, 383.

Yue, B., A. Ferrara, R. Salvaterra, Y. Xu, and X. Chen, 2013, Mon. Not. R. Astron. Soc. **433**, 1556.

Yue, B., A. Ferrara, R. Salvaterra, Y. Xu, and X. Chen, 2014, Mon. Not. R. Astron. Soc. **440**, 1263.

Zackrisson, E., C.-E. Rydberg, D. Schaerer, G. Östlin, and M. Tuli, 2011, Astrophys. J. **740**, 13.

Zahn, O., *et al.*, 2012, Astrophys. J. **756**, 65.

Zaroubi, S., 2013, in The First Galaxies, *Astrophysics and Space Science Library*, Vol. 396, edited by T. Wiklind, B. Mobasher, and V. Bromm (Springer, Heidelberg), p. 45.

Zemcov, M., P. Immel, C. Nguyen, A. Cooray, C. M. Lisse, and A. R. Poppe, 2017, Nat. Commun. **8**, 15003.

Zemcov, M., *et al.*, 2014, Science **346**, 732.